The Thesis Committee for Sean Laurids Porse
Certifies that this is the approved version of the following thesis:

Using Analytical and Numerical Modeling to Assess Deep Groundwater Monitoring Parameters at Carbon Capture, Utilization, and Storage Sites

APPROVED BY
SUPERVISING COMMITTEE:

Supervisor:

Michael H Young

Susan D. Hovorka

Jack M. Sharp

Using Analytical and Numerical Modeling to Assess Deep Groundwater Monitoring Parameters at Carbon Capture, Utilization, and Storage Sites

by

Sean Laurids Porse, B.S.

Thesis

Presented to the Faculty of the Graduate School of

The University of Texas at Austin

in Partial Fulfillment

of the Requirements

for the Degree of

Master of Science in Geological Sciences

The University of Texas at Austin

December 2013

Dedication

I dedicate this thesis to my parents. They have encouraged me to pursue my passions by providing me with the gift of higher education, and pushed me to grow as both a person and scientist. Without their tireless support, I wouldn't be half the man I am today.

Acknowledgements

This thesis would not have been possible without the financial support from the Hastings Monitoring, Verification, and Accounting Project, and the Gulf Coast Carbon Center. I would also like to thank Denbury Onshore LLC for their generous field and data access.

Thanks to my graduate committee members Michael Young, Susan Hovorka, and Jack Sharp for their personal and professional support during my thesis project. In particular, thanks to Michael for working with me as my main graduate adviser. His insight, attention to detail, and critical analysis skills greatly improved the quality of the project scope, data analyses methods, and scientific writing. I would also like to thank Sue for challenging me to improve in all facets of my technical background.

I would like to acknowledge the many researchers in the Bureau of Economic Geology who helped me develop my project: Mehdi Zeidouni for his time and support while learning his analytical model, Todd Caldwell for his generous assistance with MATLAB, Becky Smyth and Logan West for field work assistance, Brad Wolaver for his personal and professional support, Jiemin Liu for his help with XRD analyses, Patrick Mickler for assistance with water sample analyses, Changbing Yang for his expertise with PHAST, and Vanessa Nuñez-Lopez for her project management and guidance.

Thanks to the friends I've made here at UT; you have all made my time in Austin truly great. Finally, thanks to my brother Erik who gave me prophetic advice to wait to attend graduate school until I knew what I truly wanted to do. This advice has made all the difference.

Abstract

Using Analytical and Numerical Modeling to Assess Deep Groundwater Monitoring Parameters at Carbon Capture, Utilization, and Storage Sites

Sean Laurids Porse, M.S.Geo.Sci.

The University of Texas at Austin, 2013

Supervisor: Michael H. Young

Carbon Dioxide (CO_2) Enhanced Oil Recovery (EOR) is becoming an important bridge to commercialize geologic sequestration (GS) in order to help reduce anthropogenic CO_2 emissions. Current U.S. environmental regulations require operators to monitor operational and groundwater aquifer changes within permitted bounds, depending on the injection activity type. We view one goal of monitoring as maximizing the chances of detecting adverse fluid migration signals into overlying aquifers. To maximize these chances, it is important to: (1) understand the limitations of monitoring pressure versus geochemistry in deep aquifers (i.e., >450 m) using analytical and numerical models, (2) conduct sensitivity analyses of specific model parameters to support monitoring design conclusions, and (3) compare the breakthrough time (in years) for pressure and geochemistry signals. Pressure response was assessed using an analytical model, derived from Darcy's law, which solves for diffusivity in radial coordinates and the fluid migration rate. Aqueous geochemistry response was assessed using the

numerical, single-phase, reactive solute transport program PHAST that solves the advection-reaction-dispersion equation for 2-D transport. The conceptual modeling domain for both approaches included a fault that allows vertical fluid migration and one monitoring well, completed through a series of alternating confining units and distinct (brine) aquifers overlying a depleted oil reservoir, as observed in the Texas Gulf Coast, USA. Physical and operational data, including lithology, formation hydraulic parameters, and water chemistry obtained from field samples were used as input data. Uncertainty evaluation was conducted with a Monte Carlo approach by sampling the fault width (normal distribution) via Latin Hypercube and the hydraulic conductivity of each formation from a beta distribution of field data. Each model ran for 100 realizations over a 100 year modeling period. Monitoring well location was varied spatially and vertically with respect to the fault to assess arrival times of pressure signals and changes in geochemical parameters.

Results indicate that the pressure-based, subsurface monitoring system provided higher probabilities of fluid migration detection in all candidate monitoring formations, especially those closest (i.e., 1300 m depth) to the possible fluid migration source. For aqueous geochemistry monitoring, formations with higher permeabilities (i.e., greater than 4×10^{-13} m^2) provided better spatial distributions of chemical changes, but these changes never preceded pressure signal breakthrough, and in some cases were delayed by decades when compared to pressure. Differences in signal breakthrough indicate that pressure monitoring is a better choice for early migration signal detection. However, both pressure and geochemical parameters should be considered as part of an integrated monitoring program on a site-specific basis, depending on regulatory requirements for longer term (i.e., >50 years) monitoring. By assessing the probability of fluid migration detection using these monitoring techniques at this field site, it may be possible to

extrapolate the results (or observations) to other CCUS fields with different geological environments.

Table of Contents

List of Tables

List of Figures

List of Acronyms

AoR: Area of Review

AZMI: Above-zone monitoring interval

BEG: Bureau of Economic Geology

CCS: Carbon capture and storage

CCUS: Carbon capture, utilization, and storage

EOR: Enhanced oil recovery

GS: Geologic sequestration (of CO_2)

LHS: Latin hypercube sampling

LPSA: Laser particle size analyzer

MVA: Monitoring, verification, and accounting

SACROC: Scurry Area Canyon Reef Operators

UIC: Underground Injection Control Program

USDW: Underground Source of Drink Water

USEPA: United States Environmental Protection Agency

VOA: Volatile organic analysis

WHU: Well

Chapter 1: Introduction

The goal of any monitoring network is to minimize risk while maximizing monitoring network efficiency setup and the probability of parameter detection (Freeze et al., 1992). Based on this goal, the motivations for this thesis work are two-fold: (1) subsurface monitoring at fluid injection/disposal projects such as enhanced oil recovery (EOR) or carbon dioxide (CO_2) storage projects (i.e., geologic sequestration (GS)) is important to track physical and chemical parameters of injection fluids that can better define project boundaries, and demonstrate protection of underground sources of drinking water (USDWs), and (2) properly characterizing a project's physical and chemical characteristics, including subsurface structure, stratigraphy, as well as hydrogeology prior to initiating any monitoring program is crucial for a monitoring program's success. This thesis introduces: the motivations behind using CO_2 for resource production and storage activities, the regulatory bodies responsible for permitting these operations, the potential effects on groundwater aquifers (i.e., aquifers with any salinity) from failure by regulators and/or operators to remove operational risks, and how monitoring in the deep subsurface can maximize chances for early detection to avoid adverse leakage.

According to the International Panel on Climate Change (IPCC), recent atmospheric warming has been directly linked to continued anthropogenic activities, specifically CO_2 emissions (IPCC, 2005). Additionally, the effects from climate change are expected to continue through the 21st century with the growing industrialization of both established and developing nations. To counteract this trend, a number of options are either currently available or are being developed including: 1) reducing energy consumption using energy efficient technologies, 2) switching to less carbon-intensive fuels or renewable energy sources, and 3) carbon capture, utilization, and storage

(CCUS). The last option is a suite of technologies that: 1) separates and captures CO_2 emissions at a stationary emissions source (e.g., a coal-fired power plant), 2) transports the CO_2 via a pipeline or other mechanism (e.g., ship) to an injection site, and 3) injects CO_2 safely into a geologic formation (reservoir, injection interval) overlain with a low-permeability confining geologic formation (e.g., shale). Extensive site characterization is conducted prior to operation to ensure that the storage site has geologic and hydraulic properties conducive for the permanent storage and retainment of CO_2 as a supercritical fluid. If the main goal from a CCUS project is to inject CO_2 into the subsurface for permanent storage from the atmosphere, the injection process is known as geologic sequestration or GS (IPCC, 2005; USEPA, 2010; NETL, 2012b). CO_2 can also be injected to aid in the commercial recovery of hydrocarbons in mature oil and gas fields, through a process known as CO_2 EOR. Storage goals can be linked with EOR, through the incidental storage of either naturally or anthropogenically sourced CO_2 (NETL, 2010).

Through operations such as CO_2 EOR, the oil and gas industry has developed specialized experience in implementing commercial reservoir management tools (e.g., pressure measurement) that help regulate production and monitor for adverse fluid migration that may occur. The GS research community has focused on a wide variety of monitoring related topics including the use of pressure and geochemistry as fluid migration indicators. However, the integration between these two communities continues to evolve. This thesis explores the potential to integrate different methods of subsurface monitoring (e.g., pressure and geochemistry) from commercial and research applications by comparing their use in a conceptualized geologic model informed by site-specific data. With the apparent increased appeal from CO_2 EOR as a way to commercialize GS, creating sound monitoring network development tools are critical to the long term success of this technique as a climate change mitigation technology.

GEOLOGIC SEQUESTRATION

Research on multiple technical topics surrounding geologic sequestration (GS) as well as the successful operation of demonstration and commercial GS projects aid in the continued commercial development of GS. Internationally, the longest running commercial GS operation is the Sleipner CO_2 injection project off the west coast of Norway in the North Sea, operated by Statoil. The Sleipner project has stored around 1 million metric tons (Mt) of CO_2 annually into the Utsira Sandstone Formation since 1996 in response to a government-levied tax on carbon emissions (Kongsjorden, 1997). In addition to Sleipner, projects also exist in Australia, Germany, Algeria, Great Britain, as well as China (MIT, 2013). In the United States, the Department of Energy (DOE) has invested over 3 billion USD towards the development of GS pilot projects via seven regional carbon sequestration research partnerships nationwide (DOE, 2013). In total, DOE estimates (NETL, 2012b) a storage capacity of almost 2.2 billion metric tons of CO_2 in the United States and Canada. The eastern portion of Texas (inclusive of Texas Railroad Commission Regions 1-6) has roughly 4,000 Mt of CO_2 storage capacity in existing oil and gas fields (NETL, 2012). This oil and gas field capacity has the potential to safely store hundreds of years' worth of cumulative US greenhouse gas (GHG) emissions within suitable geologic formations in both onshore and offshore reservoirs of the Gulf Coast of Texas.

An important aspect of progress toward commercialization of GS already in place is a comprehensive regulatory structure administered through the U.S. Environmental Protection Agency (USEPA) and state regulatory organizations. USEPA's Underground Injection Control (UIC) Program regulates the construction, operation, permitting, and closure of injection wells that place fluids underground for storage or disposal, including CO_2 storage and commercial EOR operations. USEPA derives its authority to regulate

underground injection from the Safe Drinking Water Act for the protection of underground sources of drinking water (USDWs), defined as aquifers with total dissolved solids (TDS) less than 10,000 mg/l (40 CFR 144.3). As of 2011, dedicated GS operations are permitted under the UIC Program's Class VI well category, which lays out specific steps to manage, safely operate, and monitor GS injection activities (40 CFR 146.81-146.95). One key to the UIC permitting process is the development of a monitoring plan for injection operations to ensure that no USDWs are endangered via conductive migration pathways (e.g., abandoned wellbores, faults, fractures) (USEPA, 2010). At the state level, Subpart B of Texas Administrative Code Title 16 Chapter 5 outlines requirements GS operators must follow to operate a GS project in Texas that are broadly similar to USEPA's Class VI requirements.

In a separate set of regulations under the authority of the Clean Air Act, USEPA has also outlined requirements for the mandatory reporting of greenhouse gas (GHG) emissions from specific industrial sources (40 CFR 98).For GS, project operators must report GHG emissions under Subpart RR of the Mandatory GHG Reporting Program by submitting records of CO_2 received, injected, produced, and emitted by surface leakage over varying reporting time frames (40 CFR 98.442). Under Subpart RR, GS operators must develop a CO_2 Monitoring, Reporting, and Verification (MRV) program to monitor and quantify any surface leakage within the approved monitoring area (40 CFR 98.448). Required monitoring activities under the MRV plan can in large part also satisfy the UIC Class VI permit requirements.

Developing proper GS site characterization, operation, and monitoring practices can not only satisfy these environmental regulations under USEPA and Texas State regulatory programs, but help reinforce safe practices as GS continues toward widespread commercialization.

CO_2 Enhanced Oil Recovery

While numerous GS research efforts continue, GS' use as a widespread climate change mitigation technology remains elusive primarily due to the commercial cost of separating and capturing CO_2 from an emissions source (e.g., coal-fired power plant) (NETL, 2013). In lieu of financial or regulatory drivers, one commercial process that may help offset the large upfront costs associated with developing and operating capture facilities is using CO_2 EOR with incidental CO_2 storage. Operators have used CO_2 EOR in the United States for over forty years (Crameik and Plassey, 1972). Until recently however, operators were not interested in the CO_2 storage capabilities of this technology. With continuing discussion of future incentives available for such activities, operators may look to officially account for this incidental storage amount along with normal hydrocarbon production. This thesis, however, will not discuss the implications of such incentives.

During the CO_2 EOR process, a commercial operator uses CO_2 to enhance the recovery of hydrocarbons while incidentally storing CO_2 permanently in isolation from the atmosphere through deep subsurface storage or closed loop recycling. The goal for all EOR operations is to increase the sweep efficiency within an oil and gas reservoir by injecting exogenous materials that can decrease oil viscosity, increase the oil volume, or increase fluid and hydrocarbon miscibility. Multiple methods using different classes of fluids exist to enhance the recovery of hydrocarbons including: thermal (e.g., steam injection), chemical (e.g., polymer drive), and gas (e.g., N_2 or CO_2) (Alvarado, 2010). In Texas, CO_2 has been used as a type of EOR solvent in commercial fields such as the Scurry Area Canyon Reef Operators (SACROC) oil field since the 1970s (Crameik and Plassey, 1972).

CO_2 EOR operations can share similar project design specifications with GS projects. However, while CO_2 EOR and GS fall under the larger technology umbrella of CCUS, operations differ in their primary focus of CO_2 use at the respective field, as well as their applicable regulatory programs. CO_2 EOR operations commercially enhance the production of hydrocarbons while GS projects' exclusive goal is to permanently sequester CO_2 in the subsurface. CO_2 EOR operations can also significantly differ from GS projects because of: legacy surface and subsurface features from previous activities (e.g., abandoned wells, brine pits, storage tanks), potential for increased subsurface heterogeneity (e.g., faults and fractures) compared to GS sites, and the collection of hydrocarbons from producing wells that would not be present at GS operations looking to store CO_2 into saline formations (Wolaver et al., 2013). These differences can add a layer of complexity when designing a deep subsurface research monitoring program at CO_2 EOR sites, because the existing infrastructure increases the possibility that improperly completed or damaged wellbores present can act as conduits for potential fluid migration during operations (Nordbotten et al., 2004; Birkholzer et al., 2009; Humez et al., 2012; Ebigbo, 2012; Wolaver et al., 2013).

Individual U.S. States can apply for UIC primacy to manage the UIC program as long as they meet minimum national standards for program provisions and injection well requirements (40 CFR 145). In Texas, the Railroad Commission has primacy to issue UIC permits for Class II wells (i.e., wells that inject fluids associated with oil and gas production) under Texas Administrative Code Title 16, Part 1, Chapter 3. In contrast to Class VI (GS) operators, Class II well owners or operators are not required to monitor geochemistry changes in specific geologic formations above their injection and/or disposal operations. Instead, regulation is focused on monitoring physical parameters such as injection pressure, flow rate, and cumulative volume ranging from daily to

monthly during operation. Operators have incentive to conduct these types of monitoring practices; pressure management in the production reservoir is an established practice during operations that can help optimize hydrocarbon production as well as CO_2 storage (Phade and Gupta, 2008; Hermanrud et al., 2013).

Subpart UU of USEPA's Mandatory GHG Reporting Program requires operators of projects injecting CO_2 into the subsurface through a single well or group of wells to report the mass of CO_2 received prior to injection (40 CFR 98.470-472). Unlike Subpart RR, operators that fall under Subpart UU are not required to develop a monitoring plan to account for potential surface leakage emissions. Under Texas Administrative Code Chapter 5 Subpart C, EOR operators can voluntarily submit a plan to certify the amount of CO_2 incidentally stored during production activities with the Railroad Commission. Importantly, such activities under Subpart C are not for obtaining a permit, only for an operator voluntarily seeking an official certification of CO_2 stored.

SUBSURFACE PHYSICAL INTERACTIONS

During GS operations, as long as constant injection rates continue and no fluids are produced, injection zone pressures will tend to increase within the area of review (AoR) and/or the AoR size may increase. The AoR is the region surrounding a GS project where this increase in pressure could lift reservoir fluids up an open pathway, potentially endangering USDWs by injection activity (USEPA, 2010). Formation pressures increase due to the relative incompressibility of native fluids and the introduction of new fluids into the system. Variations in pressure response can be caused by variability of hydraulic properties of the geologic formations as well as the phase of the injected fluid. With CO_2 EOR, the increase of pressure is needed to optimize hydrocarbon production; thus

injection and production occur simultaneously that can effectively manage subsurface pressures.

Pressure has been used as a versatile indicator for determining the presence of stored gases (e.g., CO_2, natural gas) in the subsurface for commercial and research purposes (Perry, 2005; Meckel and Hovorka, 2010; Hovorka et al., 2011; Sun and Nicot, 2012). For the natural gas storage industry, pressure monitoring is used for determining inventory verification, caprock seal integrity, as well as an indirect measurement of potential leakage (Perry, 2005). At the Southeast Carbon Sequestration Partnership's (SECARB) pilot project in Cranfield, MS, researchers from the Texas Bureau of Economic Geology (BEG) implemented continuous pressure monitoring both in-zone (i.e., injection zone) as well as in an above-zone monitoring interval (AZMI) roughly 112 meters above the injection zone for twenty four months while field production activities occurred (Meckel and Hovorka, 2010; Hovorka et al., 2011). During these activities, pressure signals within the injection reservoir increased by over 80 bar (8,000 kPa) while AZMI pressure signals displayed a more subdued and delayed response, increasing by less than 7 bar (700 kPa) over the monitoring time frame. As the authors discuss, a first order conclusion from this large pressure disparity is a lack of vertical connectivity between the injection zone and the AZMI formation at the oil field. It was hypothesized that the slight increase in AZMI pressure was attributed to a slow behind-casing fluid flow that was generally localized, but significant engineering-based noise (e.g., well remediation, dual depth interval completion) complicated this conclusion (Meckel and Hovorka, 2010; Hovorka et al., 2011).

Sun and Nicot (2012) have modeled a novel process to locate anomalous AZMI pressure signal origins based on the application of source identification from the contaminant and remediation sciences. By inverting a modeled set of AZMI pressure

data, the authors were able to back out the fluid migration history and most likely locations of the source for fluid migration under a variety of scenarios including for known, as well as unknown, migration sources into the AZMI. Sun and Nicot concluded that the linear inversion solvers can be applied to real-world leakage cases using pressure data.

As shown in practice, the physics of pressure propagation as a rapid response to fluid injection can be advantageous for not only operational stability and subsurface retention, but USDW protection. To take advantage of this efficiency, operators can install down-hole pressure gauges (i.e., an assembly that delivers an electrical signal that represents the measured pressure) that can measure injection and reservoir pressure perturbations within the injection formation(s) and overburden through optical, acoustical, and pneumatic methods (Omega, 1998, Schlumberger, 2006a). While there are a variety of types of sensors based on measuring types, sensitivities, and price ranges, some of the most reliable down-hole gauges incorporate quartz crystals as the main measure for strain. Quartz, when placed under a stress, will strain with a precise, repeatable, and measureable response vibration based on encountered temperatures and pressures (Schlumberger, 2006b). The well understood elastic properties of quartz make it ideal for use in oil and gas reservoirs, including high temperature and pressure environments (i.e., greater than 15,000 psi and 350°F) (Avant, 2012).

Overall, early fluid migration detection via pressure signals in the deep subsurface can: 1) remediate or adapt operations prior to USDW endangerment and/or atmospheric interaction, and 2) provide proof and increase confidence (as seen at the Cranfield site) that the storage system is intact, potentially reducing the need for long term monitoring.

SUBSURFACE GEOCHEMICAL INTERACTIONS

GS is designed to be effective. CO_2 injection follows a period of thorough characterization and permitting to demonstrate that injection fluids will be retained in the injection zone. In order to understand all aspects of the CO_2 injection process, researchers have conducted studies to assess the potential geochemical impacts of large scale CO_2 injection on groundwater by examining the mechanisms for CO_2 and deep brine migration in the injection zone as well as in shallower aquifers. Over thousands of years, CO_2 reactions can transition from structural trapping, to fluid dissolution trapping, and finally to mineral dissolution (Gaus, 2008). Over project timescales, structural and fluid dissolution trapping are anticipated to be the main methods of CO_2 isolation. CO_2 is less dense than the surrounding formation fluids in an injection zone that leads to a relative buoyancy effect that drives CO_2 towards the top of a geologic formation when injected (Bachu, 2003). Operators using any site for CO_2 injection will have previously identified prior to injection an impermeable geologic formation or formations (e.g., shale) to contain such buoyant fluids. However, it is possible that failure of confinement could occur and CO_2 or formation brines could leak into overlying aquifers through conduits such as existing wells, faults, and fractures (Nordbotten et al., 2004; Class et al., 2009). When CO_2: 1) is injected for either production (e.g., EOR) or storage purposes, or 2) migrates out of the intended storage formation, CO_2 can react with formation water/brine, disassociate and combine to form carbonic acid, a weak acid via the following reaction:

$$CO_2 + H_2O \leftrightarrow H_2CO_3 \leftrightarrow H^+ + HCO_3^- \qquad (1.1)$$

With the introduction of a weak acid, the pH of an aquifer can drop, depending upon the buffering capacity of the aquifer material. Furthermore, such pH reactions in addition to reactions occurring from direct contact of carbonic acid and rock material can corrode well materials such as cements or steel. The end results of these reactions, with

the presence of reactive water and rock materials, can increase specific element-concentrations such as prevalent cations and anions (e.g., Ca^{2+}, Cl^{-}) or trace elements (e.g., Pb^{3+}, As^{5-}) (IPCC, 2005; Wilkin and Digiulio, 2010).

Researchers have investigated the geochemical effects of CO_2 and formation brine migration on the injection zone (i.e., in-zone), USDWs (i.e., AZMI), and the near surface. For in-zone effects, Kharaka et al. (2006) researched the geochemical effects from injecting 1,600 Mt of CO_2 into the Frio Sandstone Formation at the Frio pilot project in Texas. In brief, they found sharp drops in pH, large increases in total alkalinity due to carbonate formation buffering, marked transient increases in Fe concentrations, and shifts in dissolved inorganic carbon (DIC) within the Frio formation (Kharaka et al., 2006). Emberley (2005) compared reservoir water samples taken prior to and during CO_2 injection at the Weyburn Oil Field, finding decreased amounts of dissolved element and chemistry characteristics (Cl^{-}, pH, H_2S), and increases in total alkalinity and Ca^{2+}. Other associated fluctuations of chemistry at Weyburn were similar to study results from other research projects (e.g., Kharaka et al., 2006), stressing the importance of having a strong understanding of the production interval mineralogy to fully understand the oil-water-rock reactions. Other studies (Lewicki et al., 2007) have examined CO_2 leakage analogue sites, such as geothermal, volcanic and other sedimentary basins that advance the understanding of CO_2 migration by examining the high permeability pathways that allow naturally occurring CO_2 and associate fluid migration to shallower depths.

For USDWs, Zheng et al. (2009) modeled the potential geochemical effects of CO_2 migration into shallow groundwater aquifers using the reactive transport modeling simulator TOUGHREACT. They found that after normalizing 38,000 groundwater samples to find average aqueous elemental concentrations, under certain modeled scenarios, CO_2 and water reactions mobilized hazardous elements (e.g., lead and arsenic)

at or near EPA Maximum Contaminant Levels (MCLs). Researchers have found that actual risks to shallow aquifers and the near surface from contamination are minimal (Smyth et al., 2008; Kell, 2011; Yang et al., 2013). In the near surface, Yang et al. (2013) found that after ten separate field sampling events (over three years) at the Cranfield CO_2 EOR field in Cranfield, MS, no shallow groundwater samples contained trace element concentrations above MCLs. Kell (2011) found that contamination by oil and gas related activities such as: drilling and completion, production, fluid disposal, and plugging and abandonment were minimal based on comprehensive studies in two historically prolific oil and gas production states, Ohio (from 1983-2007) and Texas (from 1993-2008). Finally, while CO_2 injection has occurred in Gulf Coast oil fields since the 1970s, no degradation below drinking water quality standards has been measured by researchers (Smyth et al., 2008; Yang et al., 2013).

The initial motivation for monitoring at depth during CO_2 injection is to prevent CO_2 migration into USDWs by early detection. While specific shifts in element concentrations due to CO_2 – rock – water interactions are important for understanding the sensitivity and significance of such monitoring approaches at GS sites, the modeling portion of the research project conducted herein will primarily focus on brine migration signal sensitivity alone. This brine migration can be caused by an increase in reservoir pressures due to the associated CO_2 injection, lifting brine into the near surface via a migration pathway (Class et al., 2009). Brine-rock interactions can mobilize trace elements contained within surrounding rocks and degrade freshwater aquifers if CO_2/brine leaked (Gaus, 2010). These brines can equilibrate with injected CO_2 over short (i.e., 10-100 years) and long (i.e., 1,000+ years) time frames, and when displaced by injection activities, can both carry CO_2 and be a precursor to pure phase CO_2 migration (IPCC, 2005).

With large disparities between total dissolved solids of brine and shallower aquifers, significant damage can be done to freshwater aquifer water quality, and such near surface effects have been studied in the environmental remediation and groundwater sciences (Vengosh, 1994; Siirila et al. 2012). However, the risks associated with deep brine migration to shallow aquifers are varied. Nicot (2009) demonstrated through a single-phase groundwater flow model of Gulf Coast aquifers that CO_2 injection can have localized intrusion effects on aquifers, but regional effects (i.e., within shallower connected aquifers) are largely attenuated. In contrast, Birkholzer et al. (2009) identified through modeled CO_2 injection in the Illinois Basin, a current candidate location for GS, that pressure gradient increases in storage formations are high enough to cause extensive bring migration on the order of hundreds of kilometers if open conduits exist. Thus, understanding the sensitivities of vertical brine flow is critical to efficiently answer questions on the best practices to implement a CCUS operations and groundwater monitoring program to operational integrity.

The groundwater remediation sciences have had limited success using geochemical monitoring to understand near surface fluid flow dynamics of groundwater contaminants (e.g., non-aqueous phase liquids, metals) transport and the means to remediate such contaminants (Davis, et al., 1999; Kao and Wang, 2001; Mulligan et al., 2001). Applied to the deep subsurface, fluctuations in aqueous geochemistry can lead to an early understanding of fluid migration both within the reservoir or to assess the existence of any leakage into overlying formations. The parameters to monitor largely depend on the goals of the project (e.g., length of time to monitor) and on site conditions. Choosing a primary parameter that does not occur ubiquitously in high concentrations, and is conservative in the planned monitoring formation is advantageous. From a CCUS perspective, formation brines occur ubiquitously in the Gulf Coast of Texas, with

salinities upwards of 300,000 mg/l total dissolved solids (TDS) due to the presence of large salt dome structures, like those structures present at Hastings (McWilliams, 1972; Kharaka, 2006). This stands in contrast to shallow groundwater chemistries that are orders of magnitude smaller in TDS concentrations, making the measure of prevalent brine ion concentrations a potentially useful tracer for migration detection into shallower formations.

In the case of GS, modeling studies have primarily focused on tracking constituents potentially mobilized from minerals as pH decreases, such as lead and arsenic from sulfides, when levels exceed regulatory concentration levels (Apps, 2009; Siirila et al., 2012). Furthermore, field results from Kharaka et al. (2006) show that pH, alkalinity, and Fe^{3+} can also fluctuate, potentially indicating the presence of CO_2 and groundwater interaction. In addition to monitoring naturally occurring elements, tracers can be injected into the reservoir and produced at the same or other locations to track fluid migration. Tracers should be selected such that the ambient concentration is low, and so that even trace amounts detected in the subsurface can be differentiated from natural background concentrations. In general tracers must be chemically inert, environmentally safe, nontoxic, persistent, and stable over the intended monitoring period (Stalker et al., 2009). Tracers such as noble gas isotopes of xenon, neon, argon, elemental compounds like sulfur hexafluoride, and even injectate (e.g., CO_2) can be monitored for small (i.e. ppm or smaller) changes in concentrations at monitoring wells located away from the injection site (Nimz and Hudson, 2005; Stalker et al., 2009). In practice, geochemical methods have successfully identified oil and gas fields during exploration by quantifying near-surface concentrations of ethane and heavy hydrocarbons migrating from deeper oil and gas basins (Horvitz, 1985).

COMPUTATIONAL MODELING

Computational models are a critical step in the development of a monitoring plan (Yang et al., 2013). Prior to making field-based measurements, simulating the designed response of the system and any risk factors such as unintended CO_2 migration are needed to understand field sensitivities. In general, three major types of models are used in GS research: analytical, semi-analytical and numerical, all having advantages and disadvantages (Schnaar, 2009). Analytical and semi-analytical models represent more simplistic geomechanical and geochemical processes, such as single-phase fluid flow in porous media and abandoned wellbores (Nordbotten et al., 2005; LeNeveu, 2008). The main advantages of using analytical models come from efficient processing and relatively lower computing power requirement while still using realistic modeling parameters to solve fundamental equations. Additionally, analytical and semi-analytical models can more effectively model fluid transport via wellbores than numerical models due to the spatial disparity between well diameters and modeled geologic domains (Schnaar, 2009; Zeidouni, 2012). However, analytical and semi-analytical models cannot simulate more complex modeling scenarios (e.g., three-dimensional flow, formation heterogeneity, or complicated boundary conditions); only numerical models can account for these conditions. Numerical fluid models solve a series of governing equations for the flow and transport of groundwater and other fluid phase liquids and gases by discretizing the flow domain and time, in one, two, or three dimensions. Such models are commonly used in petroleum engineering for reservoir characterization (e.g. ECLIPSE, CMG-GEM) and have been used by researchers to examine potential CO_2 and associated fluid migration effects (Nicot, 2009).

These and other computational models have been adapted for GS research to help understand CO_2 migration risks on groundwater resources, model multiphase flow in the

subsurface for comparison with GS pilot projects, and test the sensitivity of reservoir characteristics on modeled CCUS efforts (Law and Bachu, 1996; Doughty and Pruess, 2004; Birkholzer et al., 2009; Cihan et al., 2011). The computing power necessary to run numerical models, based on project goals, can be demanding or prohibitive. When used in conjunction with each other, analytical models can quickly screen potential GS sites for subsequent intensive modeling with numerical codes, and can also be used to check numerical modeling results (Schnaar, 2009).

GROUNDWATER MONITORING NETWORK DEVELOPMENT

In a set of benchmark papers by Freeze and others, an important discussion on the purpose of groundwater monitoring highlights the inherent adversarial nature between entities that create regulations and the commercial operators who must follow such requirements and still maintain profitability (Massmann and Freeze, 1987; Massmann et al., 1991; Freeze et al., 1992). These papers stressed that proper monitoring of any type of fluid should, as goals, minimize risk while maximizing monitoring network efficiency setup and the probability of fluid leakage detection. The monitoring network should also meet specific cost/benefit analyses; most networks can maximize the probability of leak detection, but eventually the owner or operator will reach a cost prohibitive threshold (Freeze et al., 1992). Both groundwater monitoring and CO_2 accounting are necessary for both CCS and CCUS projects as industry best practices, as well as through regulatory requirements. Ultimately, regulations like the Class II and VI monitoring programs (e.g., 40 CFR 146.23, 40 CFR 146.90) are an interplay between the risk-cost-benefits of a monitoring network and highlight the different objectives for regulators and companies. Regulatory agencies are in place to set requirements and procedures that will greatly reduce potential project failures (e.g., contamination of USDWs) that can endanger

human health and the environment. Owners or operators of fluid and/or waste disposal projects look to operate their facilities in a manner that optimizes profits while still meeting regulatory requirements.

However, a monitoring network alone does not guarantee leakage detection; it relies upon a probability of leakage detection through risk analyses conducted prior to monitoring network construction and operation, known as "risk-based engineering" (Freeze et al., 1992). This approach incorporates sets of data and analytical/numerical models only if they are useful in the final decision making process, and such data sets are collected to minimize the uncertainty of site geology (i.e., uncertainty between location and continuity of structure and stratigraphic bounds controlling the hydrogeology), and formation parameters (i.e., formation permeabilities). It is only through an understanding of the geology, hydrogeology, and expected operational parameters that a risk-based engineering program can be properly implemented. For this thesis, datasets will help to tailor generalized models to a more realistic conceptualized geologic domain, towards the goal of determining monitoring parameter sensitivity.

GOALS AND HYPOTHESES

This study is part of the second of a five stage research plan that the Texas Bureau of Economic Geology (BEG) is developing and implementing for a research monitoring, verification, and accounting (MVA) program, during commercial operations at the Hastings Field, fault blocks B and C (Figure 1.1, 2.1). The research MVA program is required as part of acquired U.S. Department of Energy (DOE) support for anthropogenic capture of one million tons of CO_2 annually from the Air Products hydrogen plant in Port

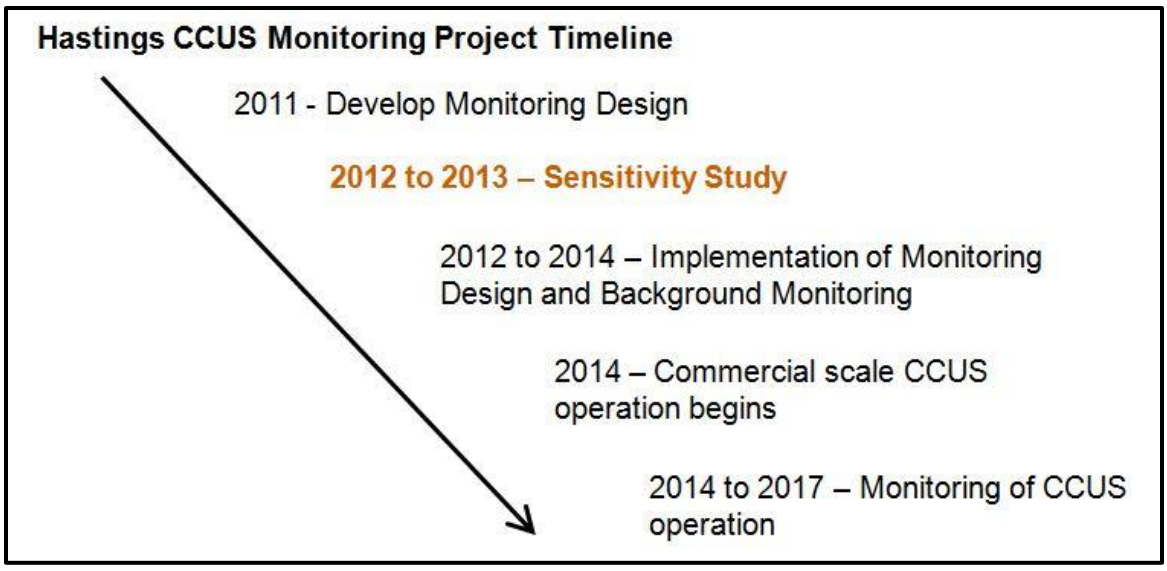

Figure 1.1: Hastings monitoring, verification, and accounting research project time frame. Orange text highlights the scope of this thesis work.

Arthur, TX in addition to CO_2 sourced from the Leucadia Lake Charles gasification facility (NETL, 2012a). The BEG currently collaborates with Denbury Onshore LLC (hereafter referred to as Denbury) on this research MVA plan for the goal of providing retention data of CO_2 in the production reservoir for permanent isolation from the atmosphere. Some of the monitoring began with the arrival of CO_2 in Fault Block A in 2012, but this research project's scope falls under injection monitoring in fault blocks B and C beginning in 2014 (Figure 2.1).

To help attain the larger goal of demonstrating retention through a research MVA program, the goals of this research are to: (1) understand the limitations of monitoring pressure versus aqueous geochemistry in the deep subsurface (i.e., 400 meters and deeper) using analytical and numerical models, (2) conduct sensitivity analyses of theoretic formation and migration pathway parameters to support monitoring design conclusions, and (3) compare the breakthrough time (in years) for pressure and geochemistry signals in an idealized geometry. Analyses are performed on the monitoring

network set up by modeling one monitoring well installed into multiple overlying monitoring formations. Simulated fluid migration will occur for 100 years, vertically up a conceptualized fault that intersects all geologic formations. The term fluid migration in this thesis refers to a modeled constant flux of fluid vertically up a geologic fault by Darcian flow. Groundwater refers to all qualities of water, from potable to saline. Fluid migration does not refer to migration via a discrete wellbore, which would include separate assumptions not valid for this research. This research is also not an implicit quantification of the likelihood for fluid migration at any studied field from specific mechanisms.

Study results should help determine the type of monitoring that could be implemented at commercial EOR operations, either pressure which is emphasized as the primary monitoring tool under conventional oilfield practices, or geochemistry, which the groundwater remediation sciences emphasize for contaminant tracking and remediation. Initial investigations from this study led to the hypothesis that pressure monitoring would show faster fluid migration detection, potentially providing efficient early signal detection to facilitate operations mitigation prior to any impacts on USDWs and/or the atmosphere. However, geochemistry as a secondary monitoring tool could be expected to be useful under limited monitoring network conditions, such as in higher permeable formations located close to the migration source, or over longer periods of monitoring (i.e., > 50 years). Ultimately, this research helps to highlight the importance of an integrated and well characterized approach to groundwater and CO_2 monitoring at CCUS fields. By highlighting the best monitoring network parameters to use, these results can help inform environmental regulatory discussions moving forward on how to prevent unintended CO_2 migration into above-zone formations and the atmosphere and optimize monitoring network setup efficiency.

Chapter 2: Site Description and Methods

PROJECT OVERVIEW, SITE DESCRIPTION, AND GEOLOGIC HISTORY

For this research project, the BEG collected and compiled data from the Hastings Oil Field, located in Brazoria County, Texas, USA (Figure 2.1). The field was first discovered in 1936, and the first commercial operations begin in 1941. Currently, Denbury owns and operates the West Hastings Field. Denbury began enhancing hydrocarbon production using CO_2 transported in their Green Pipeline initially from

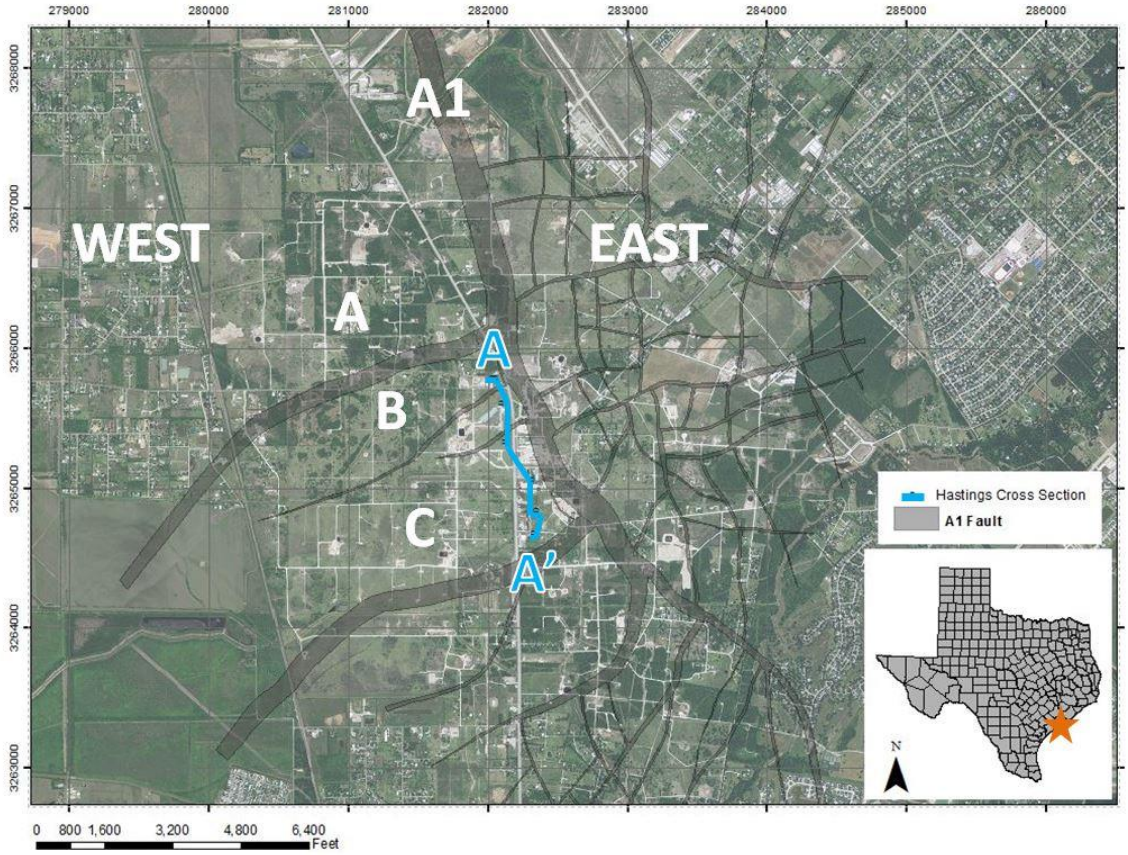

Figure 2.1: Hastings Field, Brazoria County, Texas, USA. Gray lines indicate faulting at Frio sandstone formation depth (1524 meters/5000 feet). Hastings is divided into West and East Fields along the major A1 Fault. West Hastings is divided on the surface into fault blocks A, B, and C. Cross section in Figure 3 from A to A' featured in blue.

natural CO_2 sources from the Jackson Dome in December 2011. In December 2012, about one million metric tons per year of CO_2 from the Air Products hydrogen production facilities located in Port Arthur, Texas were added to the system.

Averaged characteristics of the Hastings Field are shown in Table 2.1. The field sits on a domal uplift caused by a deep-seated piercement salt dome. As a result, the subsurface contains a collection of faults that radiate outwards from the salt dome intrusion that acted as conduits for reservoir charge and create structural traps for hydrocarbon accumulations (McWilliams, 1972; Banga et al., 2003). Hastings Field is divided by a northwest trending/northeast dipping normal fault that is part of a crestal graben of the salt dome, into the West and East Hastings at depth in the Frio Sandstone (Figure 2.1). The field is further divided in the subsurface into Fault Blocks A, B, and C in the West Hastings portion of the field by a series of faults that hydrologically isolate each block in terms of production and are used to stage the current commercial operations.

The Frio Sandstone is the major production interval at the Hastings Field that varies greatly in thickness, but can be as thick as 730 meters (2,400 feet) regionally (Thomas, 1953). The Frio Sandstone is one of the most productive intervals of any onshore reservoir in the Gulf Coast of Texas, producing over 4 billion barrels of oil since commercial production began. Historically at Hastings, hydrocarbons are produced from around 1544-1800 meters (5,100 to 6,000 feet) (McWilliams, 1972). The Frio was deposited in beach and near shorface facies' during a major seaward transgression during the Oligocene that allowed rapid burial of sediments, further overlain by sediments during a coastal regression (Halbouty, 1968; Ambrose et al., 2008).

Hastings Field Characteristics		Frio Sandstone Characteristics	
First Discovered	1936	**Formation Dip (degrees)**	6-9
Current Number of Production Wells	93 active	**Avg. Porosity (%)**	29
Major Production Interval	Upper and Lower Frio Sandstone	**Avg. Permeability m^2 (mD)**	5.84e-13 (592)
Cumulative Oil Production to Date (MMBO)	578	**Depth, m (ft.)**	1800 (5900)
Oil Gravity (API Units	31	**Temperature (°C)**	71.1
		Avg. Brine TDS (mg/l)	>100,000

Table 2.1: Hastings Field and Frio Sandstone averaged characteristics (Denbury, personal communication).

Overlying the Frio is approximately 180 meters (600 feet) of late Oligocene and early Miocene aged Anahuac shale, the regional confining unit in the Hastings field. The Anahuac Shale, a marine shale, represents a major transgressive sequence, where the paleo-Texas coast line rapidly moved inward towards the Balcones Uplift (Halbouty, 1968; Maynard, 2006). Above the Anahuac sits a series of Miocene through Pleistocene through Miocene aged clays, sands, and shales. While these Miocene-aged sandstones are named in the literature (Baker Jr., 1979), they are traditionally assigned numbers at

Hastings (e.g., M-14 sits above the Anahuac) and are delineated primarily by their hydraulic properties as they vary greatly in thickness and continuity. Many formations overlying the Anahuac were formed by rapid sedimentation, sourced from prolific delta deposits across South Texas in the Miocene during major seaward regressions of the Gulf Coast coastline (Halbouty, 1968; Rainwater, 1970). In parts of the Gulf Coast, this rapid sedimentation also buried significant amounts of organic materials, the precursors for prolific Miocene oil fields in Texas and Louisiana, where over 7 billion barrels of oil and 35 trillion cubic feet of gas have been produced since discovery (Rainwater, 1970).

Modeling the sensitivities of these Miocene-aged sandstones for monitoring is a primary focus of this thesis. To apply field properties to both analytical and numerical models used in this research project, data were collected and/or compiled from literature and field samples, and also processed in the laboratory. A West Hastings cross section generated by historical log data obtained from Denbury trending from northwest to southeast in Fault Block B is shown on Figure 2.2. Based on this cross section, deeper Miocene sandstones (e.g. 1220-1370 meters, 4000-4500 feet) can be more easily correlated between wells. In general, the shallower (e.g. 762 meters, 2500 feet) Miocene sediments at Hastings cannot be correlated between wells, interpreted as an indication of a lack of hydrologic connection. This transition from continuous to increasing heterogeneity has been shown to affect CO_2 storage capacity in other Gulf Coast fields (Ambrose et al., 2008), and presents challenges when identifying candidate monitoring formations that could yield the highest probability of signal detection. Above the Miocene sandstones are the two major regional sandstone aquifers used for drinking water in this portion of the Gulf Coast, the Chicot and Evangeline aquifers.

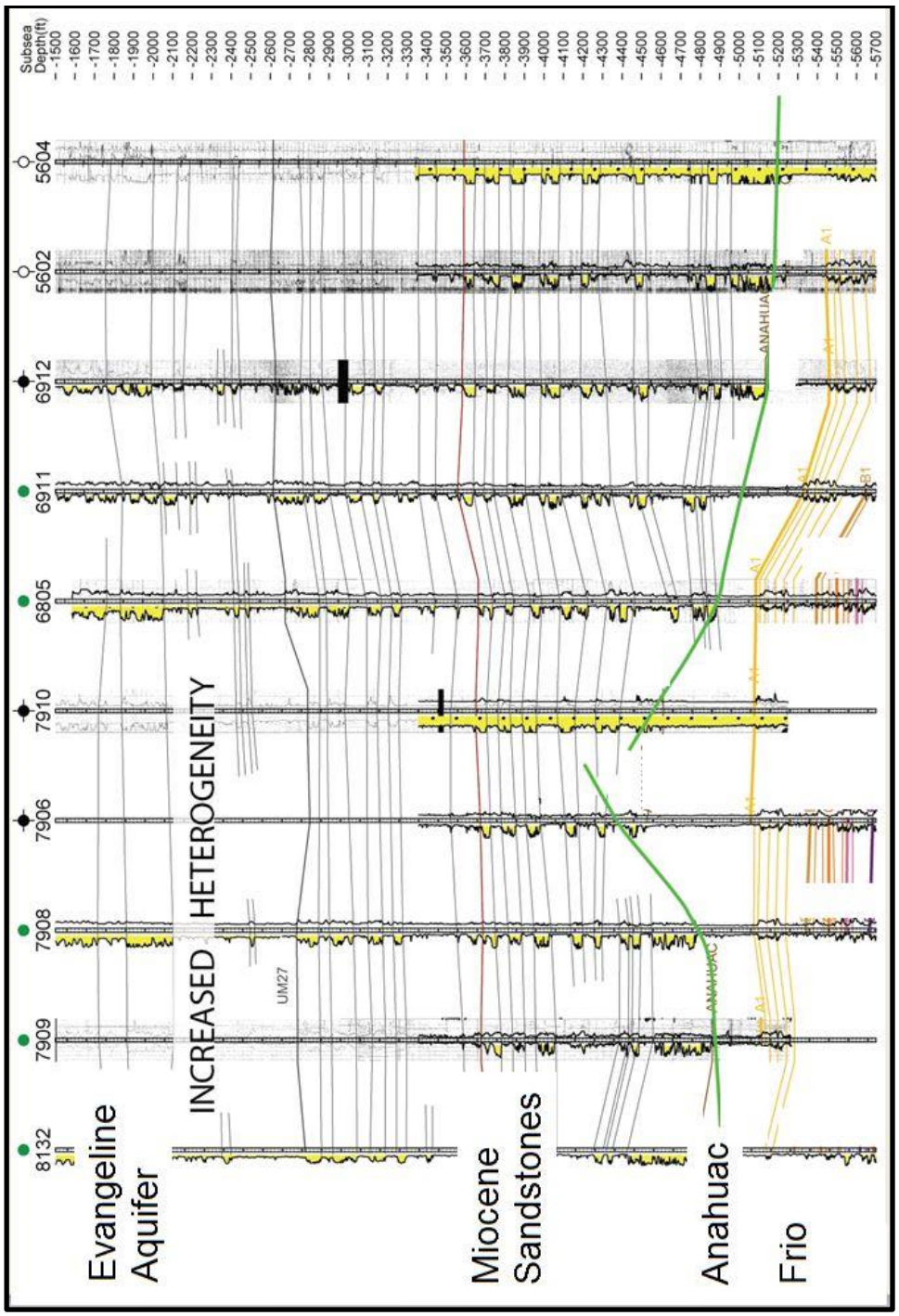

Figure 2.2: Cross section from SE (A') to NW (A) across Fault Block C, West Hastings. Green lines denote inferred faults above Anahuac. Refer to Figure 2.1 for cross section transect in blue.

Figure 2.3 shows a generalized Hastings Field stratigraphic column based on Figure 2.2 that is simplified to support modeling for this thesis. It features the Upper Frio Sandstone, overlain by the Anahuac Shale, followed by a number of alternating Miocene sandstones (brown) and confining units (yellow), overlain by two regional Gulf Coast aquifers, the Evangeline and Chicot. The column identifies eleven Miocene sandstones (e.g., M-14 to M-4) that are the focus of the AZMI (i.e., overburden geologic formations) research for pressure and geochemistry monitoring.

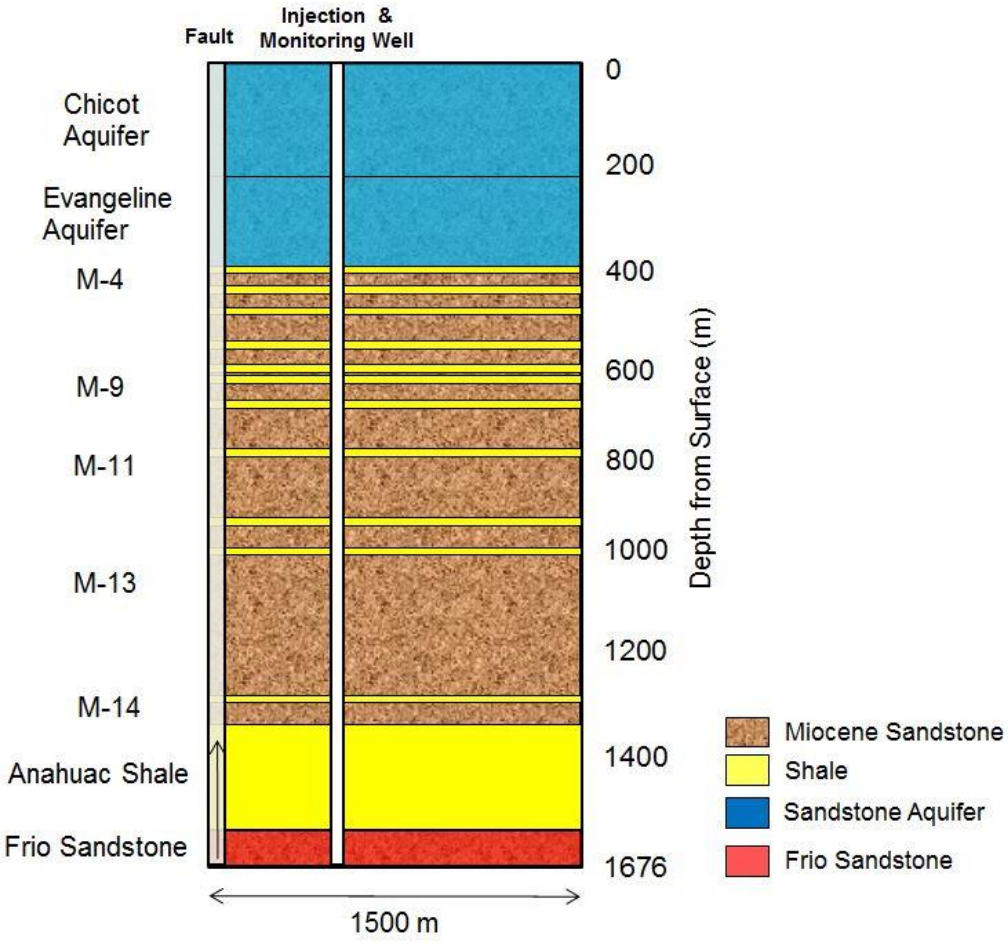

Figure 2.3: Simplified Hastings stratigraphic column.

WATER SAMPLING METHODS

For shallow groundwater sampling, BEG researchers identified ten existing Hastings shallow groundwater wells, which were sampled in March, April, and July of 2012 (Figure 2.4). See Appendix A for a complete listing of sampled Hastings wells and chemistry results. Of these ten samples, one was a deep brine sample from well (WHU) 4831, in the M-14 formation obtained from a depth of approximately 1372 meters (4500 feet) (Figure 2.4). For each well, the following physical and chemical water parameters were measured via probes or sample analysis: pH, specific conductivity (SpC), total dissolved solids (TDS), oxygen reduction potential (ORP), dissolved oxygen (DO),

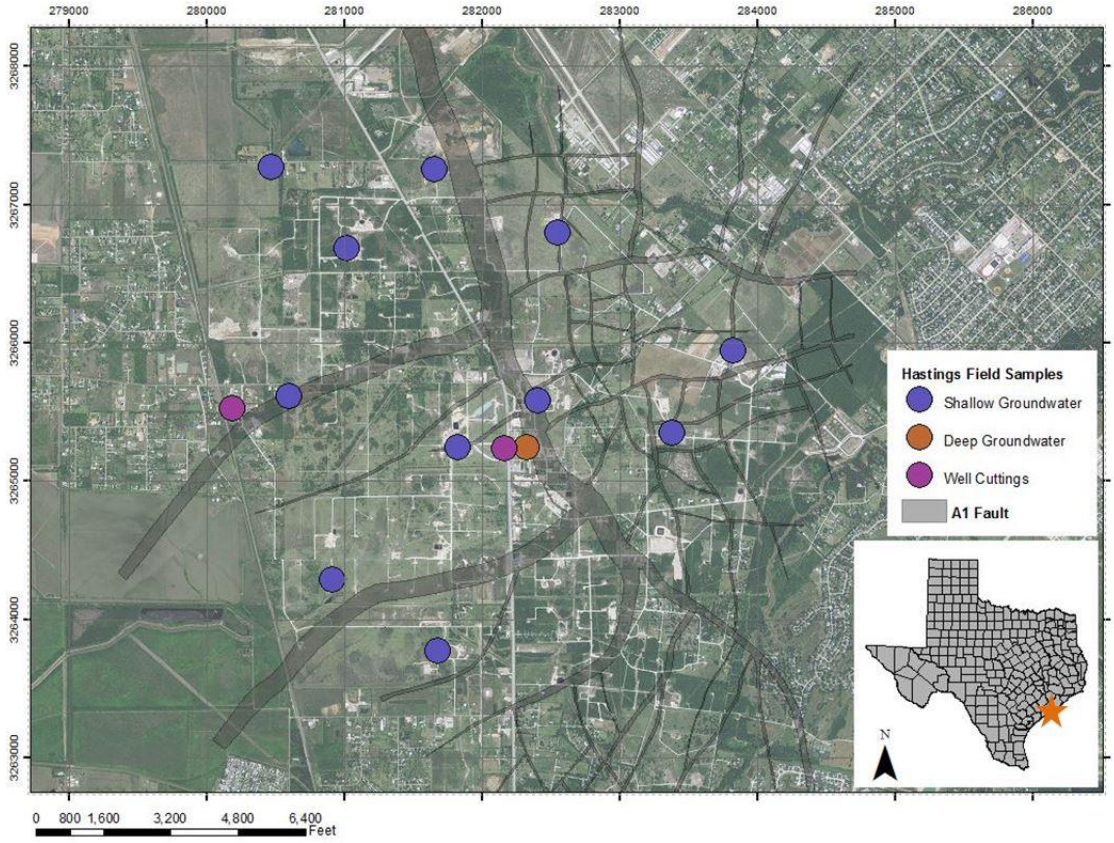

Figure 2.4: Locations of sampled groundwater and lithology cuttings, Hastings Field.

total alkalinity (TA), major cations and anions, trace elements, and dissolved inorganic carbon (DIC). To measure and sample these wells, standard United States Geological Survey (USGS) methods were used from the Field Methods Catalog for preparing, collecting, cleaning, and processing water samples (USGS, 2006).

After identification, candidate wells that were open to atmosphere and surface contamination were cleaned by high pressure water jetting downhole to remove any debris and other materials that would prevent shallow formation sampling. For the M-14 sample, the brine was sampled at pressure directly from a spigot off of the well that transports water from the M-14 to the surface. For each well, a sampling kit was created that included: two 60 ml polypropylene (PPE) unacidified bottles for cation and anion water samples, two 10 ml PPE bottles for trace element concentrations, two 40 ml amber VOA vials for stable isotopes and dissolved inorganic carbon concentrations. In addition to sample packs, field, and travel blanks of deionized (DI) water were sampled, sealed, and transported for each field trip to ensure no contamination occurred during transport. Field meters to measure chemical and physical parameters at Hastings included a multimeter (Hydrolab Quanta Multimeter and SDI-12 Data Logger, Loveland, CO) and a pH probe (Orion 4-Star Model 80-05, Thermoscientific), and were calibrated before the field sampling to ensure measurement accuracy.

When sampling groundwater at Hastings, total depth of the well and water levels were measured when possible using an electric line and plumb line. Total depth and water levels are necessary to properly calibrate the sampling depth of groundwater. For wellheads that could not be removed, no water or total depth levels were measured and estimates were made on well depths. After establishing well depth, a submersible pump (Redi-Flo 2, Model A1A106003 P1 0637 0009 Grundfos, Olathe, Kansas) was lowered into the borehole (see Figure 2.5). The pump was regulated by an Electric Controller

Figure 2.5: Shallow groundwater sampling set up, Hastings Field, March 2012.

(Serial #: H0912020046), and powered using a 5 kW Honda generator. In general, water level was around 160 feet below ground surface, excluding the M-14 brine sample (Appendix A). Before sampling, the well was purged for roughly three times casing volume, or until measurement parameters on the multimeter (e.g. pH, TDS, ORP, DO) stabilized. For the entire sampling procedure, laboratory-grade latex gloves were used to minimize contamination of groundwater samples.

Collected samples were preserved depending on the analysis. For cation and trace element samples, 2% Nitric acid was added (e.g. 2 ml of a six molar HNO_3 concentration in 60 ml water sample) for sample preservation. Anion and DIC samples were not acidified. For VOA vial samples, each sample taken was capped with no headspace to prevent atmospheric contamination of samples before laboratory analysis. Total alkalinity was measured in the field using a field titration kit (Model AL-DT, Hach, Loveland, CO)

to minimize atmospheric exchange of carbon. The inflection point method, which determines the carbonate and bicarbonate endpoints of a titration by finding the greatest change in pH per volume of sulfuric acid added, was used per USGS field sampling method recommendations (USGS, 2006).

Major cations and anions were measured using two ion chromatography systems (Dionex ICS-2000), equipped with auto-eluent generators, and a AD25 absorbance detector at the BEG's Geochemistry Laboratory. Trace elements were analyzed on an Agilent 7500ce quadrupole inductively coupled plasma mass-spectrometer (ICP-MS) at the Department of Geological Sciences at The University of Texas at Austin.

GRAIN SIZE PREPARATION AND ANALYSIS

Another important input parameter for each model was obtained from the grain size distribution of different Hastings geological units. Grain size distribution can significantly affect hydraulic parameters (i.e., porosity and permeability) of a porous media (Masch, 1966). Such distributions were estimated on fourteen Hastings lithology samples using a laser particle size analysis (LPSA; Master Sizer 3000, Malvern, Worcestershire, UK) located at the Desert Research Institute in Reno, Nevada. The LPSA method scatters monochromatic coherent light through a falling fluid sediment column and identifies grain size based on equivalence to a sphere that gives the same diffraction as the particle being measured (Konert, 1997). The Master Sizer 3000 has a working range of 0.01 μm - 3500 μm. To examine the grain size distribution of Hastings material, a combination of existing cuttings and fresh well cuttings were used. The University Of Texas Core Research Center (CRC), part of which is located in Austin, houses one of the world's largest collections of core and rock material, provided a limited selection of historical East and West Hastings drill cuttings from wells drilled in the 1970s. Of this

selection, only a few had cuttings within potential monitoring intervals of interest (e.g. 914-1524 meters/3000-5000 feet below ground surface). These wells include WHU 6604, 7502, 7202. Of these final picks, only WHU 6604 supplied enough sample to be processed, from a depth interval of 1524 to 1615 meters (5000 to 5300 feet) below ground surface (Figure 2.4).

In addition to existing cuttings from the UT CRC, in July 2012 Denbury drilled a new production well (WHU 7240) near the main field office in the West Hastings portion of the oil field (Figure 2.4). WHU 7240 yielded 165 sediment cutting samples in depths ranging from 548 meters (1800 feet) to 1920 meters (6300 feet) at roughly 9 meters (30 feet) intervals. The samples were raw (i.e., drilling mud included) at time of collection. Of these samples, eight were chosen as they covered specific formation intervals of interest, from 980 to 1557 meters (3218 to 5110 feet). The raw sediment samples required preparation to isolate lithology grain samples from drilling mud, and to remove organic matter, carbonate and iron oxide particulates before LPSA analysis. Pretreatment methods commonly used in soil sciences were applied to the Denbury-collected sediment samples (Gee and Or, 2002). The goals are to remove any exogenous materials and to separate particles into individual grains. Before chemical treatment of each chosen sediment sample, wet sieving (2 mm and 0.044 mm) removed coarse drill bit and fossil fragments, while allowing fine drilling muds to pass through completely, removing them from the sample. This process was repeated as necessary with DI water to remove and clean as many of the grains before subsequent chemical treatment. After wet sieving, samples were dried overnight in an oven at 60^{o}C.

Following Gee and Or (2002) carbonates and soluble salts were first removed from the dried sediment samples by centrifugation. First, approximately 60-80 grams of each sample, < 2 mm fraction, was placed into a 250 ml centrifuge bottle. Approximately

100 ml of DI water was added, and mixed along with 10 ml of 1 M Sodium Acetate (adjusted to pH 5). This mixture was then centrifuged for 10 minutes at 1500 rpm until the supernatant became clear. The supernatant was then removed, after which the sample was washed twice by shaking with 50 ml of DI water, centrifuging, and discarding the supernatant until clear. After carbonates and soluble salt removal, removal of organic matter was necessary.

To do this, 25 ml of DI water was added to the carbonate-treated sample in a centrifuge bottle and placed on a wrist shaker overnight. Afterward, the mixture was transferred to a 1000 ml beaker, augmented with 5 ml of hydrogen peroxide, stirred, covered and observed for frothing. If excessive frothing occurred, the mixture was cooled in a cold water bath until frothing ceased, and then heated to 90 ^{o}C to remove excess water. This process was repeated as necessary as long as organic material appears present. The mixture was then heated for about an hour after to destroy excess hydrogen peroxide.

The final step toward preparation for LPSA analysis is removal of iron oxides. Initially, a citrate-bicarbonate buffer was added to the peroxide-treated sample in the centrifuge bottle to bring the total volume of solution to approximately 150 ml. Three grams of sodium dithionite was then added gradually to prevent frothing, and the mixture was heated in a water bath at 80 ^{o}C and stirred intermittently for twenty minutes. The mixture was then removed from the bath, after which 10 ml of saturated NaCl was added, mixed, centrifuged, and centrifugate decanted. If the sample color was grey, treatment could continue to the next step; but, if a brownish color remained, the previous step was repeated. After turning grey, the sample was washed once with 50 ml of citrate-bicarbonate buffer plus 20 ml of saturated NaCl. This mixture was then shaken, centrifuged, and decanted. Finally, the mixture was washed twice with 50 ml of 10%

NaCl, then twice with 50 ml of distilled water. Results from grain size preparation analysis can be found in Appendix B.

X-RAY DIFFRACTION PREPARATION AND ANALYSIS

To incorporate Hastings lithology composition data into each model, X-Ray Powder Diffraction (XRD) was performed by researchers at the Gulf Coast Carbon Center. Samples from WHU 7240 in the M-4, M-5, M-6, and M-10 formations were processed for XRD analysis, where samples were primarily coarse sand dominated. A clay fraction was present however, so methods from Hillier (1999) were used to ensure that the sediments were analyzed in a completely random arrangement.

Samples were first washed twice in deionized water, and then dried in a soil oven at 60° C overnight. Samples were then dispersed in an aqueous solution with 20-30 milliliters polyvinyl alcohol (PVA) depending on the amount of clays. For those samples with high clay size fractions, a single drop of 1-octanol was added to prevent foaming during dispersion. Properly suspending the solution required the alcohol-sediment solution to first be mixed for 6 minutes in a Sample Prep 8000 Mixer/Mill (Spex, SN: 10115, Metuchen, NJ) with steel ball bearings, after which the suspended solution was crushed and mixed further in a Micronizing Mill (McCrone, Westmont, IL) in 125 milliliter plastic vials with 12 cylinder grinders for 16 minutes. This solution was then placed into 50 mL stout glass bottles, and then sprayed with 10-15 psi of compressed air through an air brush into a superheated cylinder that is 45x90 cm tall. Temperatures within the cylinder remain at a constant 150 °C, which will quickly dry the size fraction particles into randomly oriented, similarly sized powder samples (<2μm). These particles were collected at the bottom of the cylinder on a white poster board, and then carefully transferred to a 25 mL stout glass bottle for storage until XRD analysis can occur. An

AXS D8 diffractometer (Bruker, Madison, WI) at The University of Texas at Austin was used to analyze the prepared samples. Results from XRD analyses are in Appendix C.

ANALYTICAL AND NUMERICAL MODELING

To evaluate the sensitivity of each monitoring technology at Hastings, analytical and numerical models were used to help address the initial hypotheses. The analytical model that solves for pressure perturbations is obtained from Zeidouni (2012) while the geochemical model is a USGS-based open source numerical model called PHAST (Parkhurst, 2005). Both models share similar conceptual formation geometry (Figure 2.3), constructed based on a few motivations. First, operators have produced hydrocarbons in the Gulf Coast of Texas since the 19th century, leaving a legacy of many known and unknown wells. These wells are in various states of use and abandonment, and combining with the sheer number of penetrations, some may be improperly constructed or damaged providing conduits for fluid migration (Nicot et al., 2009). Second, while the sealing capacity of faults at oil and gas fields is demonstrated by hydrocarbon accumulation over geologic timeframes, some uncertainty remains on the geomechanics of fault seals, and their potential for allowing migration. To account for both types of uncertainties, AZMI monitoring can be used to look for evidence of fluid communication between a reservoir and a shallower formation. In designing a monitoring plan, questions that should be quantitatively addressed ahead of time are: 1) which zone(s) to monitor, and 2) which method(s) should be used. For Hastings, while both wells and faults exist, no single risk has been identified. This uncertainty is addressed probabilistically by modeling a geologic fault, crosscutting all formations vertically, that allows testing of different monitoring parameters' sensitivity in AZMI formations and lateral distances. In Figure 2.3, simulated single phase brine injection occurs on the right

hand side of each model, migrating towards the postulated open fault migration pathway on the left hand side and then upwards and into respective AZMI formations (i.e. M-4 to M-14). Pressure and geochemistry changes will be systematically sampled in each AZMI formation, at varying lateral distances from 50 to 500 meters away from the modeled fault. A full breakdown of all AZMI formations, depths, and chemistries is found in Appendix D.

Analytical Model for Pressure

The analytical model is coded and processed through the program interface MATLAB and evaluates the fluid migration rate vertically up a fault and corresponding pressure changes in the injection zone and specific above-zone monitoring intervals (AZMI). The model solves analytical solutions for two-formation and multiple AZMI formations scenarios as well as both vertical and horizontal resistances to flow through a fault and subsequent formations (Zeidouni, 2012, Figure 2.6).

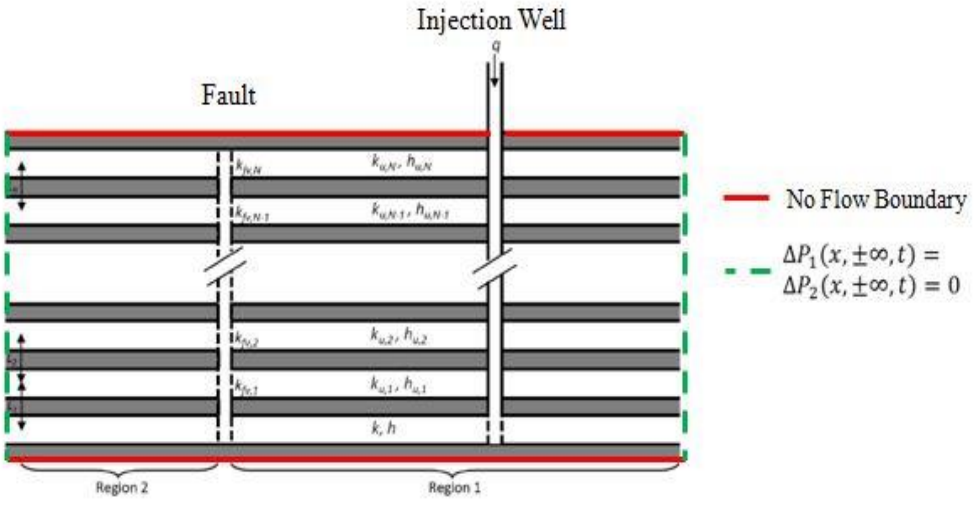

Figure 2.6: Pressure model geometry from Zeidouni (2012) where k is formation permeability, h is formation thickness, and q is the injection rate. This study focuses on Region 1 only.

No-flow boundaries bound the top and bottom of the model, with a single fault splitting the domain into regions, 1 and 2. While fluid migration occurs in both regions, monitoring activities occur only in Region 1 (Figures 2.3 and 2.6). Prior to model initiation, pressure is assumed to be hydrostatic throughout the model domain. The lateral extent of the model is semi-infinite, where the change in pressure in regions 1 and 2 are negligible at towards the infinite lateral boundaries (dashed green line; Figure 2.6).

Primarily, the boundary conditions that control flow within this model come from the fault assumptions, with flow outward from the fault boundary at any given depth location being the sum of flow toward region 1 and vertical fluid outflow at a given point in the fault. Appendix E, from Zeidouni (2012), provides an in depth discussion on the pressure solution, which involves solving and transforming Darcy flow equations successively into Laplace and Fourier transform, and solving for the resulting differential equations. Table 2.2 lists selected model input parameters. One note: the injection rate of 0.0453 m^3/s equates to $1x\ 10^6$ metric tons fluid/year, which is a hypothetical injection rate. Full input parameters can be found in Appendix D. Additionally, initial sensitivity studies determined that model fault width, and overlying AZMI formation permeabilities had the largest effect pressure migration results from base case model specifications (Figure 2.7).

To understand the sensitivity of the input on output parameters, Monte Carlo analyses are conducted to systematically vary fault width and formation permeabilities for 100 realizations over 100 years. Monte Carlo methods are a class of computational approaches that run a specific model through multiple realizations while randomly sampling model specific model parameters from a set of values. Such modeling has been used by the groundwater modeling community to vary heterogeneous media in 3D flow

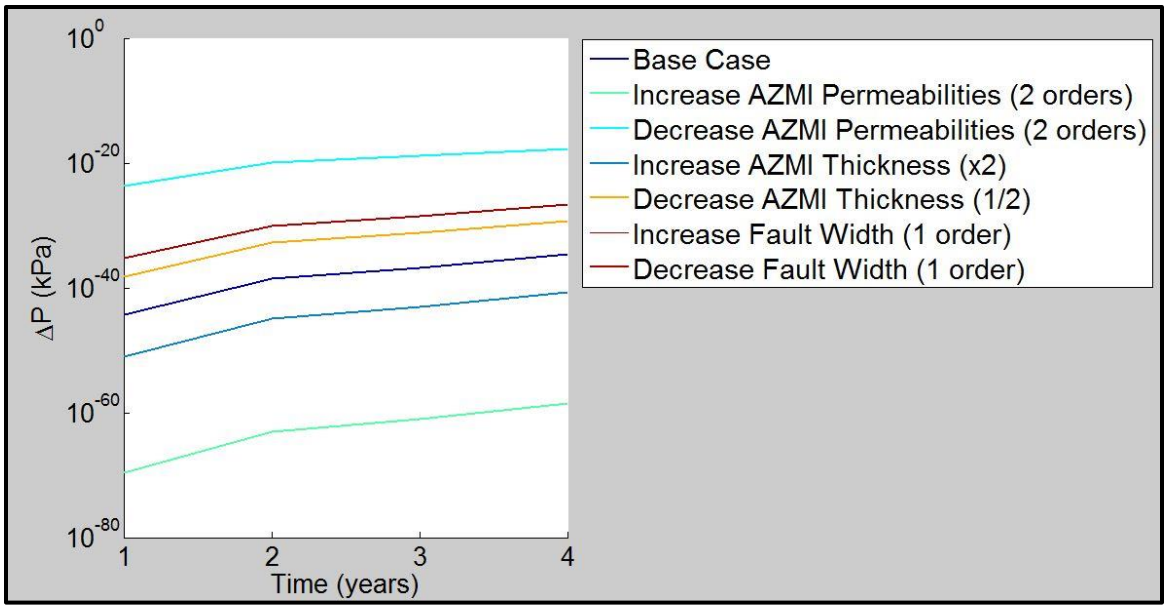

Figure 2.7: Selected pressure model sensitivity results comparison to base case.

Pressure Model Parameters	Value	Units
Injection Rate, q	0.0453	m^3/s
Frio Permeability, K	4.65e-13	m^2
Frio Porosity, Φ	0.3	
Frio Thickness	40	m
Frio Diffusivity Coefficient	1.55	m^2/s
Fluid Viscosity	1e-03	Pa.s
Fluid Compressibility	1e-09	1/Pa
Injection Well – Fault Distance	500	m

Table 2.2: Select pressure model input parameters.

and transport modeling (Burr et al., 1994; Naff,et al., 1998) as well as the GS research community to evaluate the human health risks from CO_2 leakage into groundwater (Siirila et al., 2012). Fault width values were obtained using Latin Hypercube Sampling (McKay et al., 1979, LHS) from a normal distribution around 1.68 meters width, which is an arbitrary value. Formation permeabilities were sampled from a compiled database of empirically calculated values from previously collected Hastings sidewall core samples. A beta distribution was assigned to the Hastings permeability dataset because: the beta distribution best fit the data (Appendix E) and to eliminate sampling a negative permeability value.

Pressure results are initially reported as a dimensionless pressure rate change (PDm). These results are converted to kilopascals (kPa) in equation 2.1:

$$\Delta P = (q * \mu * PDm)/(1000 * k * h) \qquad (2.1)$$

where q is the injection rate (m^3/s), μ is fluid viscosity (Pa.s), PDm is the dimensionless pressure value, k is the hydraulic conductivity of the injection zone formation (m^2), and h is the injection zone thickness (m). To determine the practicality of the pressure model results, minimum detection limits were used to delineate when parameter changes were high enough to be detected. Minimum detection limits were used to delineate when parameter changes were high enough to be detected by commercially available pressure gauges, in this case a Schlumberger down-hole Quartz Series TQPR Pressure gauge's 0.005 psi/0.03 kPa (Schlumberger, 2006b).

Numerical Model for Geochemistry

The numerical model PHAST, an open-source USGS based code that integrates the multicomponent geochemical reaction model program PHREEQC with a solute-transport simulator, HST3D, is capable of modeling a wide range of equilibrium and

kinetic geochemical reactions, including reactive transport of brines from hydrocarbon. production activities (Parkhurst, 2005). The governing equations used to solve the groundwater transport portion of PHAST, based on Kipp (1997) are:

$$Ss\frac{\partial h}{\partial t} = \nabla \cdot K\nabla h + q \qquad (2.2)$$

where $h = \frac{p}{\rho g} + z$ equals the potentiometric head (pressure, $\frac{p}{\rho g}$, and elevation, z) in meters, Ss is the storage coefficient of the formation (per meter, m^{-1}), ∇ is the divergence operator for vectors (m^{-1}), K is the hydraulic conductivity (m/s), and q is the flow rate (m^3/s). For all PHAST realizations, Ss was held constant at 1 x 10^{-4} m^{-1}, q was held constant at 1x 10^6 metric tons/year, and density, ρ, and gravity, g, are also held constant. All values represent realistic conditions, but are not directly derived from Hastings.

PHAST requires three data files to operate; a chemical data file that details all aqueous, solid solution, and equilibrium phase chemistries, a transport file that details the modeling domain to be solved by finite difference techniques for solute transport, and a chemical database file, phast.dat (PHAST offers multiple types of databases depending on the anticipated reactions). The code splits these files and independently solves the advection-diffusion-dispersion and saturated transport equations, in this case for the migration of groundwater from an injection zone into overlying AZMI formations (Figure 2.8). While PHAST can accurately model a number of reactive transport methods, it cannot simulate vadose zone flow interactions, nor can it simulate multi-phase flow such as gas, non-aqueous phase liquids, which can be done through more advanced reactive-transport simulation programs such as TOUGHREACT (Xu et al., 2006) and STOMP (Hou et al., 2012).

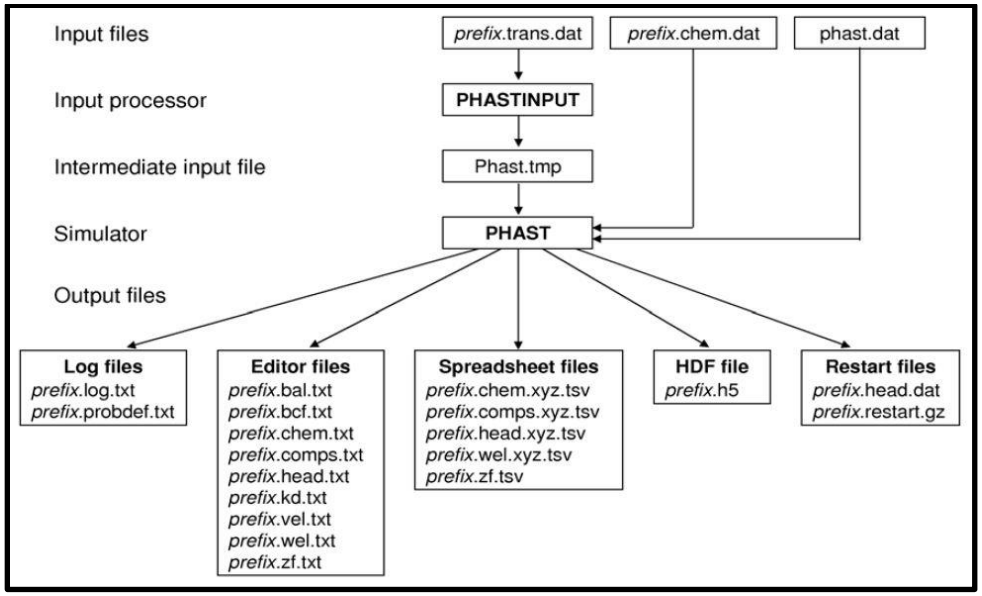

Figure 2.8: Diagram of PHAST program splitting and solving for a set of input data (Parkhurst, 2005).

Two different chemical elements are modeled as tracers, chlorine and bromine. Together, chlorine and bromide are present in potable water as monovalent ions chloride (Cl^-) and bromide (Br^-). Both Cl and Br infiltrate shallow and deep groundwater systems through a number a ways, including atmospheric deposition, dissolution of subsurface evaporites, diffusion of ions out of saline fluid inclusions, as well as other means. Both elements can be used as tracers due to their conservative behavior when ionized in water (i.e., they do not readily adsorb to geologic media). Additionally, while Cl is soluble in water, Br has an even greater relative solubility, and will remain in solution longer than Cl. This characteristic is important for helping to determine water and brine formation characteristics.

The initial program PHAST can be solved deterministically (i.e., a user inputs a set of parameters to satisfy groundwater flow equations, but cannot input distributions of parameters). Table 2.3 lists selected initial parameters and Appendix D lists all

geochemical model physical and chemical parameters. Permeability values are based on the aforementioned permeability value dataset obtained from sidewall core data, porosity values are general values representative of given lithology (i.e., sandstone and shale), and chemistry values are sourced from a combination of BEG-collected water samples and Denbury-provided Frio water sample results. Initial boundary conditions are also shown in Figure 2.3. For each Miocene formation, the model has a semi-infinite lateral (i.e., 1500 meters) boundary on the right side of the domain to minimize interactions with lateral boundaries. A potentiometric head value is specified relative to the z-axis, with an assigned solution type to each condition, and varies over time with the flux of water through the boundary relative to the current composition of the cell (Table 2.3 and Appendix D). A flux of 0.116 meters per day across 20 m^2 in area at the bottom of the left hand side of the model domain drives fluid migration. This flux rate equates to a migration rate of roughly 1,000,000 Mt of brine per year over the volume equivalent of fault blocks B and C in West Hastings (Figure 2.1). Similarly to the pressure model, the injection rate does not represent current operational parameters at Hastings. To vary select parameters, a function was written in MATLAB that calls on PHAST, runs the geochemical model by implementing all three input files and systematically varies specific model parameters. Similar to the analytical pressure solution, the sensitivity of various formation permeabilities was tested by Monte Carlo analysis. Each model realization sampled water from a lateral distance range of 50 to 500 meters from the fault in 50 meter increments to determine chemistry breakthrough times, and mass flux. See Appendix G for the associated MATLAB code.

	Permeability (m^2)	**Porosity**	**Initial Chemistry Value**
Chicot Aquifer	4e-09	0.3	4
Evangeline Aquifer	7.28e-10	0.3	4
M-4	9.87e-17 to 2.7e-12	0.3	3
M-5	9.87e-17 to 2.7e-12	0.3	3
M-6	9.87e-17 to 2.7e-12	0.3	3
M-7	9.87e-17 to 2.7e-12	0.3	3
M-8	9.87e-17 to 2.7e-12	0.3	3
M-9	9.87e-17 to 2.7e-12	0.3	3
M-10	9.87e-17 to 2.7e-12	0.3	3
M-11	9.87e-17 to 2.7e-12	0.3	3
M-12	9.87e-17 to 2.7e-12	0.3	3
M-13	9.87e-17 to 2.7e-12	0.3	3
M-14	9.87e-17 to 2.7e-12	0.3	3
Anahuac Shale	9.99e-19	0.1	2
Frio Sandstone	9.87e-17 to 2.7e-12	0.3	1
Confining Units	9.8e-20	0.1	2

Table 2.3: Select PHAST Input Parameters. Refer to Appendix D for chemistry values.

An important consideration for quantitative comparison between these models is maintaining consistency for each respective model's assumptions. Both models simulate Darcy-type flow in a saturated porous media; however, the solvers used for each vary. The analytical model uses a set of partial differential equations processed through

Laplace and Fourier transform space, while the numerical solution relies on finite difference solving methods (Appendices E and F). However, while inherent differences exist in solving for each respective solution, maintaining consistency with boundary conditions, fluid migration conditions, and field parameters helps to keep quantitative comparison valid. Both models have semi-infinite lateral boundaries, no flow boundary conditions at the top and bottom of the model domain, and they share the same geometry for the fault domain. For PHAST flux values, the goal was to equate both injection rates and fluxes from each model to represent the same migration rate of 1,000,000 Mt of brine annually.

The analytical model features one well that serves as the injection point (in orthogonal coordinates) for the analytical solution (Figure 2.6). In contrast, PHAST does not have an actual injection well, rather, the flux boundary represents migrating fluid generated by injection activity. A vertical fault cuts across each model domain entirely at the left hand side of the model. The Frio sandstone serves as the injection zone at a maximum depth of 1676 meters, with the Anahuac shale regional confining unit overlying the Frio. Above the Anahuac, eleven alternating Miocene-aged sandstones (i.e., M-sands) and generic confining units (i.e., shale) persist to 467 meters below ground surface. Above these alternating M-sand and confining units, the two major regional aquifers in the Gulf Coast of Texas, the Evangeline and Chicot aquifers, persist to the surface. Analyzing chemistry at specific model domain nodes is accomplished using two methods; first, sampling wells are installed at specific depths within the PHAST model to sample a small amount of fluid (i.e., 1e-40 m^3/d) as to ensure not to influence modeled flow, and second, by using MATLAB to plot temporal change of Cl and Br ion ratio concentration changes for each AZMI formation.

STATISTICAL COMPARISON METHODS

Undertaking a quantitative analysis of each model's data independently and in comparison to each method helps more fully assess the use of each monitoring type. For groundwater monitoring, a number of established methods to quantify probabilities of detecting fluid migration exist from the environmental remediation literature. These include prediction limits (USEPA, 2009), ion ratio comparisons such as Cl/Br ratios (Davis et al., 1998), rate of infiltration comparisons for determining fluid wetting front timing into the vadose zone (Young et al., 1999), and methods adapted from other industries such as signal to noise ratios (SNR) from the electrical engineering industry (Taguchi, 1986; Sun et al., 2013). The primary metric for determining the strength of a pressure signal for each AZMI formation is to use the minimum detection limit (MDL) for a commercially available pressure gauge, in this case the previously discussed Schlumberger Quartz TCPQ gauge, with a reported MDL of 0.03 kPa/0.005 psi. This comparison of resulting pressures to the MDL can help determine the degree of signal strength (and signal confidence); any changes in pressure above the MDL could help and owner or operator identify a potential change in subsurface conditions, indicating a release. However, Monte Carlo analyses inherently create a level of sampling uncertainty, resulting in a standard deviation due to systematic variation of formation hydraulic parameters. To account for this uncertainty, the standard deviation, σ, will be incorporated into each model's results. Standard deviation is a measurement of variation between a given value, and a dataset's average value, represented by the following equation (2.2):

$$\sigma = \left(\frac{1}{n-1}\sum_{i=1}^{n}(x_i - \bar{x})^2\right)^{1/2} \qquad (2.2)$$

where n is the number of elements in the sample, $\bar{x}$ is the mean, and x_i is a given sample from the number of elements n. By subtracting the standard deviation from the mean ΔP value, the largest source of uncertainty, the Monte Carlo sampling of specific model parameters, is eliminated. Other sources of uncertainty include the gauge measurements themselves; all gauges such as the Schlumberger Quartz TCPQ gauge have inherent drift (i.e., undesired change in the output reading for a gauge over a given amount of time; Omega, 1998). The drift of an instrument is measured at full scale output (i.e., the maximum working conditions a gauge can operate). In the case of the Schlumberger Quartz TCPQ gauge, a maximum drift of 0.02% of 110,000 kPa/16,000 psi (Schlumberger, 2006b). However, for the purposes of this thesis, drift is considered small enough that it is not incorporated into the pressure results.

Related specifically to geochemistry, the chloride to bromide ratio (Cl/Br) is used to determine brine impacts by helping to quantify the breakthrough and impact from brine migration into shallower AZMI formations. Comparing their natural occurrences, Cl is around 40-8000 times more abundant than Br in geologic media (Davis, 1998). Because of the contrast in natural abundances of each ion, comparisons using a Cl/Br ratio provide information on dominant mechanisms leading to estimated brine concentrations (Rittenhouse, 1967; Kesler et al., 1995; Weaver et al., 1995; Whittemore, 1995). Deep brine aquifers generally form by the evaporation and subsequent ion concentration of formation seawater, or through the dissolution of marine evaporites. From the ion properties discussed above, neither Cl nor Br readily precipitate into minerals. However, under extreme evaporitic conditions, halite precipitation can occur which removes Cl from solution and leaves Br and markedly decreases the Cl/Br ratio (Kesler et al., 1995; Alcala, 2008). Based on this general relationship between elements, the ratio has been applied at oil and gas fields to evaluate the mechanisms of brine, oil,

and gas migration (Morton et al., 1987; Land, 1995; Davis et al., 1998; Hyeong et al., 2001). For the PHAST model, because of the vertical fault setup, brine transport is expected to be efficient and conservative (i.e., no retardation by reactive transport) making it an ideal ratio to examine the modeled sensitivities of geochemical signal monitoring.

Typically in Texas Gulf Coast oil fields, shallow groundwater systems that have interacted with deep brines, from legacy oil field activities such as surface brine disposal, have Cl/Br ratios between 300-400 (Kesler et al., 1995). Production intervals such as the Frio Sandstone can have Cl/Br ratios from 600-800, depending on the presence of salt piercement domes. Such domes, like the one present just east of Hastings (Figure 2.1), can contribute significantly more Cl than Br via brine migration to shallower formations through halite dissolution and migration upward through faults and fractures. For example, the Chocolate Bayou and Alta Loma Fields, both located regionally near the Hastings field on the Gulf Coast of Texas, have Cl/Br ratios around 830 within the Frio, similar to ratios found at Hastings (e.g., 865) (Morton et al., 1995). Br is also used as a conservative introduced tracer (LeBlanc et al., 1991; Yang et al., 2013).

Rather than quantifying model results through field-specific ratios, the rate of change for both the ΔP values and Cl/Br ratios is the primary indicator of brine migration into shallower AZMI formations. Specifically, this rate change is evaluated by taking the first, and second derivatives of each pressure and geochemical value. The first derivative represents the change in slope of a given function, $f(t)$ given by the following Equation (2.3):

$$\frac{dy}{dt} = \frac{f(t+\Delta t)-f(t)}{\Delta t} \qquad (2.3)$$

where t represents time, in this case 500 day increments, and $f(t + \Delta t) - f(t)$ is the difference between two values at two different times t, and Δt is the change in time, in this case a constant 500 days. This thesis uses the derivative approach because it provides a consistent and objective point in time signifying arrival of changes in either pressure or geochemistry (as the Cl/Br ratio). This approach is particularly helpful for cases where background conditions differ as a function of vertical distance from the injection source, in the case for each M-sand. Here, a single threshold value to represent all M-sands would not work for both tested monitoring techniques. Therefore, identifying the point of greatest change in conditions is more useful and practical.

Using Br as an example, as Br migrates through a given Cl-dominated formation, the Cl/Br ratio of the formation fluids will begin to decrease. The first derivative helps determine at what point the greatest decline of the Cl/Br ratio occurs. The smallest (i.e., most negative) first derivative for each monitoring well in each M-sand formation represents the greatest negative slope, or the point in time when Br concentration increases most rapidly. The "arrival" point for pressure or Cl/Br ratio can also be identified using the second derivative. The second derivative is the derivative of the derivative of a function $f(t)$ and is a measure of the increase or decrease of a rate of change, in this instance, the change in the Cl/Br ratio. It is calculated through the following equation:

$$\frac{d^2y}{dt^2} = \frac{d}{dt}\left(\frac{f(t+\Delta t)-f(t)}{\Delta t}\right) \qquad (2.4)$$

where t represents a given time in 500 day increments, and $\frac{d}{dt}$ represents the first derivative. The smallest second derivative value (i.e., negative) represents the greatest

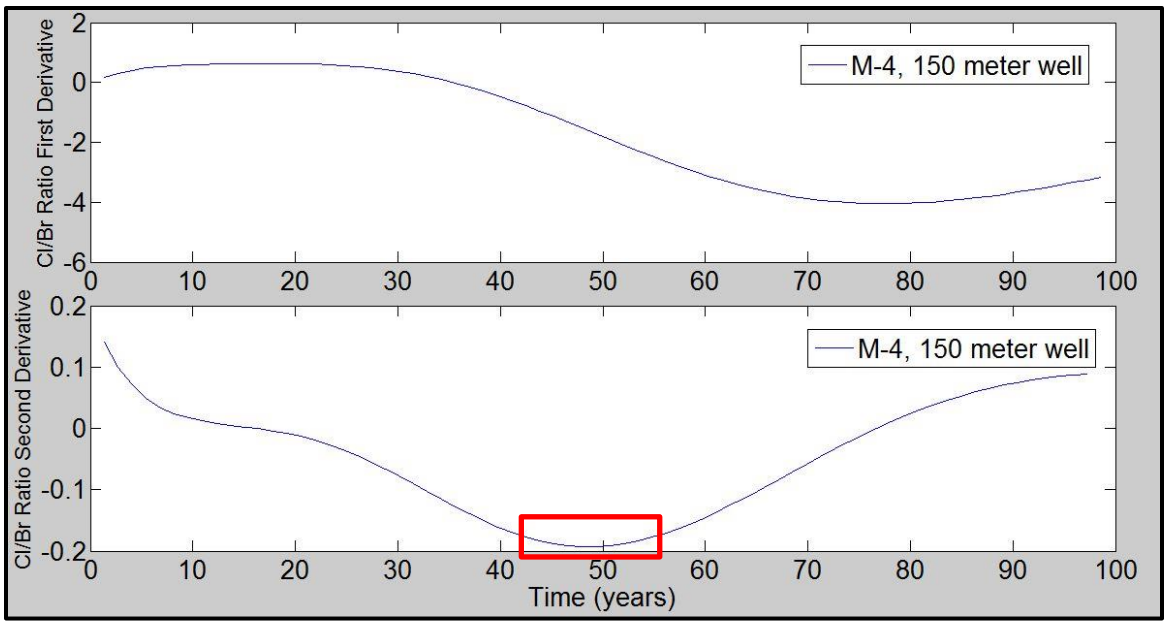

Figure 2.9: First and second derivative values in the M-4 formation at 150 meters. The box in second derivative plot highlights the greatest rate of decline.

rate of decrease in measured value, in this instance the Cl/Br ratio (Figure 2.9), for a given AZMI formation. The second derivative serves as the main delineator for arrival of injected fluid (containing a Br tracer) at a particular distance from the injection well, installed in a particular M-sand, and is particularly important for cases without satisfactory first derivative values.

In order to compare pressure and geochemistry signal occurrences, results must be standardized. Because the models use different programs to solve for equations at different time steps, data is interpolated between each known value to standardize the comparison at 500 days. Importantly, this standardization does not significantly influence any of the pressure values, but merely allows for improved comparison and subsequent plotting (Figure 2.10). This requires the pressure models values to be interpolated between each assigned time step of 0.1, 1, 2, 5, 10, 25, 50, and 100 years, at a rate of 1.37 years, or 500 days.

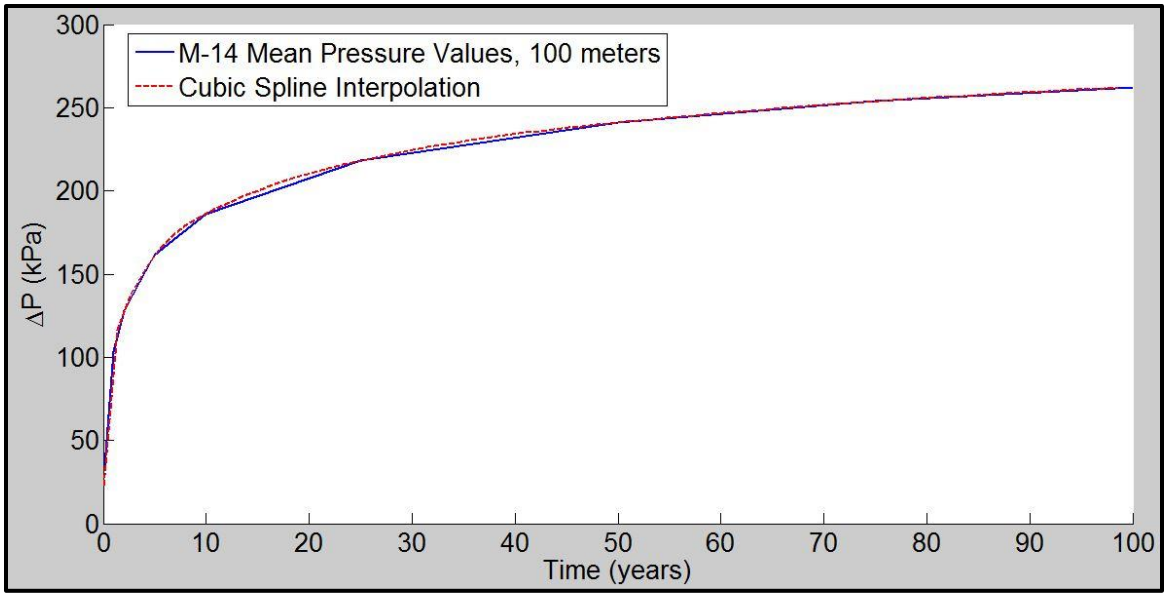

Figure 2.10: M-14 mean pressure and interpolated values, 100 meters.

To accomplish this, a cubic spline method (the MATLAB function *interp1*) interpolates between each known point. When run, the cubic spline interpolation creates an estimated value at a query point (in this case every 1.37 years) based on the values at neighboring grid points in each respective dimension (de Boor, 1978).

Chapter 3: Results

Results from the model simulations show different sensitivities for each type of monitoring. While pressure signals display a clear depth-to-use relationship, geochemistry monitoring signals show more complexity as a groundwater monitoring tool.

PRESSURE MODELING

Results from analytical modeling for migration of pressure changes demonstrate that as the monitoring depth shallows from the fluid migration source, the pressure signal weakens by an order of magnitude from the deepest to shallowest AZMI formations. Almost all pressure results, however, are above the minimum gauge detection limit (MDL, 0.03 kPa) during all or part of the 100 year monitoring period. Results of pressure changes (ΔP) in the M-14 formation after 100 realizations are shown in Figure 3.1, where the monitoring well (i.e., point) is 100 meters from the fault. Values vary from 41.46 kPa to 718.43 kPa at 100 years, with an average of 272.8 kPa. Importantly, results for all realizations lie above the MDL almost immediately after the start of injection and remain well above the MDL through the entire 100 year period. In contrast to results from the M-14 sand, pressure changes in the M-4 formation, approximately 900 meters above the M-14 formation, are weaker (Figure 3.2). Pressure values in the M-4 ranged from 2.03×10^{-22} kPa to 22.78 kPa at 100 years, with an average of 1.97 kPa. Average M-4 pressure change values do not rise above the MDL until approximately two years after the start of injection. Average M-4 ΔP values are weaker than deeper formations, but are strong enough to be detected by standard pressure gauge equipment.

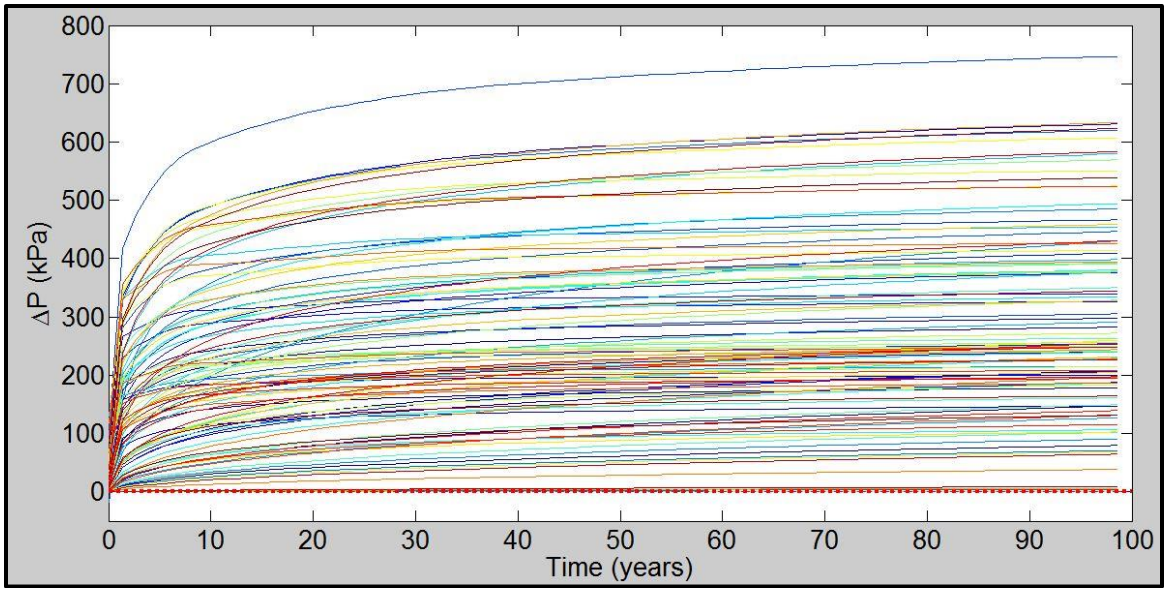

Figure 3.1: 100 pressure model results for the M-14 Formation over 100 years, 100 meters from the fault. The red dashed line represents the minimum detection limit of the pressure sensor (0.03 kPa).

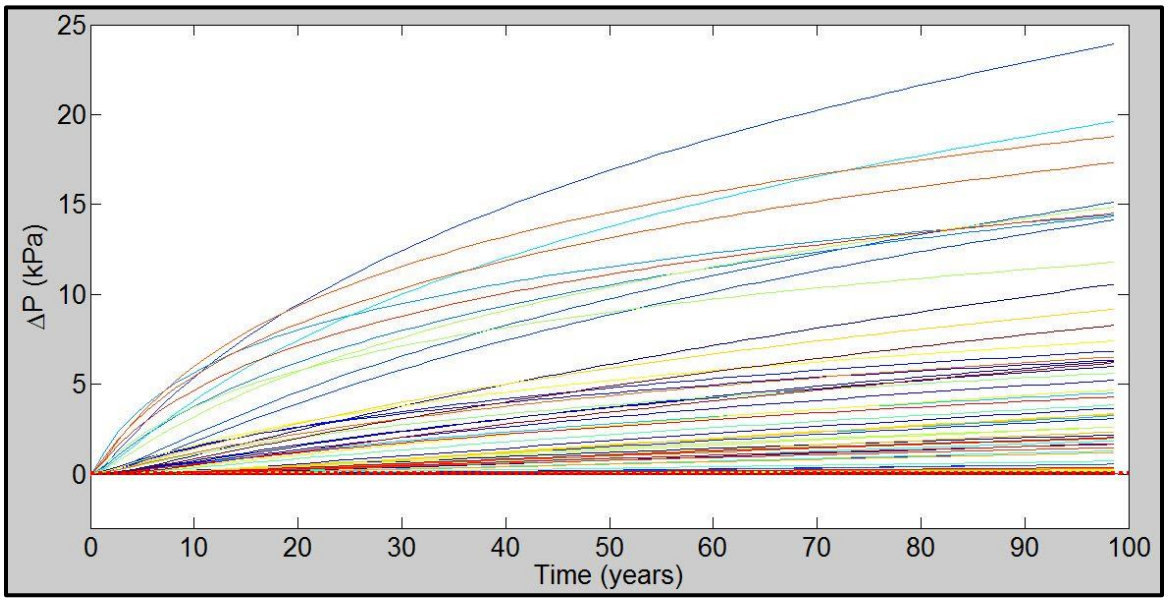

Figure 3.2: 100 pressure model results for the M-4 Formation over 100 years, 100 meters from the fault. The red dashed line represents the minimum detection limit of the pressure gauge (0.03 kPa).

Comparing Figures 3.1 and 3.2, it is clear that pressure signal decreases as AZMI formations shallow. Figure 3.3 visualizes this attenuation, showing the mean pressure change, plus or minus one standard deviation for all AZMI formations over 100 years. Similar to Figure 3.1, Figure 3.3 shows the mean pressure change in the M-14 formation above MDL for all time periods, as well as for almost all mean pressure values reduced by the standard deviation. However, while shallower formation ΔP values systematically decrease, these values remain above the MDL except in the shallowest formations. Pressures in the M-9 through M-4 formations are below MDL until 40 days after the start of injection when they rise above MDL. Pressure values in only the shallowest formations (i.e., Evangeline and Chicot aquifers) are below MDL after 40 days, where formation values persist below the MDL through two years after the start of injection. Figure 3.3 demonstrates that pressure changes occur above gauge MDL in all formations for almost all of the 100 year monitoring period.

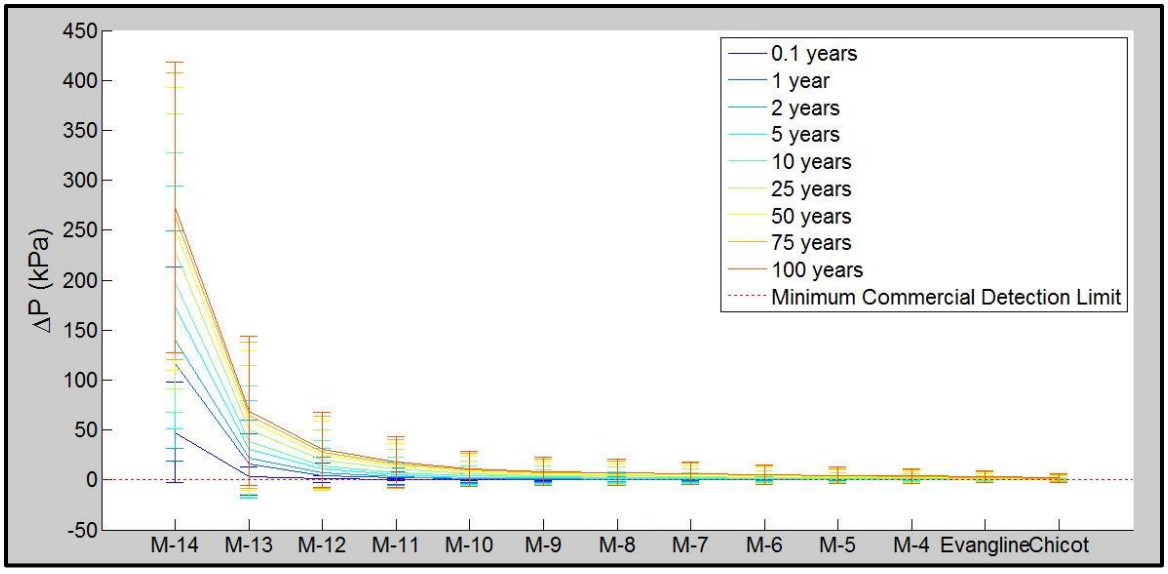

Figure 3.3: Mean (+/- one standard deviation) pressure change values for all AZMI formations, 100 years, 100 meters from the fault.

Pressure values decrease slightly with respect to vertical monitoring points closer to the leakage source at 300 and 500 meters laterally from the fault. The maximum mean pressure value in the M-14 formation at 300 meters is 260.2 kPa, while the maximum mean in the M-4 is 1.91 kPa (Figure 3.4). At 500 meters laterally from the fault, mean pressure values in the M-14 formation are a maximum of 251.86 kPa, while in the M-4 formations the greatest average is 1.88 kPa (Figure 3.5). Pressure values at 500 meters are similar to those at 100 meters, with the largest difference of 10.64 kPa in the M-14 formation after 100 years (262.49 vs. 251.86 kPa). The difference in pressures is even smaller between 300 and 500 meters, with a difference of less than 10 kPa (in the M-14 formations). Excluding M-14 formation comparisons, only the M-13 has differences in pressure values above one kPa at any lateral distance.

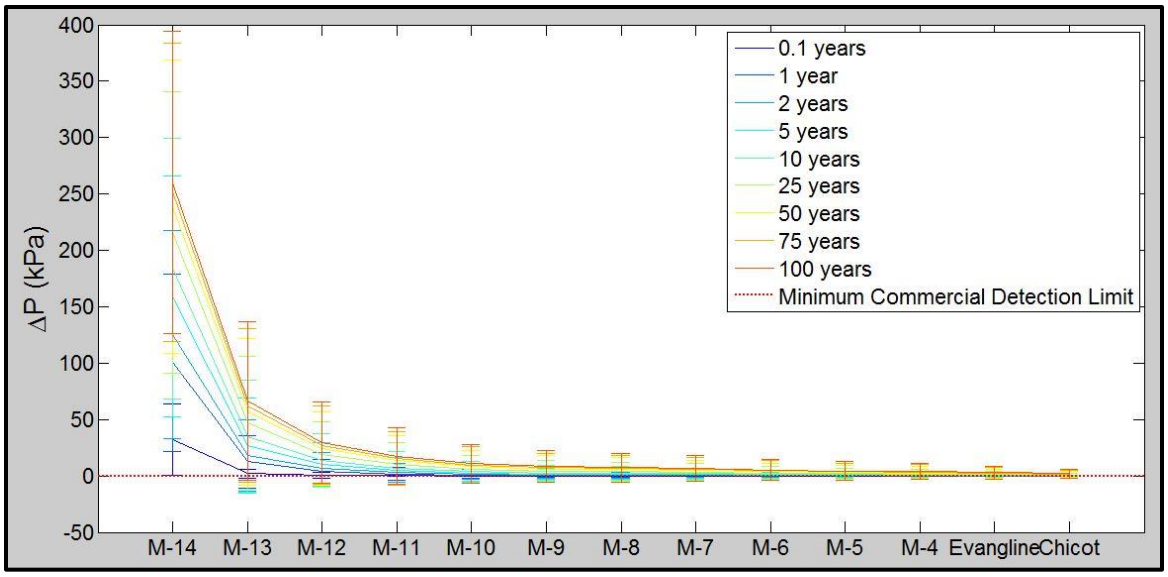

Figure 3.4: Mean (+/- one standard deviation) pressure change values for all AZMI formations, 100 years, 300 meters from the fault.

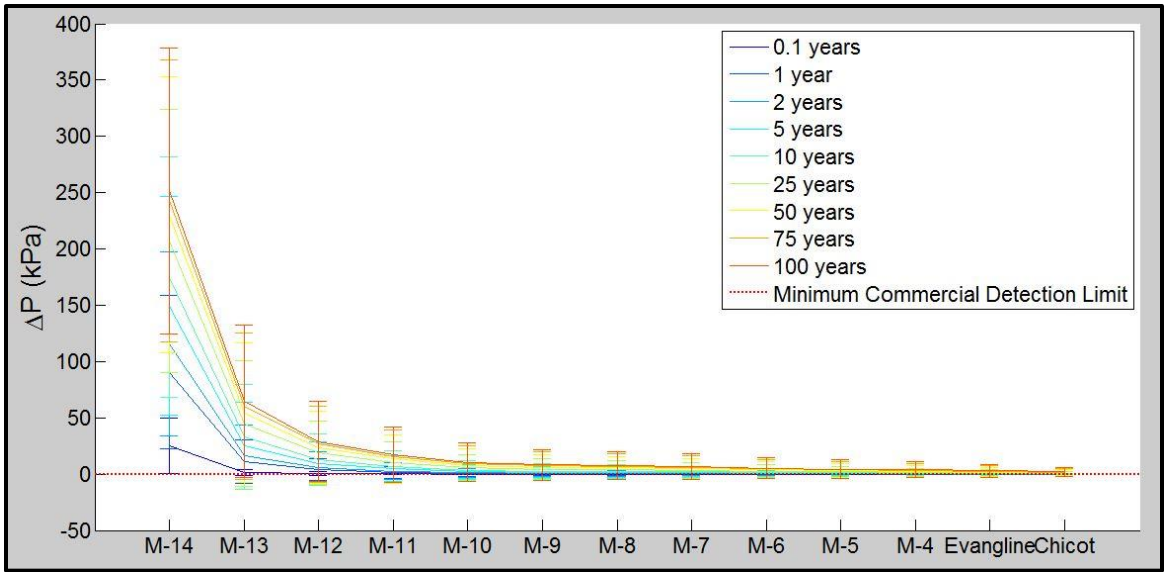

Figure 3.5: Mean (+/- one standard deviation) pressure change values for all AZMI formations, 100 years, 500 meters from the fault.

These results indicate that pressure signals will be strong enough in all AZMI formations for detection.

GEOCHEMICAL MODELING

In contrast to pressure monitoring results, modeled results of geochemical monitoring are more complex.. The model assume bromide (Br) is injected for the first 5000 days (13.7 years) of the 100 year simulation period. Results from AZMI formations, the M-14, M-12, M-8, and M-4, are highlighted, as they represent different levels of Br interaction and dispersion.

Starting in the M-14 formation, modeled Br values increase relatively quickly during the first 5000 days, especially at the wells closest to the fault (50 and 100 meters; Figure 3.6). From Figure 3.6, the largest mean Br value of any M-14 formation monitoring well is 8216 mg/l, occurring at the end of Br injection (5000 days). At 500 meters from the fault arrival time is longest and attenuates Br concentrations, with the

greatest value of 1082 mg/l at nearly 40 years. Cl/Br ratio values are found in Figure 3.7 over 100 years. Initial ratios measurements at 50-150 meters are lower (much lower at 50 meters) than the background ratio of 746, indicating Br intrusion within the first 500 days. Higher Br concentrations (Figure 3.6) lead to Cl/Br ratios below background levels in all distances from 50-500 meters in the first 30 years after simulated injection begins. The Cl/Br ratios eventual increase (Figure 3.7) occurs after the end of Br tracer injection, and because of subsequent plume dilution, and continuous injection of high concentration Cl brine throughout the remainder of the simulation period.

Figure 3.7 clearly demonstrates modeled Cl/Br ratio declines, but to understand this decline and when the greatest rates of declines occur temporally, the second derivative is calculated and plotted from Cl/Br ratio model results (Figure 3.8). Responses farther from the fault are seen by the delayed concavity change correlating to the greatest decline of the Cl/Br ratio. At a distance of 50 meters from the fault, the change in concavity is already observed within the first 500 days, and the slope recovers from its absolute minimum value (i.e., greatest rate of decline). The same behavior is seen for monitoring points in the M-14 formation 100 and 150 meters from the fault. Figure 3.9 shows absolute minimum second derivative values at: 1, 2.23, 3.75, 5.10, 6.49, 7.93, and 9.40 years for points increasing from 200 to 500 meters respectively. Minimum second derivatives are observed less than one year into the simulation at distances of 50 to 150 meters.

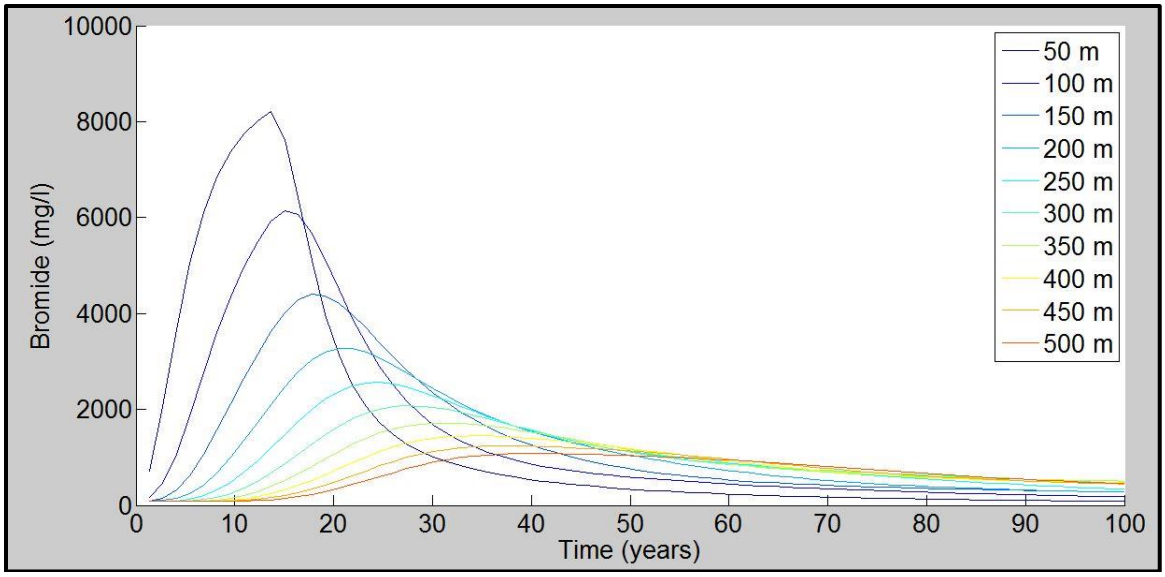

Figure 3.6: Mean bromide values at M-14 monitoring points from 50 to 500 meters laterally, over 100 years.

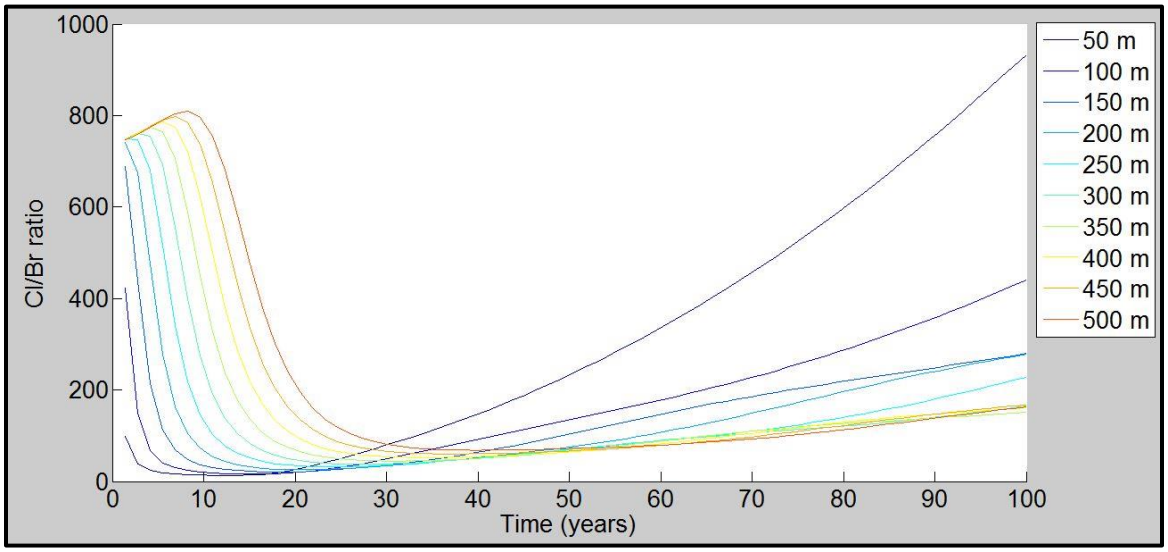

Figure 3.7: Cl/Br ratios in the M-14 formation, 100 year monitoring period.

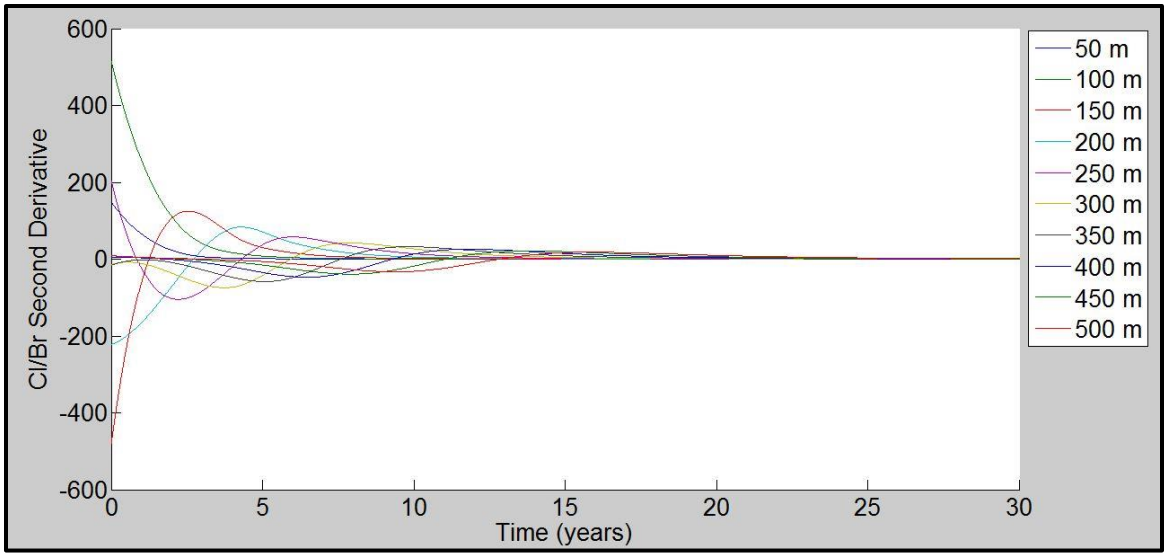

Figure 3.8: Second Derivative Cl/Br Values in the M-14 formation, 0-30 years.

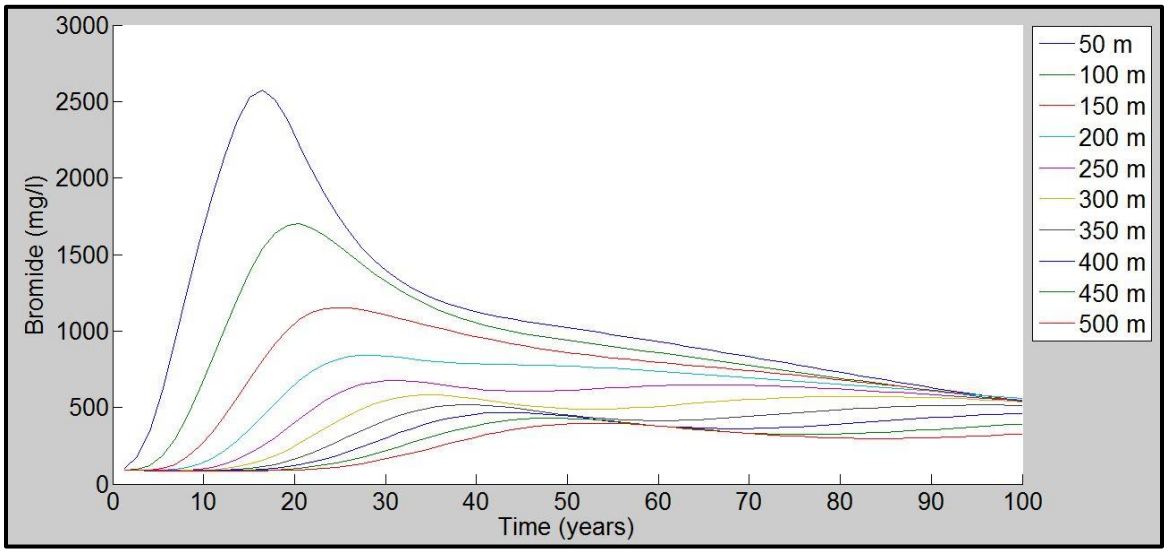

Figure 3.9: Mean Br concentrations in the M-12 formation, 100 year monitoring period.

This correlates to the strongest signal breakthroughs (i.e., absolute minimum second derivative value) at points closest to the fault, reinforcing the conclusion that monitoring points closest to the fault could yield the strongest signal changes. Decreases

in total concentrations of Br, a longer breakthrough time, and attenuated Cl/Br curves are all observed in the M-12 formation. The mean Br concentrations over 100 years in the M-12 formation range from 397 mg/l at 500 meters, to over 2570 mg/l at 50 meters (Figure 3.9). In the M-12 formation, attenuation of the Cl/Br signal is due to the increasing vertical distance away from the injection zone. For the closest observation point (i.e., 50 meters), decline in Cl/Br occurs slightly before 500 days in the simulation from 746 to 645 (Figure 3.10). The decline in the Cl/Br ratio in the M-12 formation is slower in comparison to the M-14 with the earliest occurrence at 6 years (at 50 meters), with monitoring points from 250-500 meters never falling below 100. Unlike the M-14 formation, recovery of the Cl/Br ratio in the M-12 formation from 350-500 meters is limited. Instead, an apparent second decrease is observed at these points after 50 years.

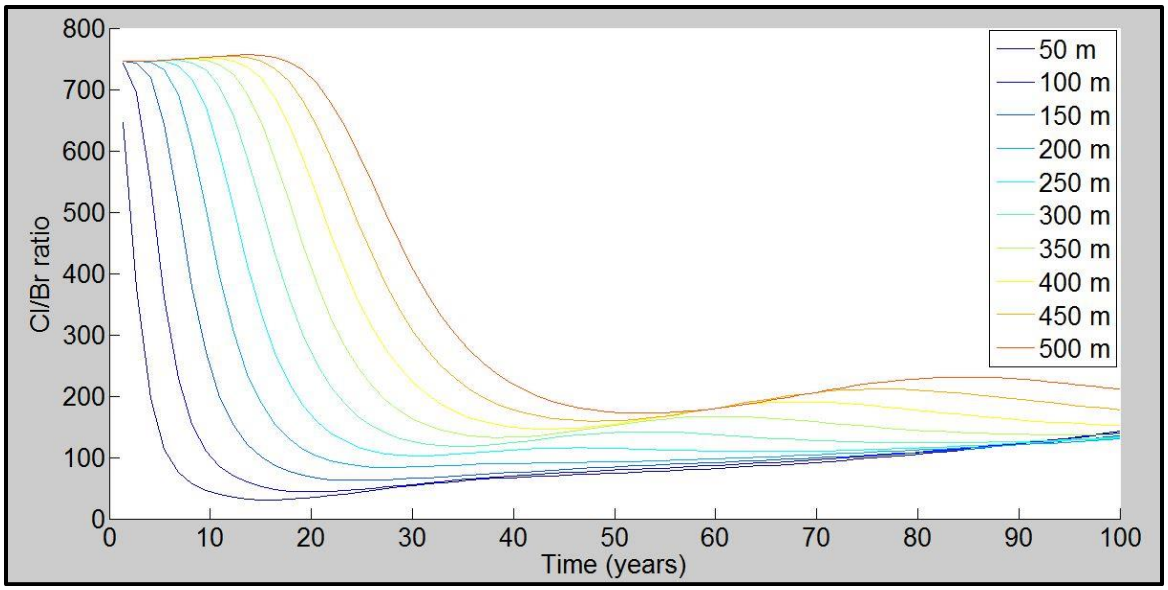

Figure 3.10: Cl/Br ratios in the M-12 formation, 100 year monitoring period.

The absolute minimum second derivative between the M-12 and M-14 formations is delayed with increasing vertical distance (Figure 3.11), from 1.34, 3.52, 5.59, 7.85, 10.09, 12.38, 14.72, 17.07, and 19.41 years for 100 - 500 meters lateral distance from the fault respectively. Similar to the M-14 formation, no absolute minimum second derivative value is obtained at 50 meters distance, primarily a function of close proximity of the simulated monitoring point to the fault.

Figure 3.12 shows the average Br concentrations in the M-8 formation over 100 years. In line with previously results, the M-8 concentrations are dampened, with lower maximum concentrations and longer breakthrough times. The highest Br concentration (i.e., 741 mg/l) occurrence is observed at 50 meters from the fault. As Figure 3.12 demonstrates, however, changes from background concentrations at 300 to 500 meters from the fault are minimal (e.g., 114 to 143 mg/l). These slight increases occur near the end of the modeling time period, indicating the expected maximum concentrations for the outermost monitoring wells would peak after 100 years.

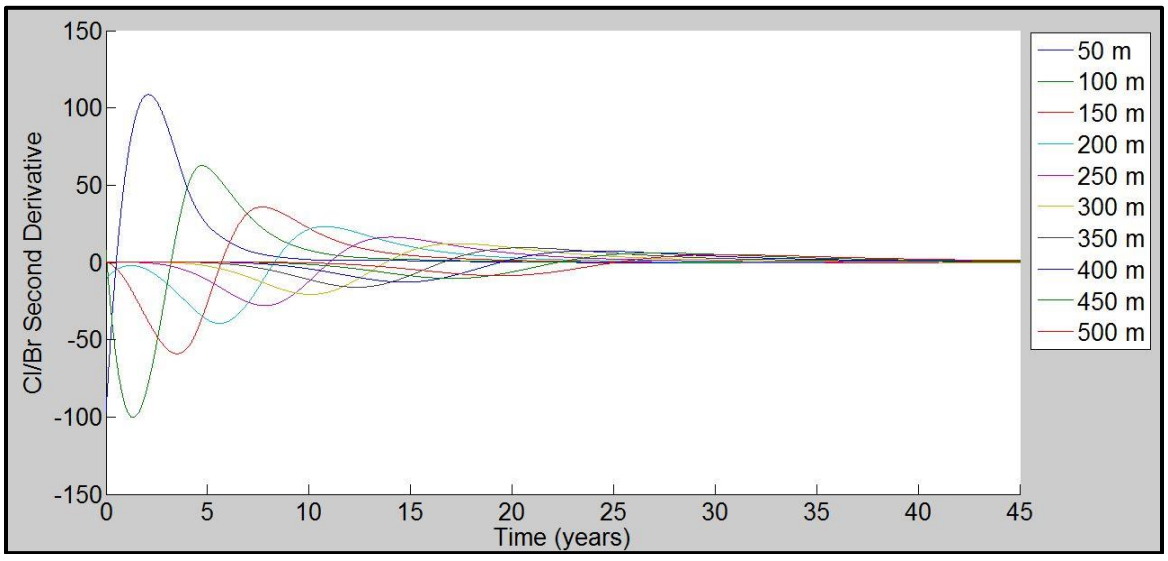

Figure 3.11: Second derivative Cl/Br values in the M-12 formation, 45 years.

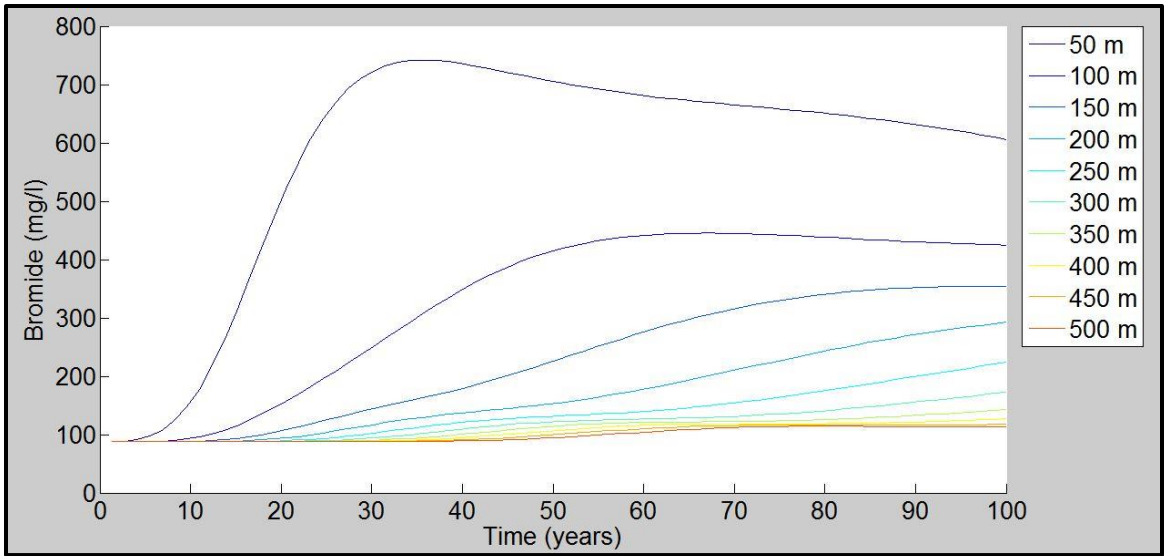

Figure 3.12: Mean Br concentrations in the M-8 formation, 100 year monitoring period.

Figure 3.13 presents mean Cl/Br ratios in the M-8 formation. Ratios observed from 300 to 500 meters to the fault continue declining throughout the 100 year monitoring time frame. In particular, the Cl/Br ratio at 500 meters does not begin to decrease until 40 years after the start of injection (and 27 years after the end of Br injection). The ratio observed at one monitoring point (at 50 meters) never falls below 100, unlike the M-14 and M-12 (Figures 3.8 and 3.11). Considering the Cl/Br ratio second derivative (Figure 3.14) the absolute minimum value continues attenuating compared to deeper formations. Interpolated greatest rates of decline for the M-8 formation are observed at: 3.78, 8.04, 12.54, 16.86, 21.16, 25.44, 29.7, 34.02, 38.34, and 42.67 years from 50 to 500 meters, respectively.

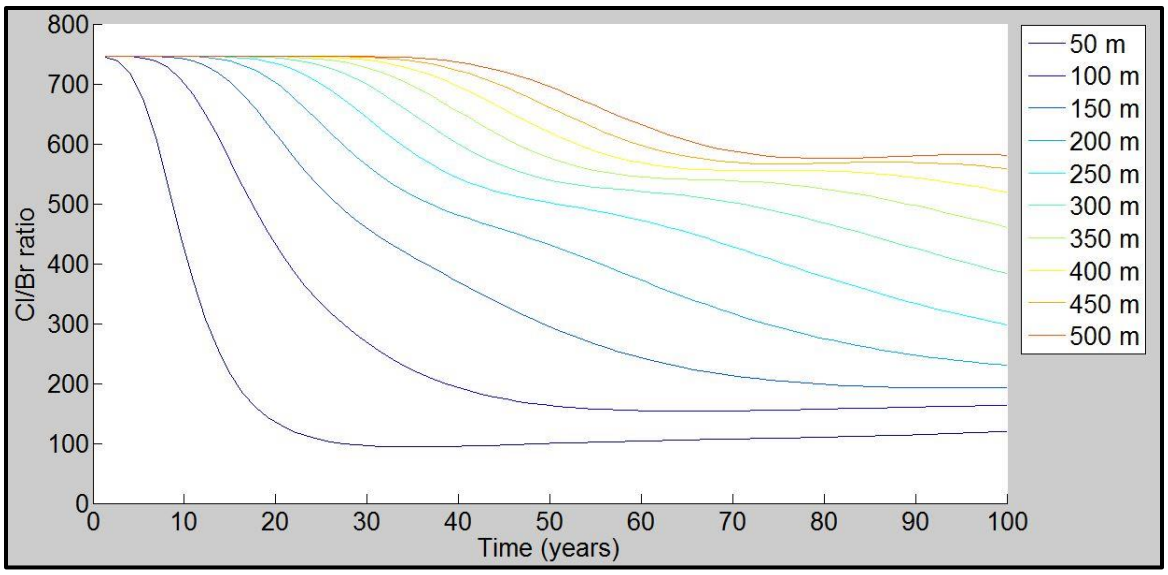

Figure 3.13: Cl/Br ratios in the M-8 formation, 100 year monitoring period.

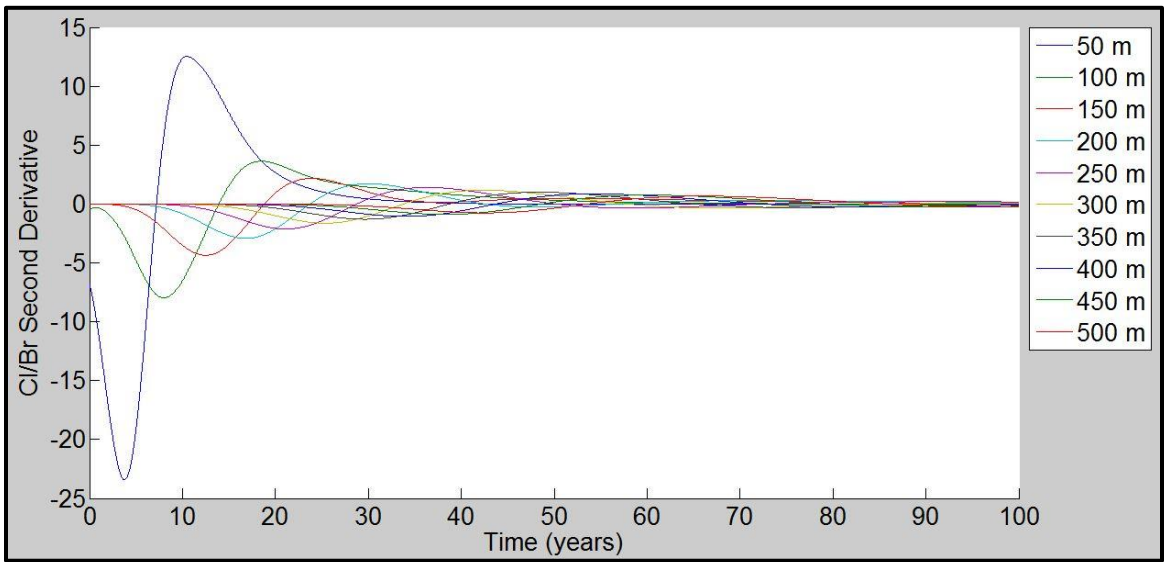

Figure 3.14: Second derivative Cl/Br values in the M-8 formation, 100 year monitoring period.

Furthermore, the M-4 formation shows a lack of Br intrusion in most instances until nearly 50 years after the start of the simulation. Average Br concentrations (Figure 3.15) are greatly attenuated when compared to deeper formations, with a maximum concentration of 262 mg/l at 50 meters. Cl/Br ratios indicate fluid migration at the closest monitoring points (i.e., 50 to 150 meters), but none of the decreases lead to Cl/Br ratio values below 100 (Figure 3.16).

Finally, ratios show no marked decrease with distances increasing from 250 to 500 meters anytime within the 100 year modeling period. The second derivative values for the M-4 formation from 50 to 250 meters are 16.01, 28.32, 48.76, 73.68, and 97.86 years respectively (Figure 3.17). The monitoring point at 300 meters begins to show an increase in the decline rate of the Cl/Br ratio, indicating initial Br breakthrough, but an absolute minimum value is not reached within the 100 year modeling period. Any wells beyond 350 meters register negligible changes in concavity, signifying that Br does not reach these wells within the 100 year modeling time frame.

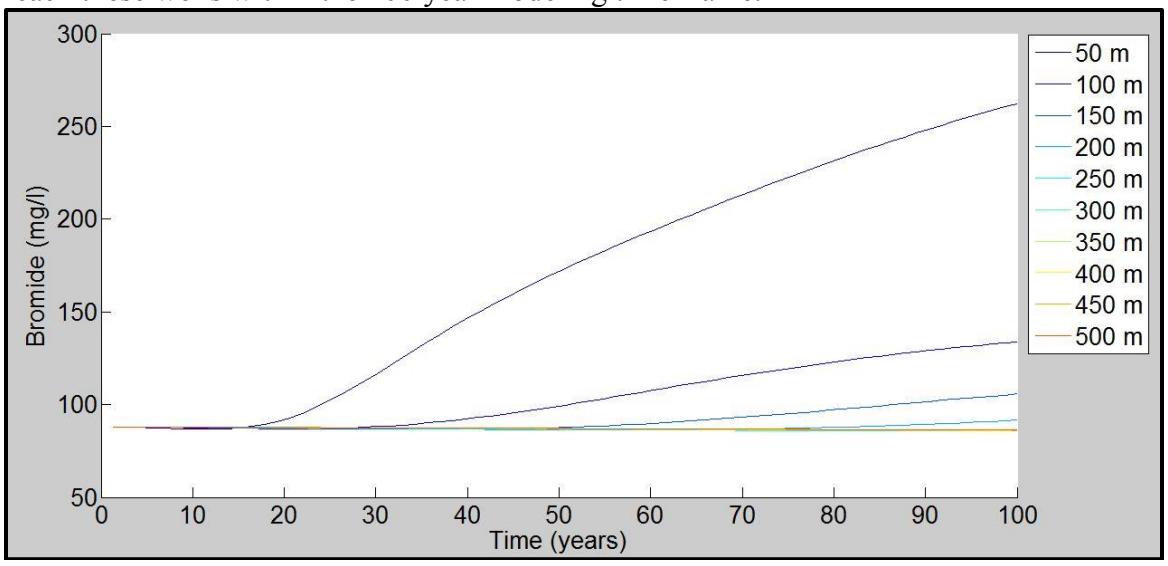

Figure 3.15: Mean Br concentrations in the M-4 formation, 100 year monitoring period.

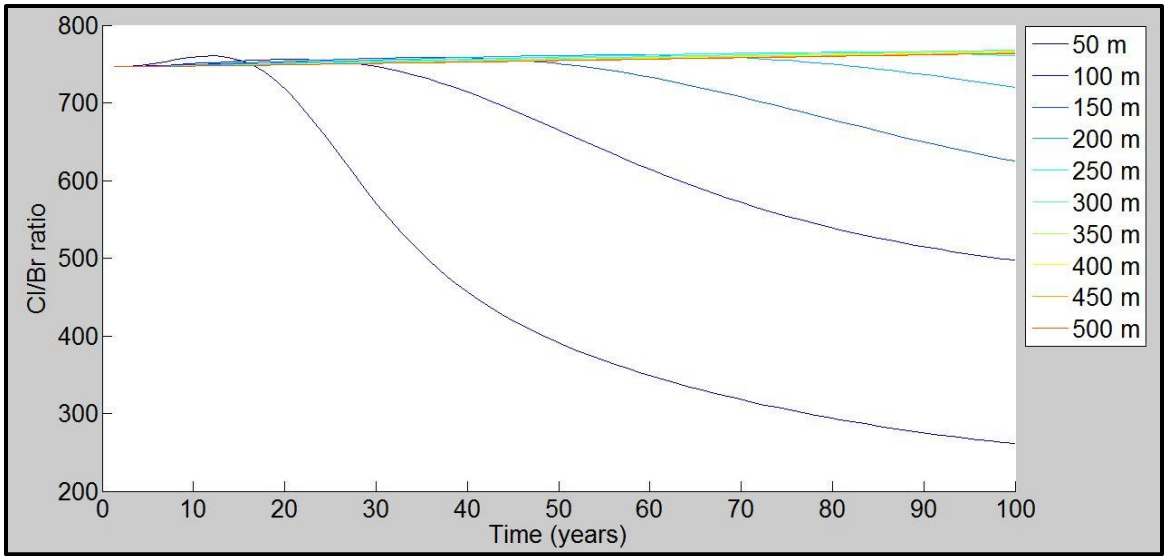

Figure 3.16: Cl/Br ratios in the M-4 formation, 100 year monitoring period.

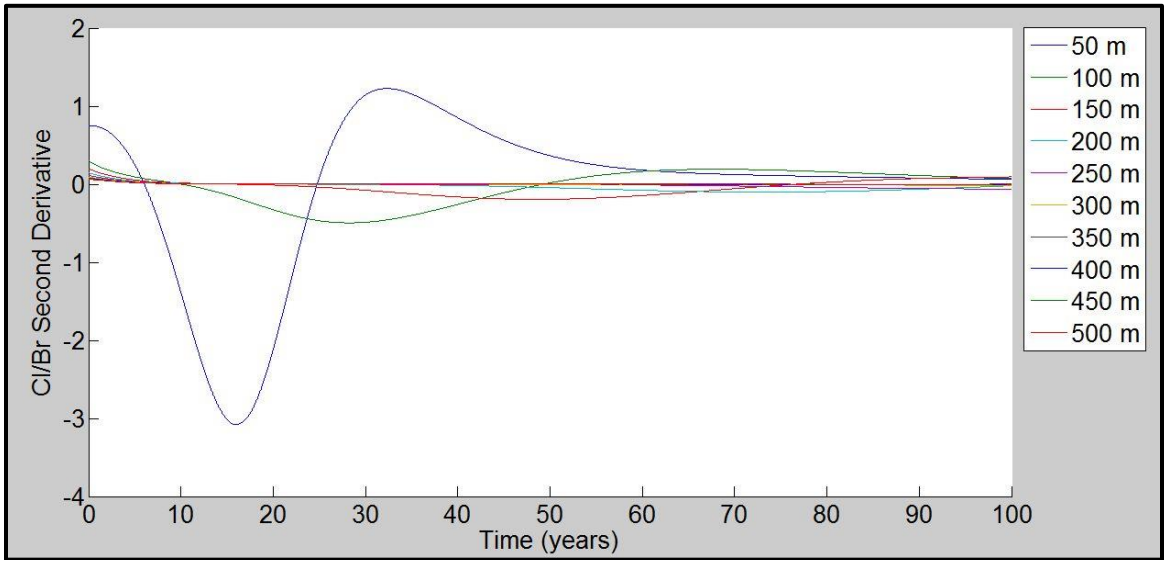

Figure 3.17: Second Derivative Cl/Br values in the M-4 formation, 100 year monitoring period.

Modeling results can be graphed to compare the potential use of geochemical monitoring in formations. Figure 3.18 shows the absolute minimum second derivative values for monitoring wells from 50 to 500 meters laterally in the M-14, M-12, M-10, M-

8, M-6, and M-4 formations. Every other monitoring formation is omitted for visualization purposes as modeling results in the M-7 to M-9 formations are spatially similar to one other. From Figure 3.18, Br migration rates are clearly attenuated from the deepest formation (i.e., M-14) to the top of the overburden (i.e., M-4). Geochemistry signals in the M-14 formation indicate absolute minimum values early in the 100 year monitoring period, especially in the 50 - 150 monitoring wells. The absolute minimum values increase between the M-14 and M-12 formations by an average of 7 years. Fluid migration signals continue to be attenuated in the M-10 and into the M-8 formations. While the strongest migration signals from the M-10 formation are predicted to occur earlier than in the M-8 formation through 220 meters laterally, past this lateral distance migration signals occur later in the M-10 than the shallower M-8 formation. This behavior is likely due to the relationship of formation permeabilities and vertical distance from the Frio sandstone. Initial breakthrough occurs sooner in the M-10 formation because of its closer proximity to the injection zone vertically. But the strongest signal occurs sooner at increasing lateral distances in the M-8 because of its higher assigned permeability (Table 2.3). By far the starkest change in inflection point rates occurs in the M-4, where modeled values are available only for lateral distances through 250 meters, quickly increasing to over 100 years.

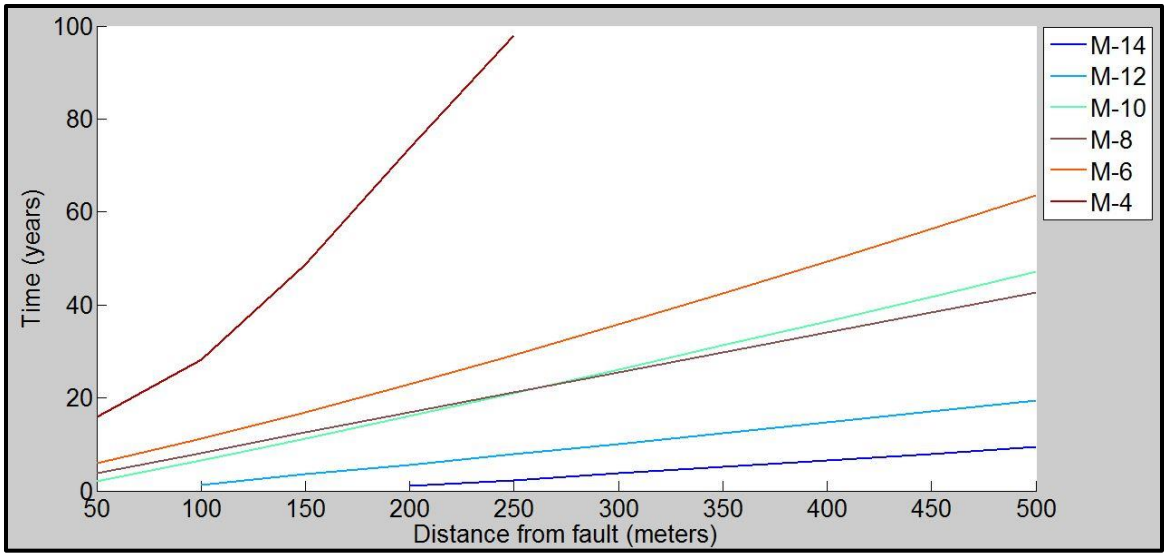

Figure 3.18: Second derivative geochemistry values for monitoring points 50 to 500 meters laterally, select AZMI formations.

COMPARISON OF MODELING RESULTS

Ultimately, comparing the modeling results of pressure and geochemistry can help determine the potential for either as a monitoring tool in the overburden. In this case, fluid migration signal time frames play an important role. In this section, a comparison of second derivative absolute minimum (i.e., maximum negative concavity) values between pressure and geochemistry is made, which indicate arrival of the strongest migration signals at monitoring wells at 100 and 500 meters away from the fault, respectively. Figure 3.19 and 3.20 shows second derivative values of pressure and geochemistry responses in the M-14 formation 100 and 500 meters from the fault. Pressure values at 100 meters rapidly approach, but never cross, the zero value during the 100 year time frame. Conversely, geochemistry values rapidly decline toward zero but never cross the zero threshold. At 500 meters, the pressure value is nearly identical to 100 meters in both

value and time occurrence at less than one year into the simulation (Figures 3.3 and 3.5). Geochemistry results at 500 meters differ from those observed at 100 meters, with an indication of arrival at 9.6 years after the start of the simulation. Based on a comparison of the graphs in Figures 3.19 and 3.20, both pressure and geochemistry have very early breakthroughs at 100 meters from the well. So early, in fact, that both signals register almost immediately after the beginning of the simulation. At 500 meters however, pressure concavity again indicate very rapid increases, while geochemistry has a delay of almost nine years until the absolute minimum second derivative value.

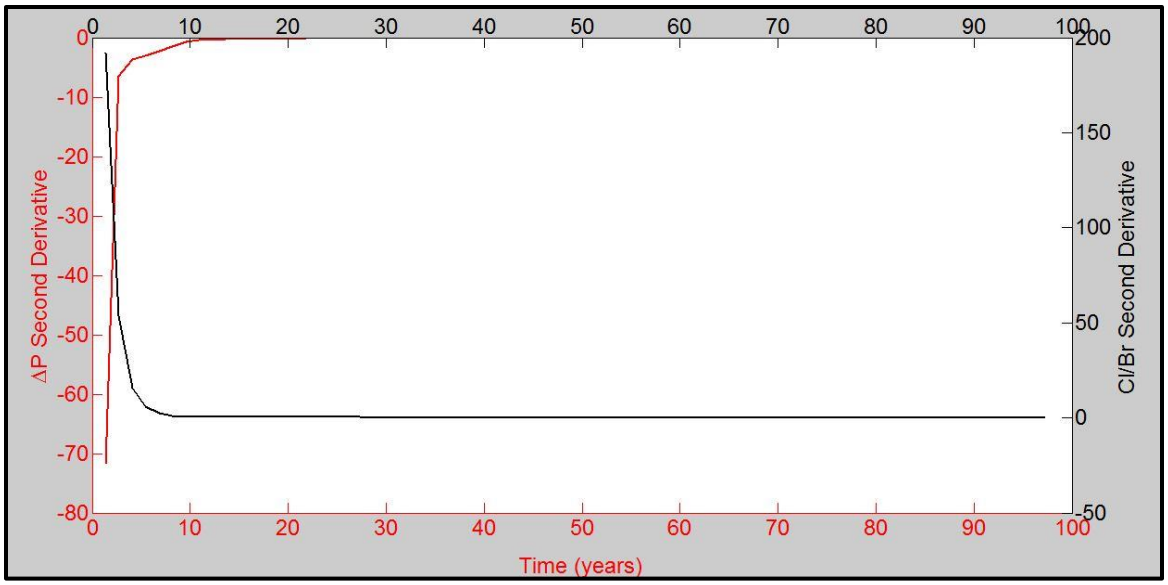

Figure 3.19: Second derivative pressure and geochemistry values in M-14 formation at 100 meters.

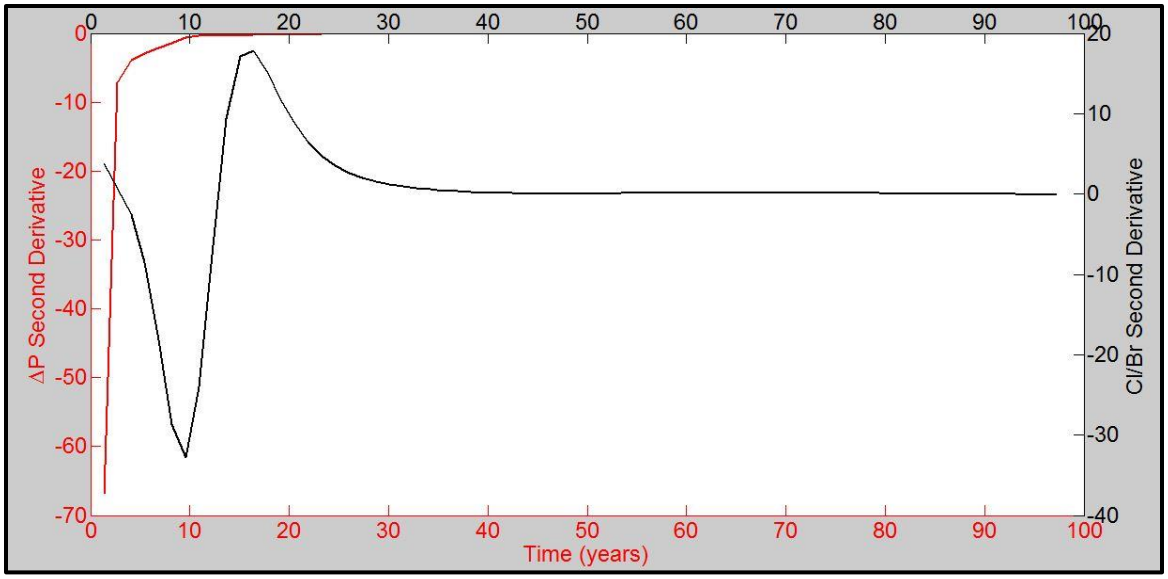

Figure 3.20: Second derivative pressure and geochemistry values in M-14 formation at 500 meters.

Results in the M-12 formation (Figure 3.21 and 3.22) demonstrate absolute minimum values for both pressure and geochemistry monitoring at the start of the simulation, similar to the M-14 results. However, Cl/Br ratios decline at a slightly smaller rate through the first seven years, leading to a slight delay in the clearest geochemistry signal, when compared to pressure. Moving laterally to 500 meters (Figure 3.22), while pressure monitoring again illustrates a relatively rapid decline of the second derivative (i.e., arrival of the pressure pulse) with an absolute minimum value at the start of the simulation, the geochemistry monitoring results indicate a further attenuated signal, with an absolute minimum value observed at 19.2 years. This is a nearly 20 year difference in the strongest geochemistry migration indicators for M-12 formation from the pressure signal.

In the shallower M-8 formation (Figure 3.23 and 3.24), the difference in the strongest migration signals continues to widen between pressure and geochemistry. At a

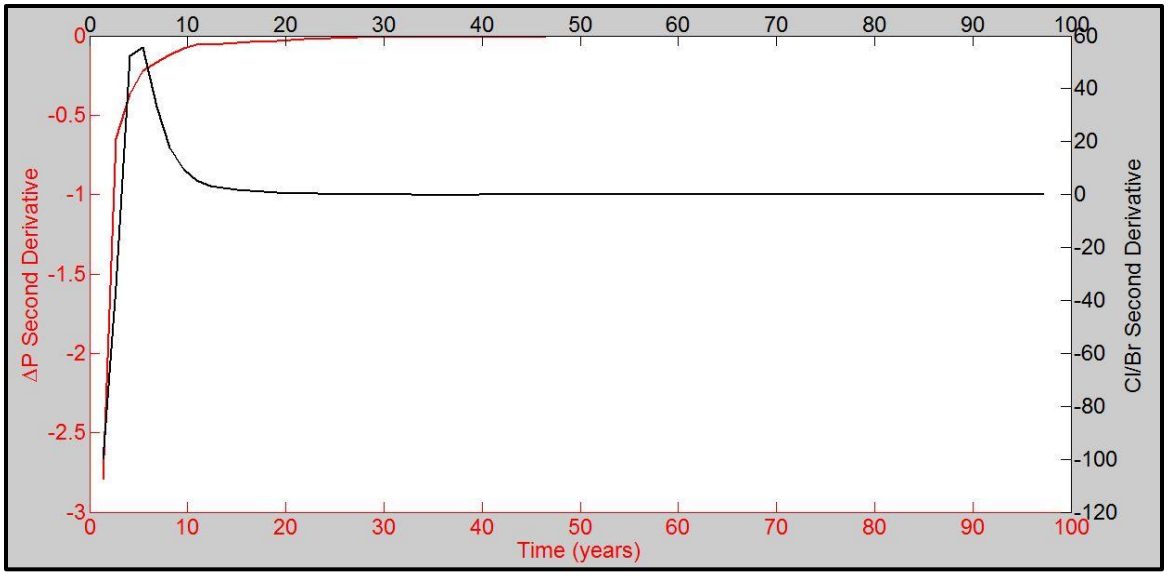

Figure 3.21: Second derivative values for pressure and geochemistry in M-12 formation at 100 meters.

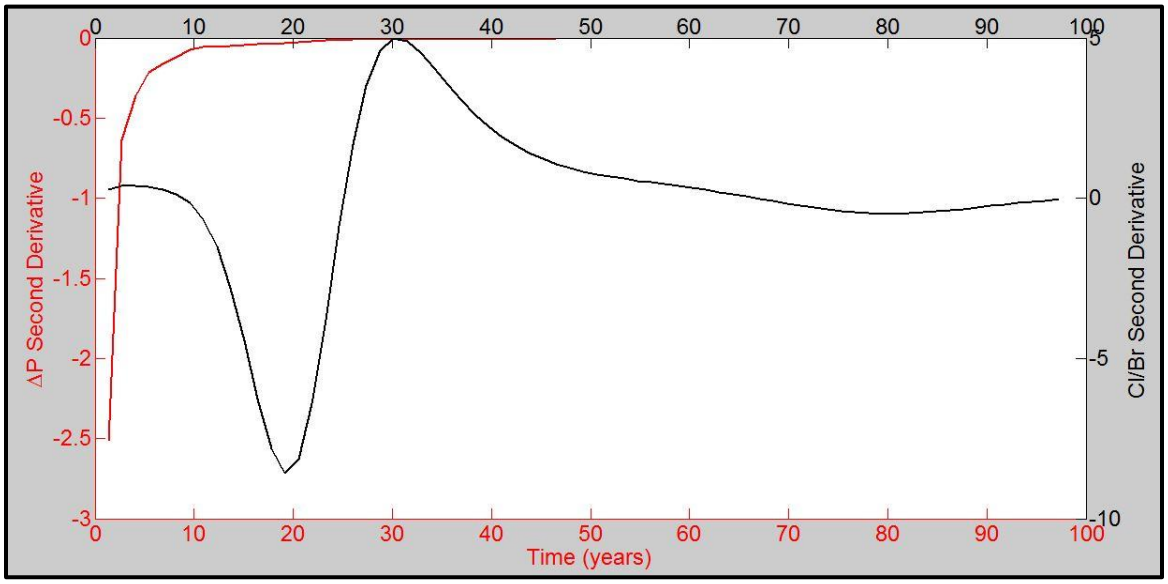

Figure 3.22: second derivative values for pressure and geochemistry in M-12 formation at 500 meters.

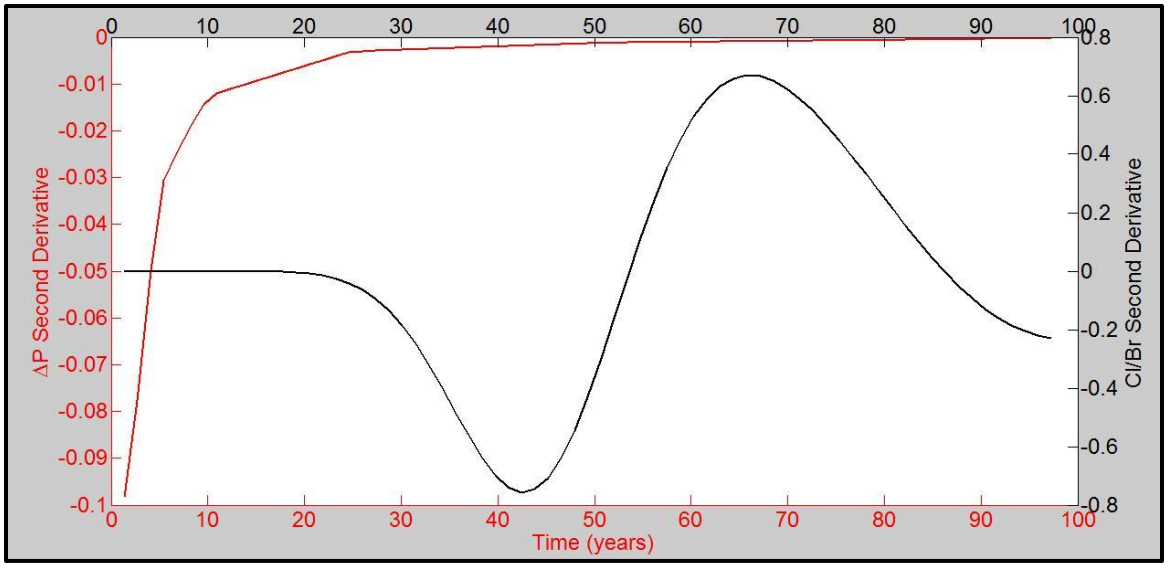

Figure 3.23: Second derivative values for pressure and geochemistry in M-8 Formation at 100 meters.

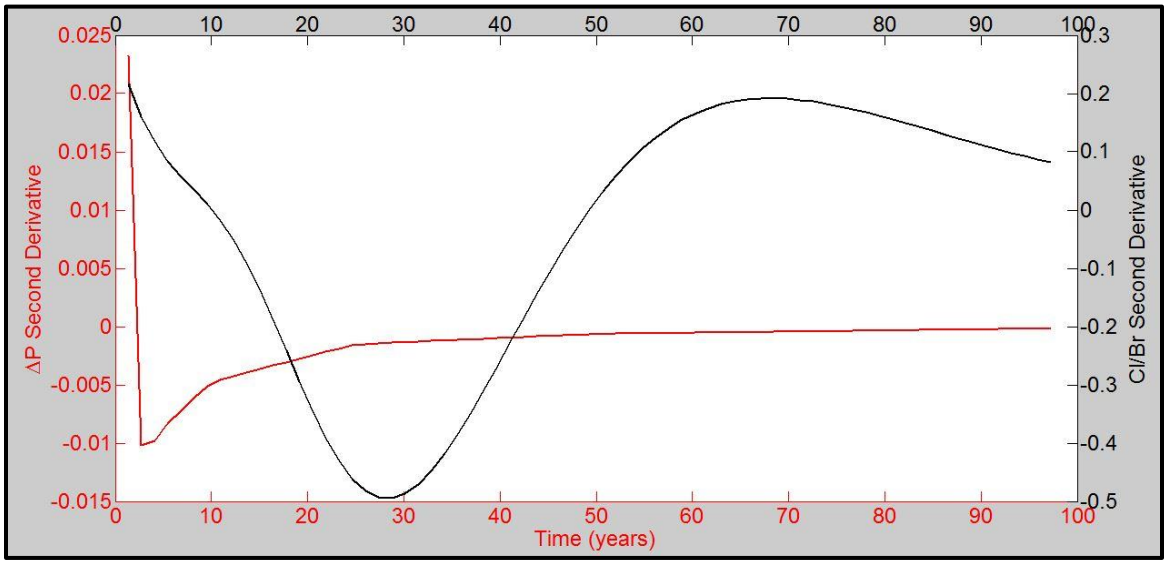

Figure 3.24: Second derivative values for pressure and geochemistry in M-8 Formation at 500 meters.

lateral distance of 100 meters from the fault, arrival of the pressure response occurs near the beginning of the simulation, while the geochemistry signal did not reach the monitoring point until 8.2 years. At 500 meters from the fault, pressure signal mirrors the

same pattern seen at 100 meters, while the geochemistry signal does not reach the monitoring point until nearly 43 years after the start of injection. Thus, a difference of around 35 years in fluid migration detection was estimated using geochemistry signal breakthrough in the M-8 formation as fault distance increases to 500 meters.

At a distance of 100 meters from the fault in the M-4 formation (Figure 3.25), the pressure signal is slightly delayed from deeper AZMI formation by around two years. However, the pressure signal still occurs much earlier than the geochemistry signal, approximately 28 years into the simulation. At 500 meters from the fault (Figure 3.26), pressure is further attenuated to around 3.5 years after the start of the simulation, while geochemistry monitoring demonstrates no discernible decline in the Cl/Br rate, due to the fact that Br never migrates 500 meters within the M-4 during the 100 year monitoring time frame.

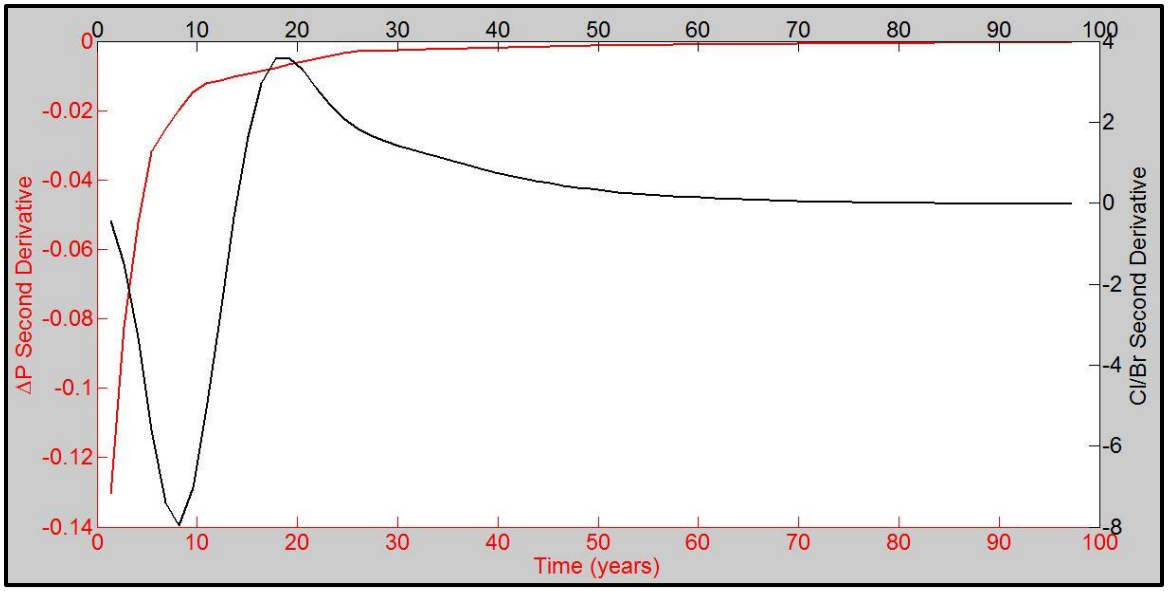

Figure 3.25: Second derivative values for pressure and geochemistry in M-4 formation at 100 meters.

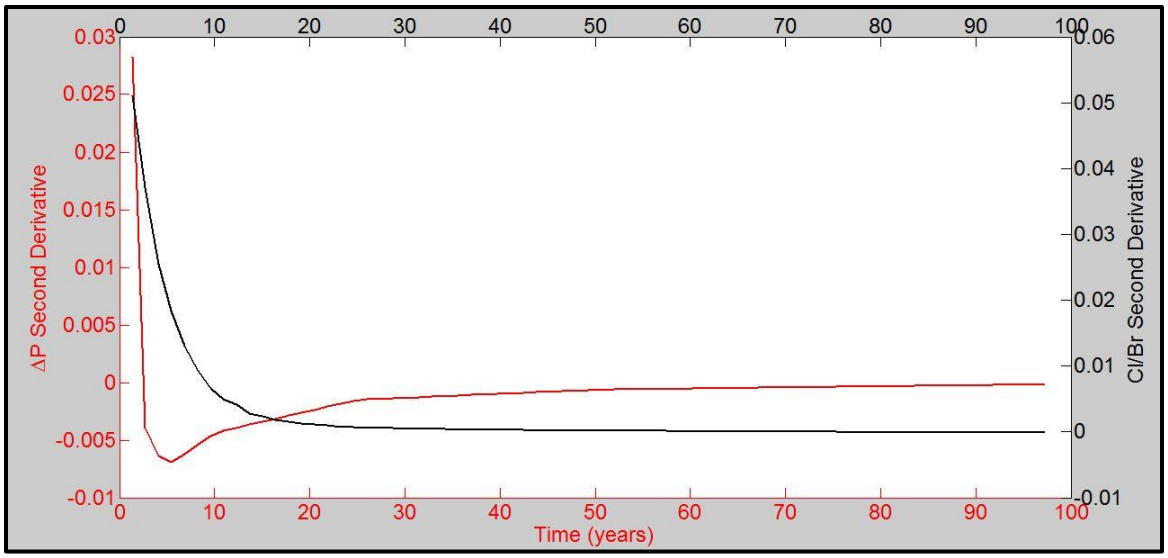

Figure 3.26: Second derivative values for pressure and geochemistry in M-4 formation at 500 meters.

Chapter 4: Discussion

In almost all modeling results discussed in Chapter 3 (Comparison of Modeling Results), pressure signal breakthrough occurs more quickly than geochemistry in the M-sand formations above the Frio injection zone. With these observations, the question arises: how can these results be applied to monitoring approaches at CCUS sites? Additionally, what are some Federal and State regulatory considerations of this work?

PRESSURE MODELING

Pressure modeling results from 100, 300, and 500 meters laterally from the fault in each respective AZMI formation have similar results in both magnitude and timing. However, these pressure values attenuate with an increase in lateral distance from 100 to 500 meters, ranging from differences of around 10 kPa in the M-14, to $4x10^{-4}$ kPa in the M-4 formation. Through the use of the mean ΔP (+/- one standard deviation) values (e.g., Figures 3.3 and 3.5) we can determine: which AZMI formations have simulated pressure changes above the gauge MDL, and which of these values falls outside of the range of uncertainty (i.e., standard deviation) from the Monte Carlo sampling process.

All AZMI formations, including the Evangeline and Chicot aquifers, have pressure signal breakthroughs above MDL for nearly the entire 100 year modeling period. Initial pressure signals in formations shallower than the M-9 are below MDL at 0.1 years, but these values quickly rise above detection limits shortly after one year. Only the shallowest formation, the Chicot Aquifer, have simulated values below MDL past one year, persisting for up to five years. Accounting for the uncertainty from the Monte Carlo simulations (i.e., Figures 3.3 to 3.5), the M-14 formation is the only monitoring formation, at any lateral distance, that has pressure signal values above MDL. However, while pressure values estimated in only the deepest monitoring formation are outside the

range of uncertainty, all formations have values above MDL at all lateral distances, increasing the chances that detection can occur. Visually, these results are summarized in Figure 4.1. Ultimately, the use of pressure as a monitoring tool in the subsurface could prove most practical in those formations where the maximum rate of change in modeled pressure occurs early, and creates pressure changes above the MDL. Such AZMI formations, from M-4 to the M-14 in the model domain, are categorized here as "primary" candidate pressure monitoring formations (Figure 4.1).

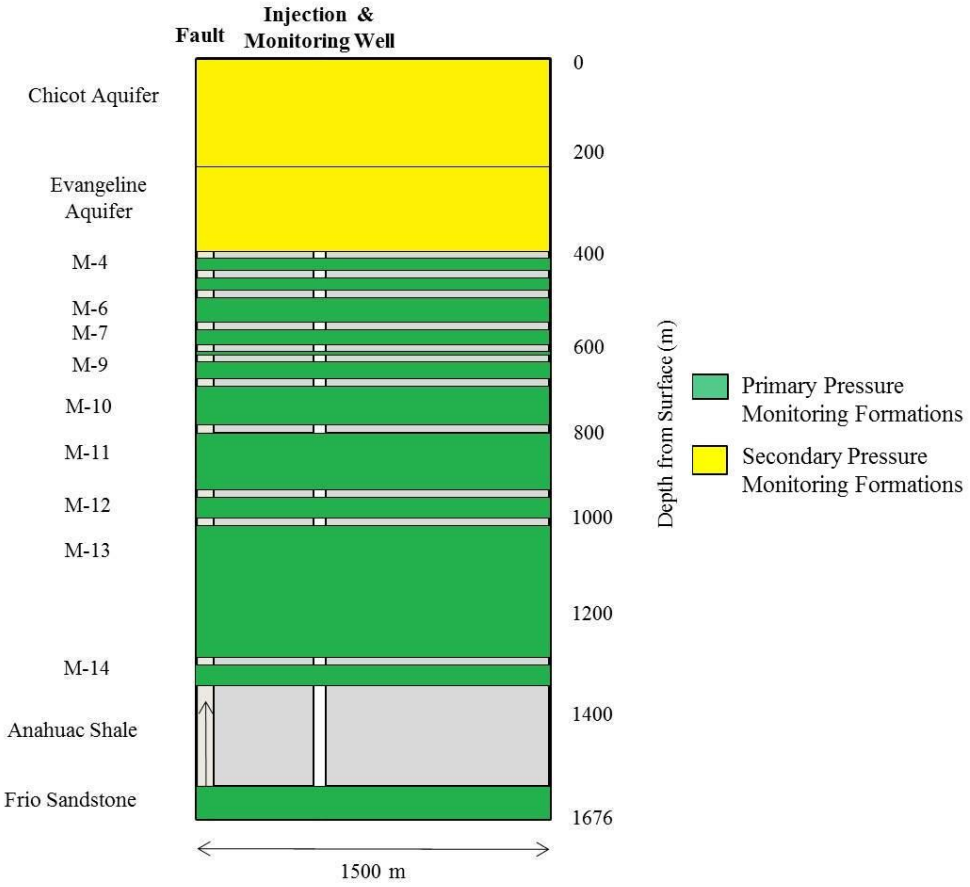

Figure 4.1: Pressure monitoring AZMI formation recommendations based on analytical modeling results, Hastings Field.

While pressure signals in the shallowest (i.e., Evangeline and Chicot) aquifers also rise above MDL, they did so after one to five years after the models starts. With more potentially viable options in deeper AZMI formations based on breakthrough times, the Evangeline and Chicot aquifers are categorized as "secondary" candidates for pressure monitoring. Results for all M-formations indicate that their use for pressure monitoring could prove practical in nearly all instances. Only in the shallowest formations is the time delay significant for a breakthrough pressure signal.

GEOCHEMISTRY MODELING

These simulated geochemistry results rely on parameters for signal detection other than pressure, and they yield different interpretations. Rather than using a minimum gauge detection limit, the results are interpreted best using the chloride/bromide (Cl/Br) ratio, in which bromide is introduced into the injected fluid as a tracer. The arrival of the Br tracer in each modeled AZMI formation is strongly affected by the hydraulic parameters that control the flow of groundwater and subsequent tracer transport, as in Chapter 2, Equation 2.2. Here, holding flow rate, density, and gravity constant, the only major change affecting the transport rate of groundwater in the model domain is hydraulic conductivity, based on the permeability distribution value for each AZMI formation. With formation permeability values ranging across orders of magnitude between injection, confining, and AZMI formations, subsequent transport of Br tracer also ranges widely.

Injecting Br for the first 5000 days of the simulation helps to show the attenuation of groundwater flow and ultimately the sensitivity of tracer migration in each AZMI formation. Figures 3.6, 3.9, and 3.12 show that attenuation occurs quickly after Br injection ceases. Table 4.1 summarizes all geochemistry signal breakthroughs (in years),

which are then adapted spatially in Figure 4.2. Table 4.1 values are indicative of how the spatial relationship of permeability affects Br transport in each AZMI formation (Figure 4.2). Comparing the breakthrough times of geochemical signals in each formation, while the deepest AZMI formations may provide earlier breakthrough times (i.e., < 30 years), the signals in the M-14 and M-12 formation occur more quickly than in the M-13 formation. This is largely based on the hydraulic parameters and the thickness of the M-13 formation; both M-13 properties directly attenuate the geochemical signal breakthrough when compared to the M-14 and M-12 formations. Signals in certain shallower formation (e.g., M-8, M-10) can take nearly 50 years to propagate 500 meters laterally. In contrast, the M-7 and M-9 formations have shorter signal breakthrough times, with a maximum arrival time of 40 years the simulation starts, at the farthest monitoring points in each formation. The shallowest M-formations have the greatest length of time associated with Br migration, in some instances never reaching the given monitoring point (i.e., M-4 300 meters and farther with respect to the fault).

Distance from modeled fault (m)	M-14	M-13	M-12	M-11	M-10	M-9	M-8	M-7	M-6	M-5	M-4
50				1.94	2.11	4.13	3.78	5.06	5.92	9.42	16.01
100		2.01	1.34	4.80	6.45	7.74	8.04	8.28	11.23	21.21	28.32
150		4.59	3.52	7.96	11.26	11.46	12.54	11.78	16.98	39.76	48.76
200	1.00	7.91	5.59	11.34	16.14	15.21	16.86	15.32	22.93	60.55	73.68
250	2.23	12.03	7.85	14.92	21.09	19.06	21.16	18.98	29.22	82.31	97.86
300	3.75	16.79	10.09	18.61	26.15	22.98	25.44	22.75	35.78	N/A	N/A
350	5.10	22.04	12.38	22.36	31.27	26.99	29.70	26.61	42.46	N/A	N/A
400	6.49	27.71	14.72	26.24	36.50	31.14	34.02	30.60	49.41	N/A	N/A
450	7.93	33.68	17.07	30.21	41.79	35.35	38.34	34.68	56.44	N/A	N/A
500	9.40	39.82	19.41	34.21	47.11	39.59	42.67	38.81	63.52	N/A	N/A

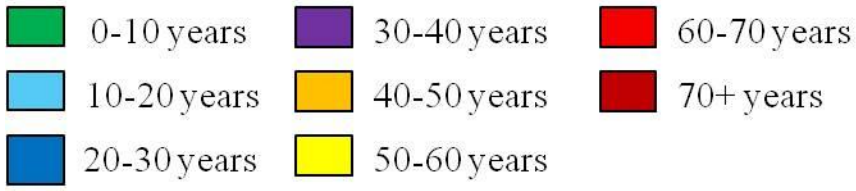

Table 4.1: Geochemistry signal breakthrough times for all AZMI formations, in years. Colors correspond to Figure 4.2. N/A indicates no signal breakthrough.

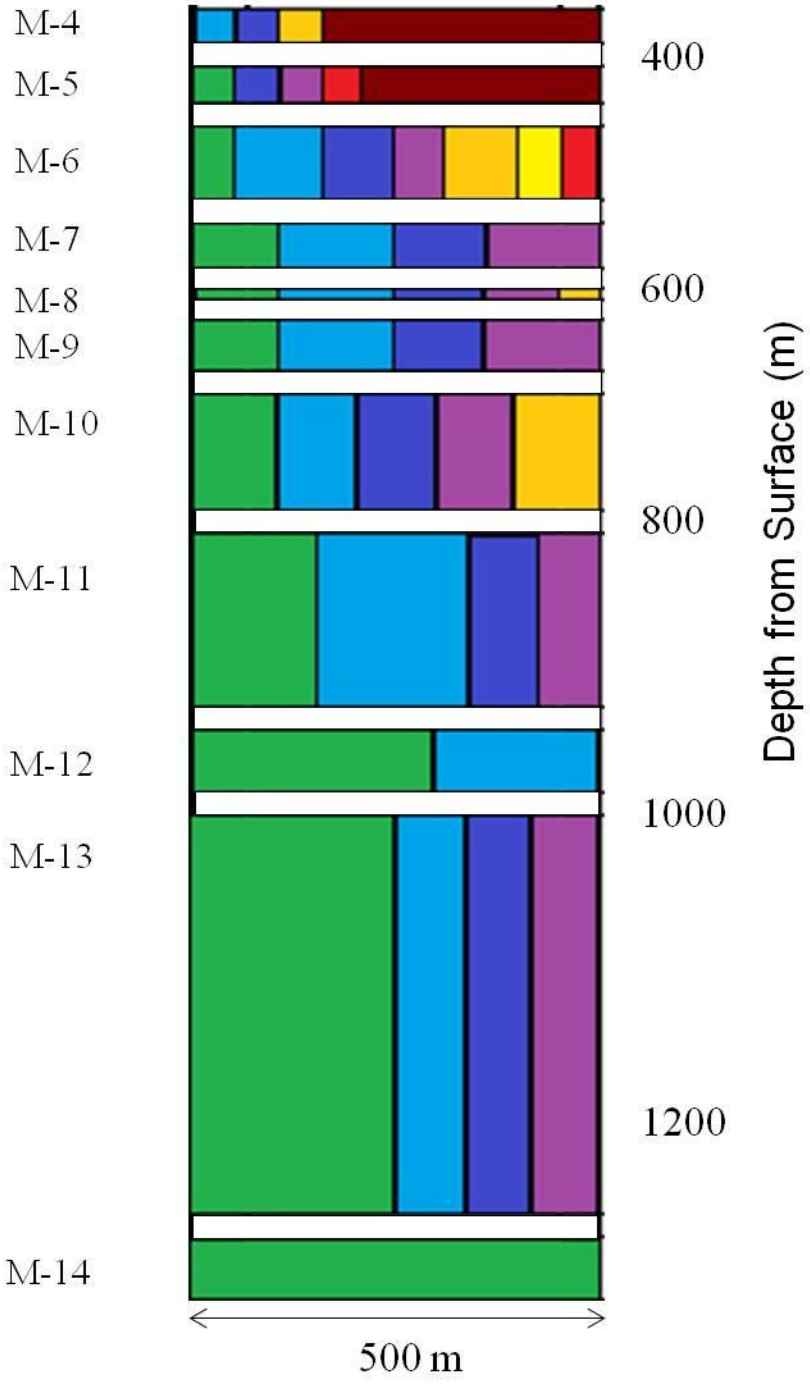

Figure 4.2: Geochemistry signal breakthrough adapted from Table 4.1, shown 0-500 meters laterally from the modeled fault. Refer to Table 4.1 for color scale.

These results raise the question, what could be the significance for using geochemical signal breakthroughs at commercial oil fields? Mature oil and gas fields generally have production lives extended by 15-25 years from CO_2 EOR activities (NETL, 2010). Based on these simulated results, geochemical signal breakthroughs in AZMI formations that are greater than 25 years may not prove useful for monitoring during EOR injection and/or production, especially in shallower AZMI formations (e.g., M-5, M-6, M-7) and at the farthest lateral distances from the possible fault.

Rather, these monitoring locations could be more useful for different applications separate from CO_2 EOR, such as GS projects with a Class VI permit where post-injection site care and long term liability considerations are required (e.g., periods > 50 years). Modeling results demonstrate that the best opportunities for GS operators to observe an arrival signal would be at the closest proximity to the suspected migration source both vertically and spatially. This includes the M-14 formation at all lateral distances, the M-13 formation distances 300 meters and closer, and the M-12 formation at all distances from the possible fault. Additionally, geochemistry monitoring could have limited use in shallower formations where hydraulic parameters are conducive for wider distributions of the monitored fluid.

MONITORING COMPARISON

Ultimately, the major goal from this thesis is to compare simulated pressure and geochemistry signals using a standard analysis metric and determine which method could be more appropriate as a monitoring tool at a field such as Hastings. Integrating the modeling results and discussion from above for each monitoring tool, we know that pressure proves to be a quicker metric of migration than geochemistry, but by how much?

	Strongest signal, 100 meters from modeled fault		Strongest signal, 500 meters from modeled fault	
AZMI Formation (Depth, m)	**ΔP Signal (years)**	**Cl/Br Signal (years)**	**ΔP Signal (years)**	**Cl/Br Signal (years)**
M-4 (412)	2.5	28.32	2.5	> 100
M-5 (457)	< 2	21.21	2	> 100
M-6 (516)	< 2	11.23	2	63.52
M-7 (583)	< 2	8.28	< 2	38.81
M-8 (639)	< 2	8.04	< 2	42.67
M-9 (652)	< 2	7.74	< 1	39.59
M-10 (703)	< 1	6.45	< 1	47.11
M-11 (803)	< 1	4.80	< 1	34.21
M-12 (945)	< 1	<1	< 1	19.41
M-13 (1018)	< 1	2.01	< 1	39.82
M-14 (1328)	< 1	< 1	< 1	9.4

Table 4.2: Pressure and geochemistry signal breakthrough times, 100 and 500 meters from the modeled fault.

Adapting results from Chapter 3 (Comparisons of Modeling Results) for all AZMI formations show that pressure can be a more appropriate monitoring tool for fluid migration detection than geochemistry (Table 4.2). Similar geochemical and pressure

signal breakthroughs are observed in only the M-14, M-13, and M-12 formations at 100 meters from the possible fault.

At 500 meters from the possible fault, however, the contrast in modeled geochemical and pressure signal breakthrough times becomes substantial, with an arrival difference at a minimum of nine years. Similar to observed attenuation in both magnitude and timing at shallower depths, the difference between pressure and geochemistry signals increases with shallower depths. The maximum breakthrough time for pressure is roughly 2.5 years, occurring in the M-4 formation at all lateral distances. In contrast, geochemistry signal breakthrough in the M-4 formation occurs at 28.32 years at 100 meters. No breakthrough signal is observed at 500 meters from the possible fault during the 100 year modeling period.

Overall, maximizing the chances of detecting fluid migration at Hastings Field through a groundwater monitoring program should emphasize physical parameters (i.e., pressure) first, and could include geochemical parameters as a secondary parameter to monitor for possible migration pathways. A pressure signal, at any depth, is predicted to occur within a relatively short amount of time (< 2.5 years after the start of injection), and will also be high enough for practical measurement. For geochemistry, while the magnitude of the geochemical signal is predicted to be high enough at all depths to be measured by current laboratory standards, the relatively long signal breakthrough time eliminates almost all AZMI formations (at this site) from serious consideration for geochemical monitoring. Only the M-14 (at all lateral distances from the fault), and the M-13 and M-12 formations, 100 meters and closer from the possible fault, may prove useful for geochemistry monitoring.

Practically speaking, unnecessary amounts of time and money may be needed to identify, construct, and/or repurpose a monitoring well that is located less than 100

meters from a possible migration pathway to maximize a geochemical monitoring program. These modeling results show that pressure can provide greater flexibility for monitoring well placement in a suitable AZMI formation. Importantly though, a comprehensive data set collected before designing an MVA program is necessary to understand the limits of monitoring systems discussed within this chapter. If an owner or operator can anticipate the difficulties associated with locating a well near a suspected migration pathway (i.e., from historical records or data), they can account for this difficulty by tailoring any MVA program toward the most flexible monitoring parameters to maximize fluid migration detection.

REGULATORY CONSIDERATIONS

Current UIC regulations for GS require the integration of direct and indirect monitoring techniques (e.g., pressure and geochemistry) at depths varying from the injection zone (i.e., deep) to the shallow subsurface (i.e., vadose zone) to protect USDWs (40 CFR 146.90). While 40 CFR 146.90 requires a number of different monitoring techniques, the frequency which these monitoring activities must be performed is flexible, based in large part on baseline characterization of the site, with the ability to update the frequency based on operational data.

In contrast to GS, traditional EOR operations follow UIC Class II requirements, where monitoring requirements primarily focus on well integrity, and monitoring operational parameters (e.g., injection pressure, cumulative volume, injected fluid composition) on a monthly basis or as determined by data characteristics (40 CFR 146.23). EOR operators (if using CO_2) must also report the mass of CO_2 received prior to injection to USEPA under Subpart UU of the Mandatory GHG Reporting Rule (40 CFR 98.470-472). CO_2 EOR operators in Texas voluntarily seeking to certify the amount of

anthropogenic CO_2 incidentally stored must do so through a monitoring and testing plan (Texas Administrative Code Title 16, Part 1, Chapter 5, Subchapter C, §5.305). Such certification monitoring plans define how the operator intends to: quantify anthropogenic CO_2 separated, injected, and entrained amounts, sample injection zone and AZMI formation fluids, and measure operational parameters. §5.305 provides flexibility for how often an owner or operator must undertake this monitoring, largely based on data collected prior to and during operations.

Based on the aforementioned requirements, the Class II and Class VI programs serve inherently different operations towards the same goal of protecting USDWs; Class II monitoring programs emphasize well and operational integrity, while Class VI monitoring programs emphasize a more comprehensive approach using both direct and indirect methods. Should this be the case? Should monitoring networks emphasize a comprehensive approach with many parameters, or should a monitoring network focus on maximizing detection of a migration signal through a concentrated number of more reliable monitoring tools?

Answers to such questions could become imperative if industrial carbon capture becomes incentivized in the United States through a financial or trading mechanism. Active research into monitoring techniques that can assure captured emissions retainment, such as this thesis and the MVA research program being developed at Hastings, helps determine effective monitoring network development in the future. For example, such assurance might be needed by an industry selling captured CO_2, as part of their demonstration of Best Available Control Technology (e.g., optimized technology for a specific industry to maximize emissions reduction) under the Clean Air Act.

Consistent with current regulatory structures, the Hastings monitoring program can focus on monitoring well installation in nearly all available AZMI formations above the Frio, especially those closest to a possible fluid migration pathway, and above the Anahuac shale (i.e., M-12 to M-14; Figure 4.3). In almost all cases, pressure is predicted to be a more effective metric for detecting groundwater migration into formations above the injection zone because the early breakthrough of pressure occurs concurrently with, or before, geochemistry signals (Table 4.2). This shorter time frame means that migration

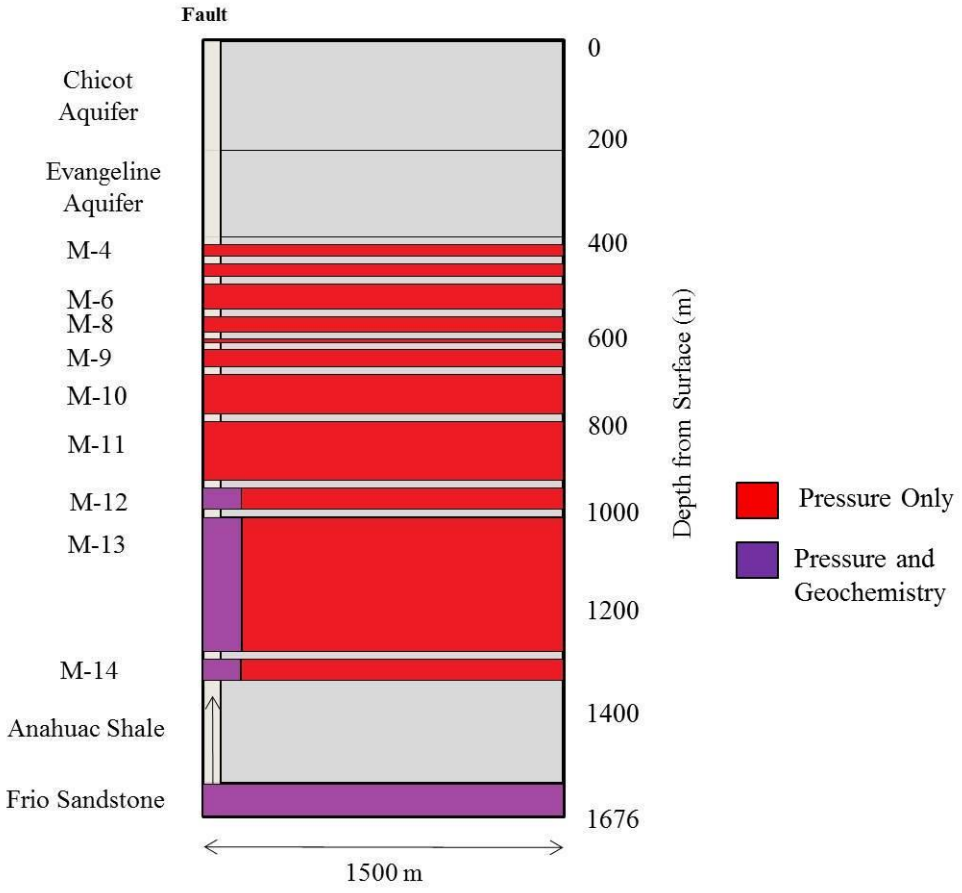

Figure 4.3: Recommended operations monitoring locations for pressure and geochemistry, based on modeling results from Chapter 3.

signals could be detected sooner, allowing the owner or operator to adjust field operations accordingly to meet project goals and regulatory requirements.

Under most scenarios, requiring additional geochemical monitoring could place burdens on owners or operators with little to no additional benefit towards protecting USDWs. However, geochemical analyses could prove useful: 1) both vertically and laterally close to a suspected migration pathway (i.e., M-12 to M-14 formation; Figure 4.3), 2) if a permit requires longer monitoring time frames (i.e., >25 years) such as GS projects (Figure 4.4), and 3) where the pressure signal breakthrough would be difficult to detect due to engineering noise (e.g., injection, production activities) occurring within the same monitoring formation. However, pressure signals are predicted to occur sooner than geochemistry signals, and should still be emphasized as a primary indicator of fluid migration.

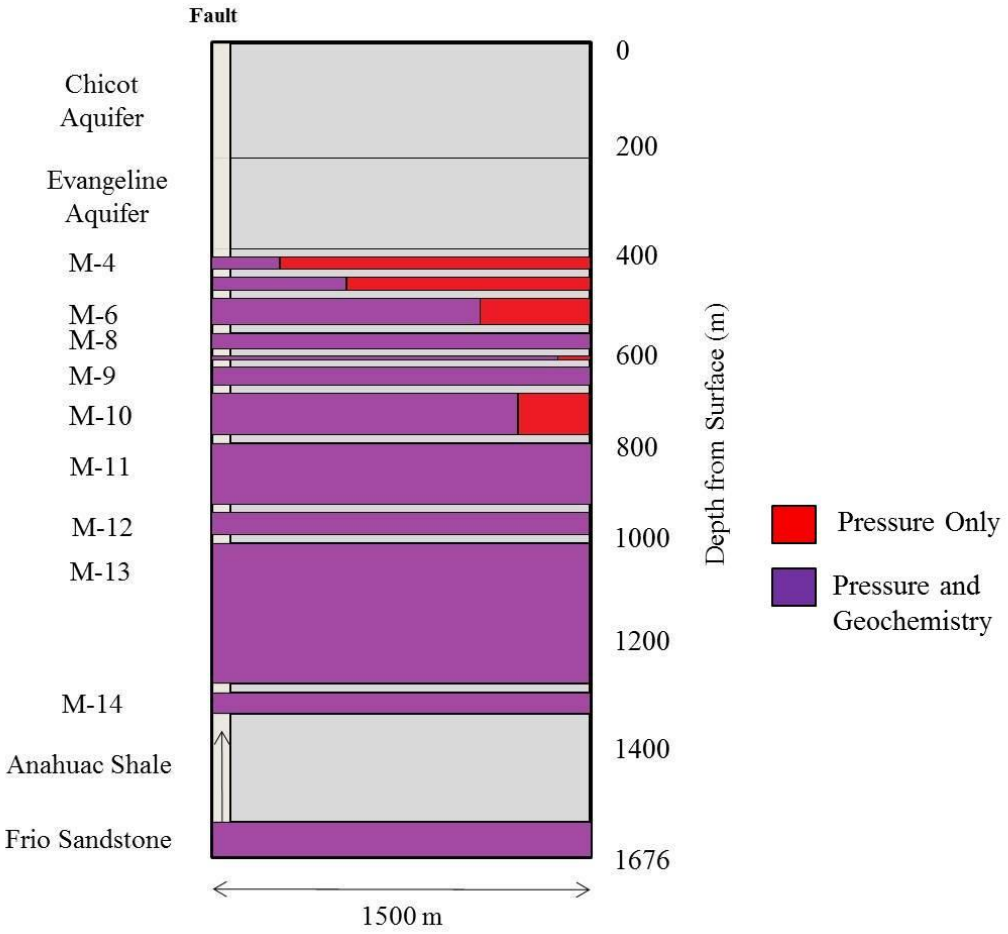

Figure 4.4: Recommended long-term (i.e., > 25 years) monitoring locations for pressure and geochemistry, based on modeling results from Chapter 3.

BROADER IMPLICATIONS

How do these results relate to broader monitoring contexts involving different types of fields and/or migration pathways? A wealth of research is available involving the complexities of brine/CO_2/fresh water interaction both at depth and in shallow groundwater aquifers. Brine migration rates and flow volumes into shallower aquifers are controlled by a number of factors including the type of migration pathway available (e.g., diffusive migration through caprocks, through open wellbores, or along well annulus damage zones; Cihan et al., 2013); injection rates and resulting pressure changes in the

injection zone (Zhou and Birkholzer, 2011); and the density (resulting from the salinity) of migrating brines (Nicot et al., 2009; Oldenburg and Rinaldi, 2011).

The modeling results from this thesis work demonstrate the sensitivity of brine migration into overlying aquifers to changes in monitoring formation hydraulic parameters, as well as suspected migration pathway properties (i.e., width, vertical permeability). In contrast to Hastings, other areas of the US and even different areas along the Gulf Coast of Texas may have ideal storage reservoirs, but little to no permeable sandstones above the injection zone. This would have consequences for developing an AZMI monitoring program because 1) fewer formations are candidates for above-zone monitoring leading to less flexibility in network setup, and 2) fluid or pressure migration up a conducive pathway at a site lacking multiple sandstone formations would not be attenuated, causing signals to travel further, and have higher magnitudes. While potentially advantageous for monitoring signal purposes, a stronger signal at shallower depths may also pose a greater threat to USDWs.

Regardless of the injection activity type, proper site characterization is crucial towards identifying ideal candidate sites not only favorable for injection/production activities, but for monitoring as well. The characterization should include (but is not limited to) critical analyses of the regional structure, stratigraphy, hydrogeology, presence (or lack) of wells on site, as well as a detailed understanding of the planned operations. Collecting and analyzing such datasets allows an operator to tailor a monitoring network for the site characteristics and suit the project's needs, whether those needs are primarily regulatory or operations-based or a combination of focuses. If site flaws are missed during characterization, a properly set up monitoring program can provide early signal detection so adverse migration can be minimized. In the case of these thesis results, pressure is predicted to be a better metric for the Hastings MVA program;

geochemistry has potentially limited applications, but only in areas where pressure signals could also effectively indicate leakage.

A major goal of this thesis is to evaluate the sensitivity of pressure and geochemistry parameters to detect single-phase fluid migration up a theorized migration pathway. This work does not take into account multi-phase fluid dynamics (e.g., CO_2); such dynamics (e.g., buoyancy, compressibility, total volume of CO_2) can play a important role in determining signal strength. Additionally, multi-phase system flow interactions require solving for complex physics falling outside the capabilities of either model used in this thesis. To approach a solution that includes these variables, a modeling domain would need to account for migration path and formation heterogeneities (e.g., anisotropic flow), as well as the connection of the migration pathway to the rock matrix. Geochemical tracers used consisted of a conservative Cl/Br ratio examination, rather than using CO_2, or a potential reaction product from CO_2-rock-water interactions. While not accounting for these more complicated physical and geochemical considerations, the simplification to understanding brine interactions and significant chemical constituents of brine (Cl and Br) allows for accomplishing the desired thesis goal efficiently: parameter temporal distribution and sensitivity at a modeled geologic domain.

Chapter 5: Conclusions

This thesis work tests the sensitivity of using pressure and aqueous geochemical monitoring as fluid migration detection methods by systematically varying specific reservoir and theorized migration pathway properties used as input to analytical and numerical models over a 100 year monitoring period. Results highlight the advantages of proper site characterization of the strata above the confining system before any monitoring network design. Monitoring for multiple parameters alone is not enough to assume timely detection of a migration signal. Instead, it must be informed by thorough site characterization prior to operation.

Should there be out-of-zone migration, changes in subsurface pressure at the Hastings site are predicted to be detectable at all monitoring depths above the Anahuac Shale, especially in the deepest AZMI formations, (e.g., M-14, M-13, and M-12), from depths of 945 to 1374 meters. Not only are all modeled pressure values above MDL in all AZMI formations, signals all rise above MDL levels no later than five years after the onset of the models, with values exceeding MDL in a majority of AZMI formations (i.e., excluding the Evangeline and Chicot aquifers) less than one year after the onset of the models. This difference in modeled pressure signal breakthrough defines the deeper M-sands as “primary” and the shallower Evangeline and Chicot as “secondary” candidate formations for pressure monitoring. Geochemical monitoring signals, through the modeled injection of a bromide tracer and measured with a chloride/bromide ratio, is predicted to be strongest in the deepest AZMI formations. However, the strongest modeled geochemical signals in these formations occur within 100 meters of the possible fault; as distances from the possible fault increased, the strongest signals are delayed, in some instances by decades compared to pressure signals.

While the Class VI regulations emphasize geochemistry as a primary indicator of migrating groundwater or CO_2, the modeled breakthrough times demonstrated in this research show that such emphasis is not appropriate for most operational instances (Figure 4.3). Rather, an emphasis should be placed on physical parameters (e.g., pressure) use. Given enough time, geochemical signals could eventually breakthrough at varying time frames, depending on distance of the monitoring well from the possible fluid migration zone. Understanding this relationship and limitations, both types of monitoring could be used together under select circumstances to satisfy regulatory requirements (i.e., Class VI) for long term monitoring (i.e., > 50 years) at shallower depths (Figure 4.4). This type of robust monitoring approach could maximize the probability of migration signal detection over required time frames, the goal for any monitoring program.

Regulators should work with owners or operators of CCUS projects to create permits that stress the best site-specific monitoring approach that falls under respective regulatory criteria. No single tool or method will be optimal for all scenarios. Ultimately, a site-specific monitoring program will instill public confidence in the regulatory community and the oil and gas industry, and protect drinking water resources for generations to come.

Appendix A: Hastings Water Sample Results

Sample ID	Location	Latitude	Longitude	Comment	Date	Watertype	Sample Depth, m (ft)	pH
Well 1904	West Hastings	29.51588	-95.25269	"pond well" - very muddy	4/1/12	Na-HCO_3	50.72 (166.4)	
Ford A Battery	East Hastings	29.51187	-95.24343	O'Day drilling pulled pipe and pump	3/15/12	Na-Cl	0.00	7.86
Well 1608	West Hastings	29.51582	-95.26494	O'Day drilling installed tap	3/16/12	Na-HCO_3	0.00	7.64
Near 3706	West Hastings	29.51056	-95.25919			HCO_3	51.11 (167.7)	7.97
CO_2 Facility	West Hastings	29.50084	-95.26322	O'Day drilling installed tap	3/15/12	Na-HCO_3-Cl	0.00	7.78
Cannon #7	West Hastings	29.49772	-95.25059	opened valve with wrench	3/13/12	Na-HCO_3	0.00	7.83
Autry	West Hastings	29.48445	-95.25175	O'Day drilling pulled pipe and pump, and jetted	3/14/12	Cl-HCO_3	49.16 (161.3)	8.18
Chance	West Hastings	29.48891	-95.25972	O'Day drilling pulled pipe and pump, and jetted	3/14/12	Na-HCO_3	49.38 (162)	7.83
Kidd 9	East Hastings	29.49894	-95.23453	O'Day drilling jetted well to clear plug at ~70 ft	4/1/12	Na-HCO_3	46.66 (153.1)	7.01
Oil Sales	East Hastings	29.5044	-95.230148	strong hydrocarbon odor in freshwater	3/14/12	Na-HCO_3-Cl	0.00	7.83
M-14 brine	West Hastings	3185235.7'*	626330.5'*	From Well #4831	7/5/12	Na-Cl	1463.04 (4800)	6.13
		*TX 4204 Nad27						

APPENDIX A CONTINUED

Sample ID	Temperature (°C)	Conductivity (µs/cm)	Dissolved Oxygen	CH_4	^{13}C	^{2}H	^{18}O	Alkalinity	Ag
Well 1904		586.00		0.20	-12.60			423	-0.00032
Ford A Battery	24.60	599.00	0.32	0.55	-13.00				-0.00028
Well 1608	23.24	558.00	0.76	0.34	-12.40			422	-0.00028
Near 3706	23.81	956.00	1.26		-12.80			411	
CO_2 Facility	24.32	900.00	0.38	0.13	-12.80			412	-0.00030
Cannon #7	20.36	760.00	4.66		-13.50			414	-0.00031
Autry	25.70	1471.00	0.30	0.17	-12.60			516	
Chance	24.41	561.00	0.28	0.41	-12.90			417	-0.00030
Kidd 9	24.25	756.00	0.31		-3.20			512	-0.00031
Oil Sales	25.36	620.00	0.41	0.20	-11.90			406	-0.00030
M-14 brine	53.10	100000.00						151.60	-0.01119
Sample ID	**Al**	**As**	**B**	**Ba**	**Br**	**Ca**	**Cd**	**Cl**	**Cr**
Well 1904	0.00213	0.00074	0.12572		0.20322	24.98454	-0.00001	41.23742	0.00019
Ford A Battery	0.00122	0.00078	0.15789		0.10798	14.10257	-0.00001	42.91256	0.00008
Well 1608	0.00397	0.00042	0.10640		0.11638	22.03012	0.00000	34.32586	0.00024
Near 3706									
CO_2 Facility	0.00241	0.00008	0.18782		0.35167	22.51065	0.00000	143.32021	0.00003
Cannon #7	0.00493	0.00031	0.15917			28.33226	0.00000		0.00005
Autry								348.66064	
Chance	0.00533	-0.00007	0.13885		0.16000	12.99563	0.00000	42.55755	0.00023
Kidd 9	0.00404	0.00750	0.36127		0.17900	9.61247	0.00003		0.00072
Oil Sales	0.00596	-0.00012	0.12531		0.23000	26.96338	0.00000	57.73993	0.00011
M-14 brine	-2.82489	-0.00065	22.58223	67.01026	68.48408	2658.49927	-0.01215	59288.51104	-0.05253

APPENDIX A CONTINUED

Sample ID	Cu	Co	F	Fe	HCO_3	K	Li	Mg	Mn
Well 1904	0.00138	0.00012	0.54000	0.04517	423	1.90187	0.01545	6.71013	0.06755
Ford A Battery	0.00180	0.00013	0.55423	0.06884		1.06958	0.01444	6.02367	0.04060
Well 1608	0.00146	0.00017	0.50664	0.07548	422	1.24610	0.01548	7.49951	0.09046
Near 3706					411				
CO_2 Facility	0.00257	0.00012	0.85542	0.03107	412	1.40422	0.01646	5.82745	0.03416
Cannon #7	0.00210	0.00016		0.05497	414			6.69107	0.08522
Autry			0.63994		516	2.10404	0.02858		
Chance	0.00201	0.00016	0.57666	0.05503	417	1.15697	0.01532	5.28621	0.05120
Kidd 9	0.00381	0.00017		0.00399	512			5.29008	0.02359
Oil Sales	0.00169	0.00018	0.52208	0.02544	406	1.57262	0.01578	7.57841	0.03277
M-14 brine	-5.26750	0.00315	0.38005	18.50090	151.6	134.68536	2.45840	571.13966	1.49143
Sample ID	**Mo**	**Na**	**Ni**	**NO_3**	**NO_2**	**Pb**	**PO_4**	**Rb**	**Sb**
Well 1904	0.00320	98.31218	0.00069	2.51068	0	0.00000	0.00000	0.00082	0.00010
Ford A Battery	0.00355	123.47141	0.00039	0	0	0.00014	0.12113	0.00037	0.00004
Well 1608	0.00201	97.80427	0.00060	0	0	0.00066	0.17087	0.00050	0.00003
Near 3706									
CO_2 Facility	0.00038	172.88499	0.00052	0	0	0.00092	0.03650	0.00078	0.00002
Cannon #7	0.00136	135.49785	0.00089			0.00020		0.00087	0.00001
Autry				0	0		0		
Chance	0.00306	128.96804	0.00158	0	0	0.00018	0	0.00040	0.00003
Kidd 9	0.01299	168.03215	0.00072			0.00023		0.00080	0.00029
Oil Sales	0.00035	108.09242	0.00069	0	0	0.00090	0.05686	0.00097	0.00001
M-14 brine	0.00340	33698.46910	-0.15221	0	0	-0.02974	0	0.27996	-0.03185

APPENDIX A CONTINUED

Sample ID	Se	Si	SO_4	Total Dissolved Solids (mg/l)	Sr	Th	Ti	Tl	U
Well 1904	0.00011	8.39758	3.92337	392.62	0.27909	0	0.00196	-0.00004	0.00015
Ford A Battery	-0.00003	6.47830	0	401.33	0.16805	0	0.00158	-0.00003	0.00000
Well 1608	-0.00001	7.36836	1.74153	373.86	0.23430	0	0.00193	-0.00003	0.00000
Near 3706				640.52					
CO_2 Facility	0.00002	9.76484	0	603	0.36872	0	0.00223	-0.00002	0.00000
Cannon #7	-0.00003	9.76886		509.2	0.44998	0	0.00234	-0.00003	0.00000
Autry			0	985.57					
Chance	0.00004	6.84469	1.86122	375.87	0.16504	-0.00001	0.00173	-0.00003	0.00004
Kidd 9	-0.00003	5.45583		506.52	0.13320	-0.00001	0.00152	-0.00003	0.00001
Oil Sales	0.00003	9.80098	1.63791	415.4	0.32468	-0.00001	0.00249	-0.00003	0.00011
M-14 brine	0.00597	16.31689	5.38110	67000	154.00555	-0.00087	-0.01363	0.00921	-0.00206

Sample ID	V	Zn
Well 1904	0.00056	-0.00030
Ford A Battery	0.00044	0.10779
Well 1608	0.00038	0.02267
Near 3706		
CO_2 Facility	0.00098	0.10068
Cannon #7	0.00075	0.03343
Autry		
Chance	0.00042	0.03925
Kidd 9	0.00087	0.03585
Oil Sales	0.00050	0.07155
M-14 brine	-0.00105	-0.65549

Appendix B: Grain Size Analysis Results

Field ID	Sample Name	Measurement Date	Concentration	Laser Obscuration	Weighted Residual
			%	%	%
Hastings #7240 M-6 3218 ft	Average of 'Average of 'TGC-001 split 3500rpm'	8/15/2012 15:06	0.03	11.78	0.26
Hastings #6604-4996-5020ft #1	Average of 'TGC-002' 3000 rpm	8/15/2012 15:40	0.59	19.06	0.29
Hastings #6604-4996-5020ft #2	Average of 'TGC-003'	8/15/2012 16:56	0.05	13.70	0.34
Hastings #6604-5028-5060ft #1	Average of 'TGC-004 Split'	8/16/2012 14:00	0.46	16.77	0.48
Hastings #6604-5028-5060ft #2	Average of 'TGC-005 Split'	8/16/2012 15:11	0.05	22.70	0.32
Hastings #6604-5246-5277ft #1	Average of 'TGC-006 Split'	8/16/2012 16:21	0.01	12.76	0.65
Hastings #6604-5340-5377ft #1	Average of 'TGC-007 Split'	8/17/2012 13:56	0.48	17.95	0.56
Hastings #7240 M-2 2566 ft	Average of 'TGC-008 Split'	8/17/2012 14:49	0.11	19.20	0.27
Hastings #7240 M-4 3056 ft	Average of 'TGC-009 Split'	8/17/2012 15:38	0.03	15.61	0.38
Hastings #7240 M-5 3170 ft	Average of 'TGC-010 Split'	8/20/2012 12:35	0.57	16.92	0.56
Hastings #7240 M-6 3116 ft	Average of 'TGC-011 Split'	8/20/2012 14:34	0.54	16.62	0.41
Hastings #7240 M-8 3500 ft	Average of 'TGC-015 Split'	8/23/2012 12:13	0.01	20.73	0.88
Hastings #7240 M-13 5110 ft	Average of 'TGC-013 Split'	8/22/2012 13:04	0.51	17.22	0.38
Hastings #7240 3880 ft	Average of 'TGC-014 Split'	8/22/2012 14:16	0.36	16.86	0.40

APPENDIX B CONTINUED

	Cumulative percent finer (µm)							
Field ID	**Dv 10**	**Dv 50**	**Dv 90**	**2000**	**1000**	**500**	**250**	**125**
	µm	**µm**	**µm**	**%**	**%**	**%**	**%**	**%**
Hastings #7240 M-6 3218 ft	15.31	284.41	1413.22	95.687	83.049	67.710	45.509	26.349
Hastings #6604-4996-5020ft #1	149.97	223.62	334.12	100.000	100.000	99.832	63.531	2.382
Hastings #6604-4996-5020ft #2	104.47	195.03	301.25	100.000	100.000	100.000	75.509	14.863
Hastings #6604-5028-5060ft #1	131.15	205.85	327.69	100.000	100.000	99.721	69.971	7.422
Hastings #6604-5028-5060ft #2	10.90	155.91	269.25	100.000	100.000	99.994	85.988	33.343
Hastings #6604-5246-5277ft #1	2.33	75.49	173.62	100.000	100.000	100.000	98.339	75.407
Hastings #6604-5340-5377ft #1	120.79	197.08	350.65	99.564	97.802	95.971	71.044	11.688
Hastings #7240 M-2 2566 ft	51.85	420.53	1914.49	91.196	68.352	52.445	42.780	29.428
Hastings #7240 M-4 3056 ft	3.82	96.67	246.37	100.000	100.000	99.758	90.385	62.650
Hastings #7240 M-5 3170 ft	145.54	288.76	675.46	97.933	93.259	82.816	39.138	6.559
Hastings #7240 M-6 3116 ft	162.52	241.51	358.88	100.000	100.000	99.708	54.249	1.087
Hastings #7240 M-8 3500 ft	1.30	4.23	125.18	99.986	99.646	98.470	96.075	89.982
Hastings #7240 M-13 5110 ft	144.20	220.45	338.41	100.000	100.000	99.761	64.182	3.903
Hastings #7240 3880 ft	181.20	309.12	506.01	100.000	100.000	89.305	30.474	2.441

APPENDIX B CONTINUED

	Cumulative percent finer (µm)			% Volume in size bin (Low Diameter (µm))				
Field ID	**62.5**	**15**	**2**					
	%	**%**	**%**	**3500.00**	**3080.54**	**2711.36**	**2386.42**	**2100.42**
Hastings #7240 M-6 3218 ft	15.875	9.961	2.717	0.00	0.37	0.74	1.09	1.43
Hastings #6604-4996-5020ft #1	0.000	0.000	0.000	0.00	0.00	0.00	0.00	0.00
Hastings #6604-4996-5020ft #2	8.109	6.514	2.472	0.00	0.00	0.00	0.00	0.00
Hastings #6604-5028-5060ft #1	0.000	0.000	0.000	0.00	0.00	0.00	0.00	0.00
Hastings #6604-5028-5060ft #2	14.162	10.643	4.285	0.00	0.00	0.00	0.00	0.00
Hastings #6604-5246-5277ft #1	43.273	25.413	8.718	0.00	0.00	0.00	0.00	0.00
Hastings #6604-5340-5377ft #1	0.000	0.000	0.000	0.00	0.02	0.07	0.11	0.16
Hastings #7240 M-2 2566 ft	13.137	4.903	1.239	0.00	0.78	1.53	2.25	2.90
Hastings #7240 M-4 3056 ft	31.654	17.661	4.806	0.00	0.00	0.00	0.00	0.00
Hastings #7240 M-5 3170 ft	2.083	0.026	0.000	0.00	0.19	0.36	0.53	0.68
Hastings #7240 M-6 3116 ft	0.000	0.000	0.000	0.00	0.00	0.00	0.00	0.00
Hastings #7240 M-8 3500 ft	80.951	71.652	22.541	0.00	0.00	0.00	0.00	0.01
Hastings #7240 M-13 5110 ft	0.000	0.000	0.000	0.00	0.00	0.00	0.00	0.00
Hastings #7240 3880 ft	1.944	1.025	0.047	0.00	0.00	0.00	0.00	0.00

APPENDIX B CONTINUED

Field ID	% Volume in size bin (Low Diameter (μm))							
	1848.69	**1627.14**	**1432.13**	**1260.50**	**1109.44**	**976.48**	**859.45**	**756.45**
Hastings #7240 M-6 3218 ft	1.76	2.05	2.30	2.48	2.59	2.64	2.65	2.67
Hastings #6604-4996-5020ft #1	0.00	0.00	0.00	0.00	0.00	0.00	0.00	0.00
Hastings #6604-4996-5020ft #2	0.00	0.00	0.00	0.00	0.00	0.00	0.00	0.00
Hastings #6604-5028-5060ft #1	0.00	0.00	0.00	0.00	0.00	0.00	0.00	0.00
Hastings #6604-5028-5060ft #2	0.00	0.00	0.00	0.00	0.00	0.00	0.00	0.00
Hastings #6604-5246-5277ft #1	0.00	0.00	0.00	0.00	0.00	0.00	0.00	0.00
Hastings #6604-5340-5377ft #1	0.20	0.26	0.31	0.36	0.39	0.39	0.36	0.29
Hastings #7240 M-2 2566 ft	3.49	3.98	4.33	4.49	4.45	4.22	3.84	3.38
Hastings #7240 M-4 3056 ft	0.00	0.00	0.00	0.00	0.00	0.00	0.00	0.00
Hastings #7240 M-5 3170 ft	0.80	0.89	0.92	0.90	0.83	0.77	0.80	1.00
Hastings #7240 M-6 3116 ft	0.00	0.00	0.00	0.00	0.00	0.00	0.00	0.00
Hastings #7240 M-8 3500 ft	0.02	0.02	0.04	0.07	0.10	0.12	0.15	0.18
Hastings #7240 M-13 5110 ft	0.00	0.00	0.00	0.00	0.00	0.00	0.00	0.00
Hastings #7240 3880 ft	0.00	0.00	0.00	0.00	0.00	0.00	0.00	0.00

APPENDIX B CONTINUED

Field ID	% Volume in size bin (Low Diameter (μm))							
	665.79	**586.00**	**515.77**	**453.96**	**399.55**	**351.67**	**309.52**	**272.43**
Hastings #7240 M-6 3218 ft	2.73	2.87	3.09	3.39	3.75	4.08	4.35	4.47
Hastings #6604-4996-5020ft #1	0.00	0.00	0.05	0.49	1.85	4.41	7.98	11.77
Hastings #6604-4996-5020ft #2	0.00	0.00	0.00	0.00	0.05	2.70	5.43	8.59
Hastings #6604-5028-5060ft #1	0.00	0.00	0.12	0.65	1.86	3.82	6.41	9.24
Hastings #6604-5028-5060ft #2	0.00	0.00	0.00	0.02	0.27	1.39	2.88	4.80
Hastings #6604-5246-5277ft #1	0.00	0.00	0.00	0.00	0.00	0.01	0.12	0.64
Hastings #6604-5340-5377ft #1	0.23	0.24	0.42	0.92	1.86	3.30	5.21	7.41
Hastings #7240 M-2 2566 ft	2.89	2.45	2.10	1.86	1.73	1.69	1.73	1.81
Hastings #7240 M-4 3056 ft	0.00	0.02	0.12	0.40	0.83	1.35	1.97	2.65
Hastings #7240 M-5 3170 ft	1.48	2.31	3.50	4.97	6.56	8.05	9.16	9.71
Hastings #7240 M-6 3116 ft	0.00	0.00	0.01	1.18	3.30	6.56	10.38	13.76
Hastings #7240 M-8 3500 ft	0.22	0.25	0.28	0.31	0.34	0.39	0.45	0.54
Hastings #7240 M-13 5110 ft	0.00	0.00	0.08	0.66	2.20	4.69	7.88	11.13
Hastings #7240 3880 ft	0.98	2.89	5.02	7.42	9.72	11.48	12.37	12.21

APPENDIX B CONTINUED

Field ID	% Volume in size bin (Low Diameter (µm))							
	239.78	**211.04**	**185.75**	**163.49**	**143.90**	**126.65**	**111.47**	**98.11**
Hastings #7240 M-6 3218 ft	4.43	4.23	3.90	3.51	3.10	2.73	2.42	2.17
Hastings #6604-4996-5020ft #1	14.74	15.94	14.97	12.15	8.36	4.70	2.00	0.54
Hastings #6604-4996-5020ft #2	11.47	13.32	13.65	12.42	10.01	7.06	4.25	2.07
Hastings #6604-5028-5060ft #1	11.77	13.43	13.81	12.78	10.55	7.65	4.71	2.31
Hastings #6604-5028-5060ft #2	6.90	8.83	10.21	10.80	10.47	9.31	7.56	5.56
Hastings #6604-5246-5277ft #1	1.32	2.24	3.32	4.45	5.49	6.31	6.77	6.82
Hastings #6604-5340-5377ft #1	9.58	11.33	12.28	12.16	10.95	8.86	6.29	3.78
Hastings #7240 M-2 2566 ft	1.93	2.08	2.26	2.47	2.69	2.91	3.09	3.19
Hastings #7240 M-4 3056 ft	3.36	4.06	4.72	5.30	5.78	6.12	6.30	6.29
Hastings #7240 M-5 3170 ft	9.56	8.76	7.46	5.88	4.29	2.88	1.79	1.06
Hastings #7240 M-6 3116 ft	15.70	15.55	13.39	9.89	6.11	2.98	1.02	0.17
Hastings #7240 M-8 3500 ft	0.66	0.81	0.97	1.14	1.32	1.48	1.61	1.70
Hastings #7240 M-13 5110 ft	13.65	14.76	14.16	12.02	8.93	5.65	2.90	1.08
Hastings #7240 3880 ft	11.05	9.14	6.84	4.55	2.62	1.23	0.41	0.07

APPENDIX B CONTINUED

Field ID	% Volume in size bin (Low Diameter (μm))							
	86.36	**76.01**	**66.90**	**58.88**	**51.82**	**45.61**	**40.15**	**35.33**
Hastings #7240 M-6 3218 ft	1.97	1.79	1.61	1.42	1.20	0.97	0.75	0.56
Hastings #6604-4996-5020ft #1	0.05	0.00	0.00	0.00	0.00	0.00	0.00	0.00
Hastings #6604-4996-5020ft #2	0.73	0.14	0.00	0.00	0.00	0.00	0.08	0.14
Hastings #6604-5028-5060ft #1	0.77	0.11	0.00	0.00	0.00	0.00	0.00	0.00
Hastings #6604-5028-5060ft #2	3.64	2.07	0.96	0.33	0.06	0.00	0.13	0.29
Hastings #6604-5246-5277ft #1	6.47	5.78	4.89	3.93	3.04	2.29	1.74	1.39
Hastings #6604-5340-5377ft #1	1.76	0.50	0.00	0.00	0.00	0.00	0.00	0.00
Hastings #7240 M-2 2566 ft	3.18	3.05	2.80	2.43	2.01	1.56	1.13	0.77
Hastings #7240 M-4 3056 ft	6.07	5.65	5.04	4.29	3.46	2.64	1.88	1.25
Hastings #7240 M-5 3170 ft	0.65	0.48	0.45	0.47	0.47	0.44	0.37	0.28
Hastings #7240 M-6 3116 ft	0.00	0.00	0.00	0.00	0.00	0.00	0.00	0.00
Hastings #7240 M-8 3500 ft	1.74	1.71	1.64	1.51	1.34	1.17	0.99	0.84
Hastings #7240 M-13 5110 ft	0.21	0.00	0.00	0.00	0.00	0.00	0.00	0.00
Hastings #7240 3880 ft	0.00	0.00	0.00	0.11	0.16	0.19	0.18	0.15

APPENDIX B CONTINUED

Field ID	% Volume in size bin (Low Diameter (µm))							
	31.10	**27.37**	**24.09**	**21.21**	**18.66**	**16.43**	**14.46**	**12.73**
Hastings #7240 M-6 3218 ft	0.41	0.30	0.24	0.21	0.21	0.23	0.25	0.27
Hastings #6604-4996-5020ft #1	0.00	0.00	0.00	0.00	0.00	0.00	0.00	0.00
Hastings #6604-4996-5020ft #2	0.20	0.23	0.24	0.22	0.20	0.18	0.16	0.16
Hastings #6604-5028-5060ft #1	0.00	0.00	0.00	0.00	0.00	0.00	0.00	0.00
Hastings #6604-5028-5060ft #2	0.43	0.51	0.52	0.48	0.41	0.34	0.28	0.25
Hastings #6604-5246-5277ft #1	1.20	1.12	1.11	1.12	1.12	1.11	1.08	1.03
Hastings #6604-5340-5377ft #1	0.00	0.00	0.00	0.00	0.00	0.00	0.00	0.00
Hastings #7240 M-2 2566 ft	0.49	0.31	0.20	0.16	0.16	0.17	0.20	0.22
Hastings #7240 M-4 3056 ft	0.78	0.48	0.32	0.27	0.29	0.34	0.41	0.46
Hastings #7240 M-5 3170 ft	0.18	0.09	0.00	0.00	0.00	0.00	0.00	0.00
Hastings #7240 M-6 3116 ft	0.00	0.00	0.00	0.00	0.00	0.00	0.00	0.00
Hastings #7240 M-8 3500 ft	0.72	0.64	0.59	0.57	0.59	0.63	0.71	0.83
Hastings #7240 M-13 5110 ft	0.00	0.00	0.00	0.00	0.00	0.00	0.00	0.00
Hastings #7240 3880 ft	0.11	0.07	0.00	0.00	0.00	0.00	0.00	0.00

APPENDIX B CONTINUED

Field ID	% Volume in size bin (Low Diameter (µm))							
	11.20	**9.86**	**8.68**	**7.64**	**6.72**	**5.92**	**5.21**	**4.58**
Hastings #7240 M-6 3218 ft	0.29	0.32	0.34	0.37	0.41	0.45	0.49	0.53
Hastings #6604-4996-5020ft #1	0.00	0.00	0.00	0.00	0.00	0.00	0.00	0.00
Hastings #6604-4996-5020ft #2	0.16	0.18	0.20	0.22	0.24	0.26	0.28	0.29
Hastings #6604-5028-5060ft #1	0.00	0.00	0.00	0.00	0.00	0.00	0.00	0.00
Hastings #6604-5028-5060ft #2	0.25	0.27	0.30	0.34	0.38	0.41	0.44	0.46
Hastings #6604-5246-5277ft #1	0.99	0.96	0.94	0.95	0.98	1.02	1.06	1.10
Hastings #6604-5340-5377ft #1	0.00	0.00	0.00	0.00	0.00	0.00	0.00	0.00
Hastings #7240 M-2 2566 ft	0.23	0.23	0.23	0.23	0.23	0.23	0.24	0.24
Hastings #7240 M-4 3056 ft	0.51	0.55	0.60	0.65	0.71	0.79	0.87	0.94
Hastings #7240 M-5 3170 ft	0.01	0.01	0.01	0.01	0.00	0.00	0.00	0.00
Hastings #7240 M-6 3116 ft	0.00	0.00	0.00	0.00	0.00	0.00	0.00	0.00
Hastings #7240 M-8 3500 ft	1.00	1.23	1.53	1.90	2.34	2.82	3.32	3.80
Hastings #7240 M-13 5110 ft	0.00	0.00	0.00	0.00	0.00	0.00	0.00	0.00
Hastings #7240 3880 ft	0.00	0.02	0.05	0.07	0.07	0.08	0.08	0.08

APPENDIX B CONTINUED

Field ID	% Volume in size bin (Low Diameter (µm))							
	4.03	**3.55**	**3.12**	**2.75**	**2.42**	**2.13**	**1.88**	**1.65**
Hastings #7240 M-6 3218 ft	0.56	0.59	0.60	0.59	0.57	0.54	0.50	0.45
Hastings #6604-4996-5020ft #1	0.00	0.00	0.00	0.00	0.00	0.00	0.00	0.00
Hastings #6604-4996-5020ft #2	0.30	0.30	0.31	0.31	0.31	0.31	0.31	0.31
Hastings #6604-5028-5060ft #1	0.00	0.00	0.00	0.00	0.00	0.00	0.00	0.00
Hastings #6604-5028-5060ft #2	0.48	0.49	0.50	0.50	0.49	0.48	0.46	0.45
Hastings #6604-5246-5277ft #1	1.14	1.16	1.16	1.15	1.13	1.09	1.05	1.02
Hastings #6604-5340-5377ft #1	0.00	0.00	0.00	0.00	0.00	0.00	0.00	0.00
Hastings #7240 M-2 2566 ft	0.25	0.25	0.25	0.24	0.23	0.22	0.20	0.18
Hastings #7240 M-4 3056 ft	1.01	1.05	1.08	1.07	1.03	0.97	0.89	0.81
Hastings #7240 M-5 3170 ft	0.00	0.00	0.00	0.00	0.00	0.00	0.00	0.00
Hastings #7240 M-6 3116 ft	0.00	0.00	0.00	0.00	0.00	0.00	0.00	0.00
Hastings #7240 M-8 3500 ft	4.23	4.57	4.80	4.89	4.84	4.65	4.33	3.95
Hastings #7240 M-13 5110 ft	0.00	0.00	0.00	0.00	0.00	0.00	0.00	0.00
Hastings #7240 3880 ft	0.08	0.08	0.09	0.08	0.08	0.07	0.06	0.02

APPENDIX B CONTINUED

Field ID	% Volume in size bin (Low Diameter (μm))							
	1.45	**1.28**	**1.13**	**0.99**	**0.87**	**0.77**	**0.68**	**0.59**
Hastings #7240 M-6 3218 ft	0.41	0.38	0.36	0.32	0.26	0.18	0.10	0.00
Hastings #6604-4996-5020ft #1	0.00	0.00	0.00	0.00	0.00	0.00	0.00	0.00
Hastings #6604-4996-5020ft #2	0.31	0.32	0.33	0.32	0.29	0.23	0.15	0.07
Hastings #6604-5028-5060ft #1	0.00	0.00	0.00	0.00	0.00	0.00	0.00	0.00
Hastings #6604-5028-5060ft #2	0.46	0.48	0.52	0.54	0.52	0.45	0.34	0.21
Hastings #6604-5246-5277ft #1	1.02	1.07	1.13	1.14	1.05	0.84	0.56	0.28
Hastings #6604-5340-5377ft #1	0.00	0.00	0.00	0.00	0.00	0.00	0.00	0.00
Hastings #7240 M-2 2566 ft	0.17	0.16	0.16	0.15	0.14	0.11	0.07	0.00
Hastings #7240 M-4 3056 ft	0.74	0.68	0.63	0.56	0.45	0.31	0.16	0.00
Hastings #7240 M-5 3170 ft	0.00	0.00	0.00	0.00	0.00	0.00	0.00	0.00
Hastings #7240 M-6 3116 ft	0.00	0.00	0.00	0.00	0.00	0.00	0.00	0.00
Hastings #7240 M-8 3500 ft	3.58	3.24	2.91	2.51	1.97	1.32	0.68	0.20
Hastings #7240 M-13 5110 ft	0.00	0.00	0.00	0.00	0.00	0.00	0.00	0.00
Hastings #7240 3880 ft	0.00	0.00	0.00	0.00	0.00	0.00	0.00	0.00

APPENDIX B CONTINUED

Field ID	% Volume in size bin (Low Diameter (µm))								
	1.45	**1.28**	**1.13**	**0.99**	**0.87**	**0.77**	**0.68**	**0.59**	**0.52**
Hastings #7240 M-6 3218 ft	0.41	0.38	0.36	0.32	0.26	0.18	0.10	0.00	0.00
Hastings #6604-4996-5020ft #1	0.00	0.00	0.00	0.00	0.00	0.00	0.00	0.00	0.00
Hastings #6604-4996-5020ft #2	0.31	0.32	0.33	0.32	0.29	0.23	0.15	0.07	0.00
Hastings #6604-5028-5060ft #1	0.00	0.00	0.00	0.00	0.00	0.00	0.00	0.00	0.00
Hastings #6604-5028-5060ft #2	0.46	0.48	0.52	0.54	0.52	0.45	0.34	0.21	0.09
Hastings #6604-5246-5277ft #1	1.02	1.07	1.13	1.14	1.05	0.84	0.56	0.28	0.08
Hastings #6604-5340-5377ft #1	0.00	0.00	0.00	0.00	0.00	0.00	0.00	0.00	0.00
Hastings #7240 M-2 2566 ft	0.17	0.16	0.16	0.15	0.14	0.11	0.07	0.00	0.00
Hastings #7240 M-4 3056 ft	0.74	0.68	0.63	0.56	0.45	0.31	0.16	0.00	0.00
Hastings #7240 M-5 3170 ft	0.00	0.00	0.00	0.00	0.00	0.00	0.00	0.00	0.00
Hastings #7240 M-6 3116 ft	0.00	0.00	0.00	0.00	0.00	0.00	0.00	0.00	0.00
Hastings #7240 M-8 3500 ft	3.58	3.24	2.91	2.51	1.97	1.32	0.68	0.20	0.00
Hastings #7240 M-13 5110 ft	0.00	0.00	0.00	0.00	0.00	0.00	0.00	0.00	0.00
Hastings #7240 3880 ft	0.00	0.00	0.00	0.00	0.00	0.00	0.00	0.00	0.00

Appendix C: X-Ray Diffraction Results

Hastings Well	Depth (ft)	Quartz	K-feldspar	Albite	Illite	Kaolinte	Calcite	Pyrite	Dolomite	Total
		%	%	%	%	%	%	%	%	%
WHU 7240	2566	17.07	6.28	1.56	39.71	3.54	29.77	0.6	1.46	99.99
WHU 7240	3056	24.36	5.44	2.23	29.19	2.81	34.16	1.81	0	100
WHU 7240	3116	48.44	5.49	0.94	24.61	2.42	17.07	1.04	0	100.01
WHU 7240	3210	20.84	3.6	0.91	34.35	3.58	34.23	2.49	0	100
WHU 7240	3836	68.21	11.38	3.7	11.06	0	5.2	0.45	0	100

Appendix D: Hastings Model Input Parameters

Hastings Formation	Depth (meters)	Geochemistry Solution Number	Hastings Formation	Depth (meters)	Geochemistry Solution Number
Chicot Aquifer	0-220	4	M-9	652-693	3
Evangeline Aquifer	220-402	4	Confining Unit	693-703	2
Confining Unit	402-412	2	M-10	703-793	3
M-4	412-447	3	Confining Unit	793-803	2
Confining Unit	447-457	2	M-11	803-935	3
M-5	457-506	3	Confining Unit	935-945	2
Confining Unit	506-516	2	M-12	945-1008	3
M-6	516-573	3	Confining Unit	1008-1018	2
Confining Unit	573-583	2	M-13	1018-1318	3
M-7	583-629	3	Confining Unit	1318-1328	2
Confining Unit	629-639	2	M-14	1328-1374	3
M-8	639-642	3	Anahuac Shale	1374-1627	2
Confining Unit	642-652	2	Frio Sandstone	1627-1677	1

APPENDIX D HASTINGS MODEL INPUT PARAMETERS CONTINUED

	1: Frio Brine[1]	**2: WHU 7707**	**3: M-14 Brine**	**4: Hastings CO_2 Facility**
Temperature (°C)	52.3	46.1	52.3	24.32
pH	3.44	6.79	6.19	7.78
Br (mg/l)	7999	0	0	0
Ca (mg/l)	3254	540	2641	23
Mg (mg/l)	403	240	596	5.8
Na (mg/l)	56990	43668	33699	173
Cl (mg/l)	90760	69000	59288	143
HCO_3 (mg/l)	55860	207	0	412
Depth of sample (m)	1776	1615	1320	46
[1]Collected Frio brine sample was modeled to react with 66.33 g of CO_2 gas and buffered with 10 mol of pure phase calcite				

Appendix E: Statistical Analyses for Hastings Data

The MATLAB application Distribution Fit (*distfit*) was used to determine the best fit for creating a sampling data set from the original Hastings permeabilities shown below. A beta fit distribution (Figure D.1) was used to ensure that no negative permeability values would be used in any model realizations, as this would cause model errors.

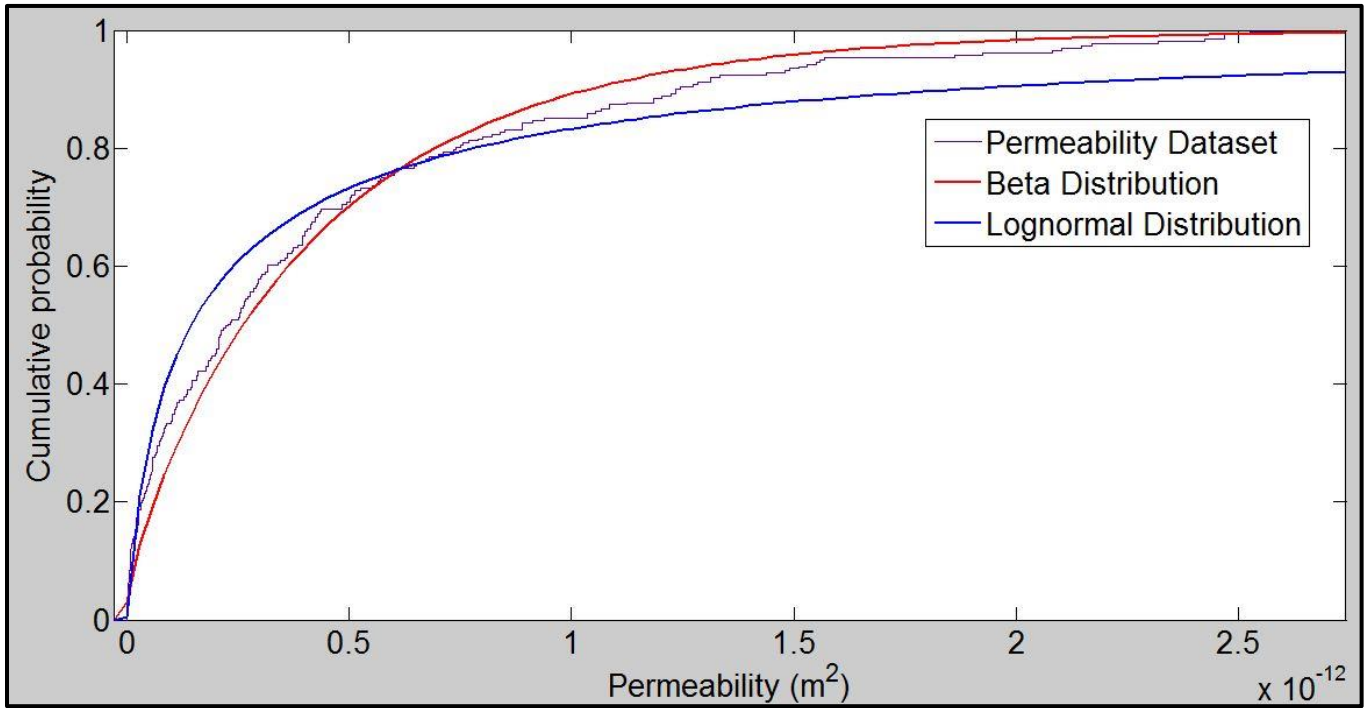

Figure D.1: Hastings permeability dataset, beta vs. lognormal distribution fit.

ID	Depth (m)	Porosity	Perm (m/s)	ID	Depth (m)	Porosity	Perm (m/s)
WHU 1814	818	0.304	1.41E-05	WHU 5003	1667	0.264	5.22E-07
WHU 1814	840	0.301	1.21E-05	WHU 5003	1673	0.258	6.38E-07
WHU 1814	894	0.345	2.42E-05	WHU 5003	1676	0.245	2.03E-07
WHU 1814	988	0.312	4.05E-06	WHU 5003	1678	0.268	1.64E-07
WHU 1814	1096	0.311	4.95E-06	WHU 5003	1683	0.246	3.97E-08
WHU 1814	1123	0.273	1.15E-06	WHU 5003	1684	0.292	2.03E-06
WHU 1814	1164	0.27	2.51E-07	WHU 5003	1690	0.295	2.71E-06
WHU 1814	1173	0.22	3.10E-08	WHU 5003	1754	0.24	9.58E-08
WHU 1814	1396	0.137	2.90E-09	WHU 5003	1756	0.288	5.71E-07
WHU 1814	1408	0.305	4.26E-06	WHU 5003	1762	0.287	3.48E-06
WHU 1814	1746	0.334	1.52E-05	WHU 5003	1764	0.248	3.87E-08
WHU 1814	1748	0.325	4.93E-06	WHU 5003	1768	0.308	1.26E-05
WHU 1814	1750	0.298	2.85E-06	WHU 5003	1771	0.257	2.71E-07
WHU 1814	1752	0.341	5.90E-06	WHU 5003	1772	0.221	2.51E-08
WHU 1814	1755	0.346	1.02E-06	WHU 5003	1776	0.237	9.48E-08
WHU 1814	1756	0.355	8.71E-06	WHU 5003	1779	0.248	7.83E-08
WHU 1814	1757	0.277	2.32E-07	WHU 5106	1067	0.328	3.68E-06
WHU 1814	1763	0.327	3.92E-06	WHU 5106	1073	0.313	7.25E-06
WHU 1814	1775	0.267	2.71E-07	WHU 5106	1653	0.269	1.79E-06
WHU 1814	1790	0.32	1.98E-06	WHU 5106	1654	0.331	9.19E-06
WHU 1814	1793	0.312	1.06E-06	WHU 5106	1656	0.334	8.22E-06
WHU 1814	1819	0.336	4.91E-06	WHU 5106	1659	0.296	3.10E-06

ID	Depth (m)	Porosity	Perm (m/s)	ID	Depth (m)	Porosity	Perm (m/s)
WHU 1903	550	0.281	3.10E-06	WHU 5106	1663	0.348	1.16E-05
WHU 1903	718	0.25	2.51E-07	WHU 5106	1668	0.334	1.02E-05
WHU 1903	720	0.263	5.80E-08	WHU 5106	1670	0.341	2.42E-05
WHU 1903	779	0.302	3.93E-06	WHU 5106	1678	0.336	1.06E-05
WHU 1903	1698	0.267	1.10E-06	WHU 5106	1679	0.338	1.31E-05
WHU 1903	1700	0.31	5.59E-06	WHU 5106	1684	0.329	1.21E-05
WHU 1903	1701	0.291	3.05E-06	WHU 5106	1690	0.319	4.74E-06
WHU 1903	1702	0.287	1.74E-06	WHU 5106	1693	0.293	1.84E-06
WHU 1903	1703	0.276	7.25E-07	WHU 5106	1695	0.309	3.87E-06
WHU 1903	1705	0.261	2.22E-07	WHU 5106	1703	0.337	5.42E-06
WHU 1903	1707	0.296	2.47E-06	WHU 5106	1705	0.336	6.87E-06
WHU 1903	1710	0.29	7.84E-06	WHU 5106	1711	0.329	3.68E-06
WHU 1903	1711	0.317	1.22E-05	WHU 5106	1715	0.284	2.56E-06
WHU 1903	1724	0.292	8.05E-06	WHU 5106	1718	0.289	1.02E-06
WHU 1903	1729	0.28	7.25E-07	WHU 5106	1746	0.324	1.06E-05
WHU 1903	1732	0.268	1.26E-07	WHU 5106	1747	0.334	5.61E-06
WHU 1903	1738	0.328	1.02E-05	WHU 5106	1754	0.31	1.89E-05
WHU 1903	1743	0.322	6.48E-06	WHU 5106	1759	0.282	8.42E-07
WHU 1903	1747	0.248	6.09E-08	WHU 5106	1762	0.304	1.45E-06
WHU 1903	1758	0.322	5.54E-06	WHU 5106	1765	0.289	8.71E-07
WHU 1903	1771	0.253	7.45E-08	WHU 5106	1768	0.315	8.71E-06
WHU 1903	1796	0.271	4.45E-07	WHU 5106	1771	0.297	6.58E-07
WHU 1903	1807	0.259	9.48E-08	WHU 5106	1772	0.243	8.12E-08
WHU 1903	1817	0.299	6.34E-06	WHU 5106	1779	0.27	3.19E-07

ID	Depth (m)	Porosity	Perm (m/s)	ID	Depth (m)	Porosity	Perm (m/s)
WHU 1903	1824	0.277	3.48E-07	WHU 5106	1780	0.303	3.87E-06
WHU 1903	1827	0.272	1.10E-06	WHU 5106	1783	0.244	7.35E-08
WHU 1903	1844	0.247	7.06E-08	WHU 5106	1788	0.268	4.55E-07
WHU 1903	1853	0.301	5.15E-06	WHU 5106	1791	0.279	1.31E-06
WHU 1903	1862	0.325	2.48E-05	WHU 5106	1799	0.327	8.22E-07
WHU 1903	1877	0.323	2.04E-05	WHU 5106	1805	0.242	6.96E-08
WHU 2703	711	0.196	2.90E-09	WHU 5106	1821	0.252	9.09E-08
WHU 2703	729	0.327	1.48E-05	WHU 5106	1828	0.288	5.03E-06
WHU 2703	952	0.303	6.58E-06	WHU 5106	1831	0.328	2.13E-05
WHU 2703	1013	0.299	5.32E-07	WHU 5106	1885	0.226	4.35E-08
WHU 2703	1218	0.296	2.03E-06	WHU 5106	2009	0.312	2.66E-05
WHU 2703	1374	0.117	9.67E-10	WHU 5305	1442	0.307	5.90E-06
WHU 2703	1688	0.332	1.25E-05	WHU 5305	1442	0.287	2.80E-06
WHU 2703	1696	0.317	5.95E-06	WHU 5305	1442	0.28	2.52E-06
WHU 2703	1701	0.313	7.40E-06	WHU 5305	1479	0.272	1.06E-06
WHU 2703	1702	0.283	4.21E-06	WHU 5305	1480	0.241	5.71E-07
WHU 2703	1703	0.325	7.74E-06	WHU 5305	1480	0.277	2.22E-06
WHU 2703	1705	0.307	1.50E-05	WHU 5305	1480	0.24	8.32E-07
WHU 2703	1708	0.301	1.26E-06	WHU 5305	1481	0.259	1.01E-06
WHU 2703	1710	0.296	1.29E-05	WHU 5305	1481	0.262	1.33E-06
WHU 2703	1712	0.306	7.21E-06	WHU 5305	1604	0.224	2.42E-07
WHU 2703	1718	0.293	2.03E-06	WHU 5305	1604	0.254	7.93E-07
WHU 2703	1722	0.29	1.40E-06	WHU 5305	1605	0.243	5.71E-07
WHU 2703	1723	0.324	7.54E-06	WHU 5305	1715	0.322	1.10E-05

ID	Depth (m)	Porosity	Perm (m/s)	ID	Depth (m)	Porosity	Perm (m/s)
WHU 2703	1726	0.314	1.53E-05	WHU 5305	1715	0.325	1.03E-05
WHU 2703	1731	0.309	6.96E-06	WHU 5305	1716	0.262	2.07E-06
WHU 2703	1736	0.313	5.76E-06	WHU 5305	1716	0.295	3.78E-06
WHU 2703	1737	0.319	1.20E-05	WHU 5305	1718	0.3	4.29E-06
WHU 2703	1747	0.276	4.35E-07	WHU 5305	1718	0.272	2.91E-06
WHU 2703	1764	0.189	9.67E-10	WHU 5305	1719	0.28	2.50E-06
WHU 2703	1790	0.338	1.46E-05	WHU 5305	1719	0.294	2.68E-06
WHU 2703	1794	0.245	5.42E-08	WHU 5305	1719	0.265	2.31E-06
WHU 2703	1806	0.23	3.39E-08	WHU 5305	1720	0.261	1.89E-06
WHU 2703	1811	0.326	4.74E-06	WHU 5305	1720	0.27	2.49E-06
WHU 2703	1814	0.273	1.26E-06	WHU 5305	1721	0.276	3.35E-06
WHU 2703	1818	0.276	5.71E-07	WHU 5305	1721	0.262	2.04E-06
WHU 2703	1837	0.325	3.87E-06	WHU 5305	1722	0.271	2.98E-06
WHU 2703	1850	0.233	5.90E-08	WHU 5305	1722	0.283	3.53E-06
WHU 2703	1855	0.326	1.54E-05	WHU 5305	1723	0.274	2.61E-06
WHU 2703	1868	0.294	4.84E-06	WHU 5305	1724	0.264	1.98E-06
WHU 2703	1878	0.312	1.04E-05	WHU 5305	1725	0.258	1.07E-06
WHU 4842	857	0.306	8.71E-06	WHU 5305	1725	0.244	7.93E-07
WHU 4842	892	0.254	9.67E-08	WHU 5305	1725	0.264	1.58E-06
WHU 4842	892	0.339	1.29E-05	WHU 5305	1725	0.249	5.71E-07
WHU 4842	1032	0.286	5.51E-06	WHU 5305	1726	0.246	3.10E-07
WHU 4842	1037	0.244	8.22E-08	WHU 5305	1726	0.238	2.61E-07
WHU 4842	1078	0.296	6.38E-06	WHU 5305	1727	0.245	3.87E-07
WHU 4842	1081	0.218	2.13E-08	WHU 5305	1727	0.255	5.61E-07

ID	Depth (m)	Porosity	Perm (m/s)	ID	Depth (m)	Porosity	Perm (m/s)
WHU 4842	1090	0.215	9.67E-10	WHU 5305	1729	0.242	3.97E-07
WHU 4842	1112	0.261	6.09E-07	WHU 5305	1736	0.334	2.27E-05
WHU 4842	1114	0.291	2.03E-06	WHU 5305	1736	0.329	2.10E-05
WHU 4842	1122	0.304	1.16E-05	WHU 5305	1736	0.188	2.90E-08
WHU 4842	1212	0.288	1.74E-06	WHU 5305	1737	0.268	2.79E-06
WHU 4842	1346	0.263	1.45E-06	WHU 5305	1739	0.274	3.38E-06
WHU 4842	1746	0.219	8.71E-09	WHU 5305	1739	0.292	4.08E-06
WHU 4842	1753	0.299	3.10E-06	WHU 5305	1740	0.213	1.84E-07
WHU 4842	1756	0.287	9.67E-07	WHU 5305	1741	0.285	3.54E-06
WHU 4842	1757	0.311	5.03E-06	WHU 5305	1741	0.27	2.91E-06
WHU 4842	1759	0.288	6.67E-06	WHU 5305	1741	0.257	1.44E-06
WHU 4842	1764	0.273	1.79E-06	WHU 5305	1742	0.232	4.06E-07
WHU 4842	1766	0.289	2.03E-06	WHU 5305	1742	0.316	8.95E-06
WHU 4842	1769	0.294	4.06E-06	WHU 5305	1743	0.303	8.32E-06
WHU 4842	1770	0.297	3.87E-06	WHU 5305	1751	0.318	1.82E-05
WHU 4842	1773	0.294	1.55E-06	WHU 5305	1751	0.325	2.06E-05
WHU 4842	1777	0.284	1.79E-06	WHU 5305	1752	0.331	2.37E-05
WHU 4842	1778	0.315	4.16E-06	WHU 5305	1771	0.273	3.97E-06
WHU 4842	1781	0.276	2.13E-06	WHU 5305	1771	0.261	2.88E-06
WHU 4842	1793	0.271	7.35E-07	WHU 5305	1771	0.27	3.64E-06
WHU 4842	1799	0.278	2.51E-06	WHU 5305	1778	0.234	3.19E-07
WHU 4842	1799	0.341	1.45E-05	WHU 5305	1779	0.246	5.71E-07
WHU 4842	1802	0.297	4.16E-06	WHU 5305	1779	0.255	6.77E-07
WHU 4842	1804	0.278	2.71E-06	WHU 5305	1779	0.274	1.95E-06

ID	Depth (m)	Porosity	Perm (m/s)	ID	Depth (m)	Porosity	Perm (m/s)
WHU 4842	1812	0.269	2.81E-07	WHU 5305	1779	0.287	2.60E-06
WHU 4842	1820	0.341	1.18E-05	WHU 5305	1786	0.187	3.48E-08
WHU 4842	1822	0.293	7.35E-06	WHU 5305	1787	0.253	5.22E-07
WHU 4842	1833	0.267	6.58E-07	WHU 5305	1787	0.268	7.64E-07
WHU 4842	1859	0.178	1.93E-09	WHU 5910	944	0.174	1.35E-07
WHU 5003	1067	0.272	2.08E-06	WHU 5910	946	0.265	2.61E-08
WHU 5003	1653	0.285	2.95E-06	WHU 5910	950	0.221	3.68E-07
WHU 5003	1654	0.299	2.27E-06	WHU 5910	985	0.26	4.84E-07
WHU 5003	1654	0.275	2.18E-06	WHU 5910	986	0.325	1.33E-06
WHU 5003	1659	0.231	6.00E-08	WHU 5910	1057	0.293	1.57E-06
WHU 5003	1660	0.246	2.51E-07	WHU 5910	1060	0.234	1.54E-06
WHU 5003	1664	0.265	5.03E-07	WHU 5910	1065	0.293	2.59E-06
				WHU 5910	1070	0.286	4.21E-06

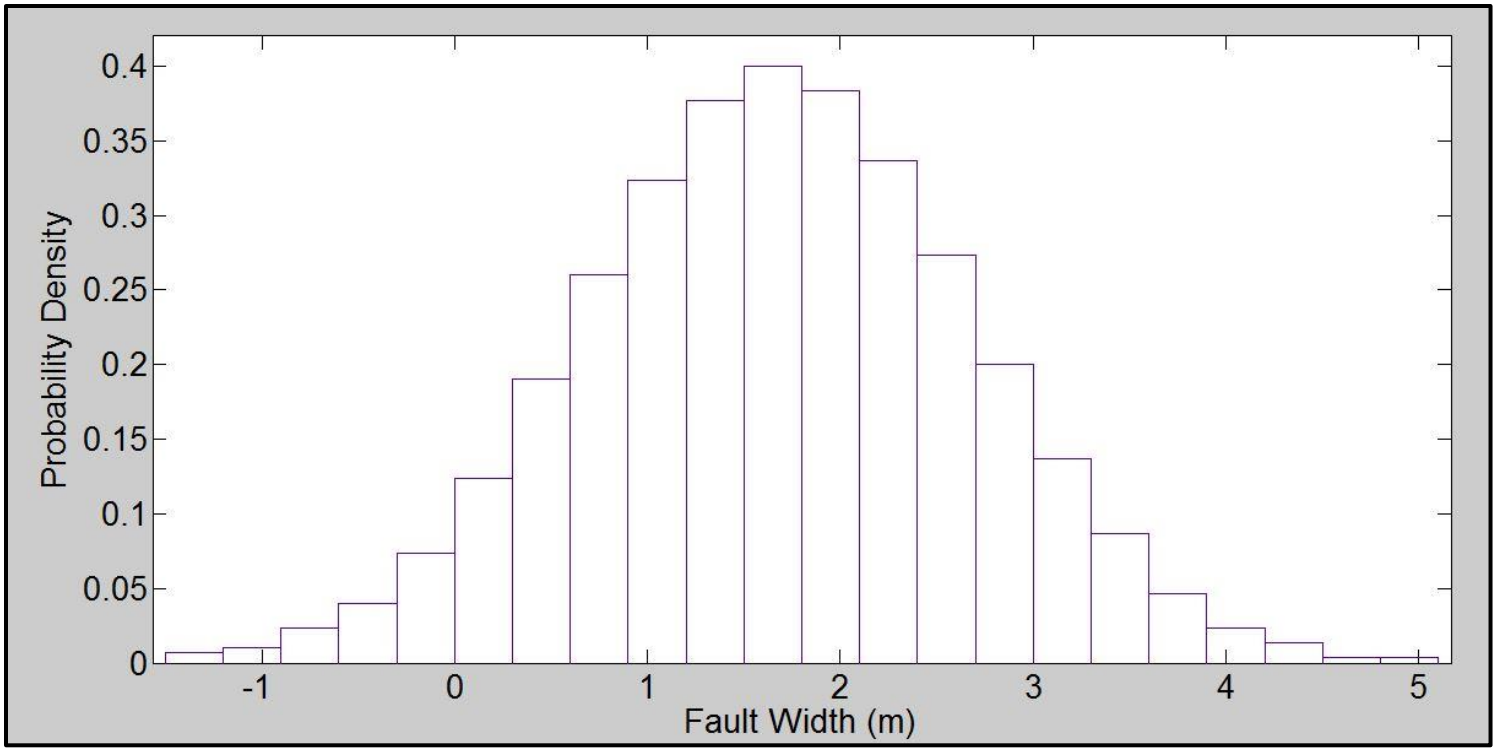

Figure D.2: Hastings fault width data set, normally distributed.

Model inputs for fault width (in meters) were sampled via Latin Hyper Cube from 1000 samples normally distributed around 1.68 meters, which is arbitrary.

Appendix E Analytical Pressure Model Equations

All equations below are sourced from Zeidouni (2012). Refer to Appendix E Figure 1 for model region breakdowns.

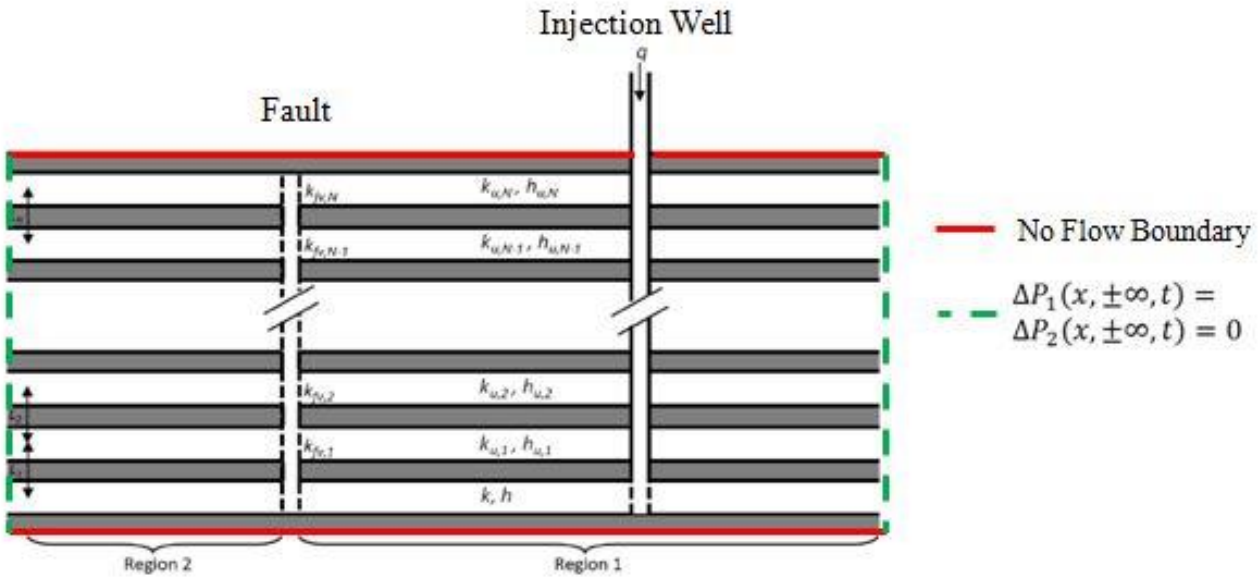

Figure E.1: Model geometry from Zeidouni (2012) where *k* is formation permeability and *h* is formation thickness.

$$\frac{\partial^2 \Delta P_1}{\partial x^2} + \frac{\partial^2 \Delta P_1}{\partial y^2} + \frac{q\mu}{kh}\delta(x-a)\delta(y) = \frac{1}{\eta}\frac{\partial \Delta P_1}{\partial t} \quad \text{(E.1)}$$

Modified diffusivity Equation (E.1) for flow in the injection zone and all above-zone monitoring intervals (AZMI), where δ is the Dirac delta function, q is the volumetric injection rate, μ is the fluid viscosity, k, h, and η are the formation permeability, thickness, and diffusivity coefficient, respectively.

$$\Delta P_1(x, y, 0) = \Delta P_2(x, y, 0) = 0 \quad \text{(E.2)}$$

$$\Delta P_1(x, \pm\infty, t) = \Delta P_2(x, \pm\infty, t) = 0 \quad \text{(E.3)}$$

$$\Delta P_1(+\infty, y, t) = \Delta P_2(-\infty, y, t) = 0 \quad \text{(E.4)}$$

$$\frac{kh}{\mu}\frac{\partial \Delta P_1(0, y, t)}{\partial x} = \frac{k_{fh}h}{\mu w_f}\left(\Delta P_1(0, y, t) - \Delta P_2(0, y, t)\right) + \frac{k_{fv}w_f}{2\mu L}\left(\Delta P_1(0, y, t) - \Delta P_{u1}(0, y, t)\right) \quad \text{(E.5)}$$

$$\frac{kh}{\mu}\frac{\partial \Delta P_2(0, y, t)}{\partial x} + \frac{k_{fv}w_f}{2\mu L}\left(\Delta P_2(0, y, t) - \Delta P_{u2}(0, y, t)\right) = \frac{k_{fh}h}{\mu w_f}\left(\Delta P_1(0, y, t) - \Delta P_2(0, y, t)\right) \quad \text{(E.6)}$$

where Equation (E.2) ensures transient pressure conditions in all x and y directions for all formations, Equation (E.3) and (E.4) account for the negligible effects of pressure at the infinite lateral boundaries (i.e., infinite boundary conditions) for all formations, Equation (E.5) states that the fault outflow at region 1 is the sum of the flow toward region 2 and the vertical leakage rate at the side of region 1, Equation (E.6) presents the relationships between flow rate entering region 2, pressure difference on two sides of the fault, and leakage to region 2 of the fault.

$$\frac{k_{fv}w_f}{2\mu L}\left(\Delta P_1(0,y,t)-\Delta P_{u1}(0,y,t)\right)+\frac{k_u h_u}{\mu}\frac{\partial \Delta P_{u1}(0,y,t)}{\partial x}=\frac{k_{fh}h_u}{\mu w_f}\left(\Delta P_{u1}(0,y,t)-\Delta P_{u2}(0,y,t)\right) \tag{E.7}$$

$$\frac{k_{fv}w_f}{2\mu L}\left(\Delta P_2(0,y,t)-\Delta P_{u2}(0,y,t)\right)+\frac{k_{fh}h_u}{\mu w_f}\left(\Delta P_{u1}(0,y,t)-\Delta P_{u2}(0,y,t)\right)=\frac{k_u h_u}{\mu}\frac{\partial \Delta P_{u2}(0,y,t)}{\partial x} \tag{E.8}$$

Equation (E.7) asserts that leakage from region 1 is the sum of the inflow to region 1 of the AZMI formations and across-fault flow in the upper zone. Equation (E.8) relates leakage rate at region 2 to the across-fault flow in the AZMI formations and the inflow of region 2 of the upper zone.

The system is reduced to a system of coupled ODE's using the Laplace transform in time and the exponential Fourier transform in y-coordinate, defined by Equations (E.9) and (E.10)

$$\overline{\Delta P}(x,y,s) = \mathcal{L}\left\{\Delta P(x,y,t)\right\} = \int_0^\infty \Delta P(x,y,t)\, e^{-st}\, dt \qquad \text{(E.9)}$$

$$\overline{\overline{\Delta P}}(x,\omega,s) = \mathcal{F}\left\{\overline{\Delta P}(x,y,s)\right\} = \int_{-\infty}^{\infty} \overline{\Delta P}(x,y,s)\, e^{i\omega y}\, dy \qquad \text{(E.10)}$$

Equations (E.9) and (E.10) are solved to provide dimensionless pressure changes in both Regions 1 and 2 of the injection and AZMI formations, in Equations (E.11) and (E.12), respectively:

$$\overline{\overline{P}}_{D1} = \frac{1}{2sA}\left(e^{-A|x_D-1|} + \frac{A^2(\alpha_u + A_uT_D)(\alpha_u + A_uT_D + 2\alpha h_D) - 2\alpha\alpha_u A_uT_D(\alpha_u + 2\alpha h_D + \alpha_u h_D + A_uT_D) - \alpha_u A_uT_D\alpha_u}{(Aa_u + AA_uT_D + a_uA_uT_D)(2aa_u + Aa_u + 4a^2h_D + 2aAh_D + 2aa_uh_D + 2aA_uT_D + AA_uT_D + a_uA_uT_D)} e^{-A(x_D+1)} \right) \qquad \text{(E.11)}$$

$$\overline{\overline{P}}_{Du1} = \frac{\alpha_u}{s}\left(\frac{\alpha\alpha_u + A\alpha_u + 2\alpha^2h_D + \alpha Ah_D + \alpha\alpha_u h_D + \alpha A_uT_D + AA_uT_D + \alpha_u A_uT_D}{(Aa_u + AA_uT_D + a_uA_uT_D)(2aa_u + Aa_u + 4a^2h_D + 2aAh_D + 2aa_uh_D + 2aA_uT_D + AA_uT_D + a_uA_uT_D)} e^{-A_u x_D - A} \right) \qquad \text{(E.12)}$$

Appendix F: Numerical Model Equations

All PHAST flow, transport, and chemical reaction equations are sourced from (Parkhurst et al., 2010). A number of governing assumptions are made for the PHAST simulator including:

- Groundwater fully saturates the porous medium within the region of groundwater flow, referred to as the simulation region.
- Groundwater flow is described by Darcy's law.
- Groundwater and the porous medium are compressible under confined flow conditions.
- Groundwater and the porous medium are incompressible under unconfined flow conditions.
- Groundwater has constant, uniform density and viscosity.
- Isothermal conditions exist in the simulation region with respect to flow and transport.
- Porosity and permeability are functions of space.
- The coordinate system is orthogonal and aligned with the principal directions of the permeability tensor so that this tensor is diagonal for anisotropic media.
- The coordinate system is right-handed; that is, when the curl of the right hand fingers is from positive X-axis to positive Y-axis, the thumb points in the direction of the positive Z-axis.
- Dispersive-mass fluxes of the bulk fluid from spatial-velocity fluctuations are neglected.
- Contributions to the total fluid mass balance from pure-solute mass sources within the region are neglected.

- Multiple solute components are present.
- Chemistry is defined by a set of chemical reactions, both equilibrium and kinetic.
- Changes in the ratio of solid reactants to mass of water caused by porosity changes in confined systems are neglected.
- Chemical reactions do not induce porosity or permeability changes.
- Dispersivity values are the same for each chemical component

Flow and Transport Equations

$$S_s \frac{\partial h}{\partial t} = \nabla \bullet \boldsymbol{K} \nabla h + q, \qquad \text{(F.1)}$$

$$\text{with } h = \frac{p}{\rho g} + z, \qquad \text{(F.2)}$$

Equations (F.1) and (F.2) describe groundwater flow in the PHAST model domain, where $h = \frac{p}{\rho g} + z$ equals the potentiometric head (pressure, $\frac{p}{\rho g}$, and elevation, z) S_s is the storage coefficient (m^{-1}) of the formation, ∇ is the divergence operator for vectors

The general reactive transport equation for both equilibrium and kinetic reactions used in PHAST is sourced from Bear (1972) and is as follows:

$$\frac{\partial}{\partial t}(\varepsilon\rho c_j) = \nabla\bullet\varepsilon \boldsymbol{D}\nabla\rho c_j - \nabla\bullet\varepsilon \boldsymbol{v}\rho c_j - \sum_{e=1}^{N_E} \upsilon_{j,e}^{E}\frac{\partial}{\partial t}(\varepsilon\rho\bar{c}_e) + \sum_{k=1}^{N_K} \upsilon_{j,k}^{K}\varepsilon\rho R_k + q\varepsilon\rho\hat{c}_j \; ; \quad j = 1, \ldots, N_c, \tag{F.3}$$

where c_j is the total aqueous concentration of component j (mol/kgw); $\boldsymbol{D}$ is the dispersion-coefficient tensor (m^2/s); N_E is the number of heterogeneous equilibrium reactions; $\upsilon_{j,e}^{E}$ is the stoichiometric coefficient of component j in heterogeneous equilibrium reaction e (unitless); $\bar{c}_e$ is the concentration of solid reactant e (mol/kgw); N_K is the number of kinetic reactions; $\upsilon_{j,k}^{K}$ is the stoichiometric coefficient of component j in kinetic reaction k (unitless); R_k is the rate of kinetic reaction k (mol kgw^{-1} s^{-1} [moles per kilogram of water per second]); $\hat{c}_j$ is the total aqueous concentration of component j in the source water (mol/kgw); and N_c is the number of chemical components in the system.

Equilibrium Reaction Equations

All equilibrium reactions are based on mass-action equations relating species activities to equilibrium constants in Equation (F.4):

$$K = \frac{\prod_{products} a_p^{\upsilon_p}}{\prod_{reactants} a_r^{\upsilon_r}}, \qquad \text{(F.4)}$$

Where K is the equilibrium constant, a is activity, υ_r and υ_p are stoichiometric coefficient of the reactants and products in the chemical equation.

Appendix G: MATLAB Code

The following MATLAB codes incorporate adaptations of existing code (in the case of the pressure analytical solution), or new code altogether (for the geochemistry numerical model).

Pressure Model

```
clc
clear all
global N au TD etaD xD

%% Sean Porse and Mehdi Zeidouni
%% July 30, 2013

%%Analysis of statistical distribution of Hastings permeability data
fileToRead1 = 'permeability.txt';%% Appendix E Data
newData1 = importdata(fileToRead1);

% Create new variables in the base workspace from those fields.
vars = fieldnames(newData1);
for i = 1:length(vars)
    assignin('base', vars{i}, newData1.(vars{i}));
end
K = newData1.data(:,6);

[p, ci] = betafit(K,0.05); % Fits a Beta function to the raw permeability data
%% User input
```

```
% Order of formations: Frio, Anahuac, M-14, M-13, M-12, M-11, M-10, M-9,
% M-8, M-7, M-6, M-5, M-4, Evangeline Aquifer, Chicot Aquifer
q=0.0453;   %injection rate (m3/s)
aa=500;     %Injection well-fault distance (m)
k=4.65E-13; %Injection zone permeability (m2)
h=40;       %Injection zone thickness (m)
mu=1e-3;    %fluid viscosity (Pa.s)
ct=1e-9;    %compressibility in 1/Pa
eta=k/(0.3*mu*ct);   %Diffusivity coefficient of the injection zone (m2/s)
K_est = betarnd(p(1),p(2), 1000,1); %Generates 1000 random permeability samples from
the estimated (p) beta distribution TO BE USED FOR ABOVE AQUIFERS, UPFAULT PERMS

N=13;
hcaprock=[252
    10*ones(N-1,1)];    %Caprock thicknesses (m)
hu=[45.72;
300.48;62.79;133.81;89.92;40.84;2.74;46.33;56.69;48.77;35.05;182.88;304.80]; %Upper
aquifer thicknesses (m) from M-14 to Chicot
fw=1.68; %fault width (m)
fwd= abs(lhsnorm(fw, 1, 1000)); %create fault width distribution
xm=100; %Distance from the fault to the monitoring well (m)
tm=(86400*365)*[0.1 1 2 5 10 25 50 75 100]; %times at which leakage rate to be
evaluated (s)

%%
iterations = 10; %# of realizations
qlDm=zeros(size(tm,2)*N,iterations); %preallocate leakage rate data set size
PDm=zeros(size(tm,2)*N,iterations); %preallocate pressure change data set size
ku=zeros(N,1); % Upper aquifer permeabilities (m3/s)
tDm=eta*tm/aa^2;
```

```
etau = ones(N,1); %Upper aquifers diffusivities (m2/s)

tic

for jj = 1:iterations;
    wf = fwd(jj)*ones(N,1); %sample one fault width from distribution
    ks = K_est(jj)*ones(N,1); %One Random sampling from Upfault permeability (kf,
m2)
    kf=ks; %set upfault permeability to randomly selected permeability

    for kk = 1:N
        ku(kk) = datasample(K_est, 1);
    end

    for kk = 1:N
        etau(kk,1)=ku(kk)/(0.3*mu*ct);    %Upper aquifers diffusivities (m2/s)
    end

    for ii=1:N
        if ii==1
            L(ii)=(h+hu(ii))/2+hcaprock(ii);
        else
            L(ii)=(hu(ii)+hu(ii-1))/2+hcaprock(ii);
        end
    end

    au=aa*ks.*wf./(2*k*h*L');
    TD=(ku.*hu)./(k.*h);
    etaD=etau/eta;

    qlD=RateSim(tDm);
```

```
    qlDm(:,jj)=reshape(qlD',size(qlD,1)*size(qlD,2),1);

    xD=-xm/aa;
    PD=PSim(tDm);
    PDm(:,jj)=reshape(PD',size(PD,1)*size(PD,2),1);
end

 LeakRate = qlDm.*q; %Leakage rate (m3/s)
 DeltaP = (q*mu.*PDm./(1000*k*h)); %Pressure change values (kPa)
toc

%% Graph Leakage and Pressure Rates


%For cumulative leakage rate (qlDm)

ee = cell(1, iterations); %preallocate cell array for filling from MC iterations
clr = jet(iterations);

for bb = 1:iterations;
    cc = mat2cell(qlDm, [size(qlDm, 1)], [ones(1, iterations)]); %break up qlDm N x
iterations (e.g. 52x10) matrix into each iteration
    dd = reshape(cc{:,bb}, size(tm, 2), N); %take each iteration and reshape them to
a 4x13 matrix and place new array into cell arrays for accessing to graph
    ee{bb} = dd; %store reshaped iterations in a new cell array
    hold on
   figure(1); semilogx(tm/86400/365,ee{:,bb}(:,1), 'color',(clr(bb,:))) %plot
iterations for qlDm in M-14
    xlabel('Time (years)')
    ylabel('q_l (m^3/s)')
    hold off
```

```
end

EE = cell(1, iterations); %preallocate cell array for filling from MC iterations
Xq = (0:1.37:100);
XX = [0.1 1 2 5 10 25 50 75 100];

for AA = 1:iterations;
    BB = mat2cell(DeltaP, [size(DeltaP, 1)], [ones(1, iterations)]); %break up PDm N
x iterations (e.g. 52x10) matrix into each iteration
    CC = reshape(BB{:,AA}, size(tm, 2), N); %take each iteration and reshape them to
a 4x13 matrix and place new array into cell arrays for accessing to graph
    DD{AA} = CC; %store reshaped iterations in a new cell array
    hold on
   figure(2); plot(Xq,(interp1(XX,DD{:,AA}(:,1),Xq,'spline')), 'color',clr(AA,:))
%plot iterations for PDm in M-14
   rline = refline(0, 0.03);
   set(rline,'color', 'r', 'LineStyle',':')
   xlabel('Time (years)')
   ylabel('\DeltaP (kPa)')
   hold off
end

legend('rline', 'Minimum Commercial Detection Limit')
```

Geochemical Model

.

```
%Vary all PHAST permeability values based on Hastings distribution
% 7/14/13, S. Porse and T. Caldwell (BEG)

clear all; close all;

%% Analysis of statistical distribution of Hastings permeability data

fileToRead1 = 'permeability.txt'; % Appendix E Data

newData1 = importdata(fileToRead1);

% Create new variables in the base workspace from those fields.
vars = fieldnames(newData1);
for i = 1:length(vars)
    assignin('base', vars{i}, newData1.(vars{i}));
end
K = newData1.data(:,7);

[p, ci] = betafit(K,0.05); % Fits a Beta function to the raw permeability data

K_est =(betarnd(p(1),p(2), 1000,1)); %Generates 1000 random permeability samples

%%
tic
db_name = 'hastings_transport_AllAZMIK'; %Name of project file

iterations = 100;
```

```
% Preallocate for storing pH and Cl file data
Cl_data = zeros(8030, iterations);
Br_data = zeros(8030, iterations);

for i = 1:iterations
    value_OPTa = num2str(datasample(K_est,1));%M-14 K
    value_OPTb = num2str(datasample(K_est,1));%M-13 K
    value_OPTc = num2str(datasample(K_est,1));%M-12 K
    value_OPTd = num2str(datasample(K_est,1));%M-11 K
    value_OPTe = num2str(datasample(K_est,1));%M-10 K
    value_OPTf = num2str(datasample(K_est,1));%M-9 K
    value_OPTg = num2str(datasample(K_est,1));%M-8 K
    value_OPTh = num2str(datasample(K_est,1));%M-7 K
    value_OPTi = num2str(datasample(K_est,1));%M-6 K
    value_OPTj = num2str(datasample(K_est,1));%M-5 K
    value_OPTk = num2str(datasample(K_est,1));%M-4 K

    fid_orig = fopen('Opt1_hastings_transport_AllAZMIK.trans.dat', 'r');
    fid_new = fopen('hastings_transport_AllAZMIK.trans.dat', 'wt');

    while 1
        str = (fgetl(fid_orig));
        if ~ischar(str), break, end
        s1  = strrep(str,'oP_a', value_OPTa);
        s2  = strrep(s1, 'oP_b', value_OPTb);
        s3  = strrep(s2, 'oP_c', value_OPTc);
        s4  = strrep(s3, 'oP_d', value_OPTd);
        s5  = strrep(s4, 'oP_e', value_OPTe);
        s6  = strrep(s5, 'oP_f', value_OPTf);
        s7  = strrep(s6, 'oP_g', value_OPTg);
```

```
        s8  = strrep(s7, 'oP_h', value_OPTh);
        s9  = strrep(s8, 'oP_i', value_OPTi);
        s10  = strrep(s9,'oP_j', value_OPTj);
        s11  = strrep(s10,'oP_k', value_OPTk);
        fprintf(fid_new, '%s\n',s11);
    end
    % Close original and new model input files
    fclose(fid_orig);
    fclose(fid_new);

    system(['PHASTINPUT.EXE ' ,db_name]); %Generate phast.tmp intermediate file
    !phast-ser.exe % call the executable and run phast.tmp file

    file1 = 'hastings_transport_AllAZMIK.wel.xyz.tsv';
    newdata1 = importdata(file1);
    vars = fieldnames(newdata1);
    for jj = 1:length(vars)
        assignin('base', vars{jj}, newdata1.(vars{jj}));
    end
        Cl_data(:,i) = newdata1.data(:,11)'; %Chloride concentration
        Br_data(:,i) = newdata1.data(:,8)'; %Bromide as a tracer

    save data_AllAZMIK Cl_data Br_data;
end
run_time = toc;

%% Convert and break up Br_data

%Need to convert molality to molarity
%Convert molar concentrations to grams per liter
```

```
Br_grams=zeros(length(Br_data), iterations);
Br_grams=79.904*(Br_data);

%Convert to milligrams per liter
Br_milligrams=zeros(length(Br_grams), iterations);
Br_milligrams=1000*(Br_grams);

% Convert grams per kilogram concentrations to volumetric concentrations
% (grams of Bromide + 1000 grams of water)

Br_volume=zeros(length(Br_data), iterations);
Br_volume=1000+(Br_grams);

% Calculate total volume of solution (Liters)

Br_totalsolution = zeros(length(Br_data), iterations);
Br_totalsolution = (Br_volume)*(1/1100); %1.1 gram/1 milliliter density

%Calculate the molarity of each time step for Bromide (grams/Liter), then
%grams/Liter molarity value to milligrams(mg/L)

Br_final = zeros(length(Br_data), iterations);
Br_final = (1000/1100)*(Br_data);

%% Convert and break up Cl_data

%Need to convert molality to molarity
%Convert molar concentrations to grams per kilogram

Cl_grams=zeros(length(Cl_data), iterations);
Cl_grams=35.453*(Cl_data);
```

```
%Convert to milligrams per liter
Cl_milligrams=zeros(length(Cl_grams), iterations);
Cl_milligrams=1000*(Cl_grams);

% Convert grams per kilogram concentrations to volumetric concentrations
% (grams of Bromide + 1000 grams of water)

Cl_volume=zeros(length(Cl_data), iterations);
Cl_volume=1000+(Cl_grams);

% Calculate total volume of solution (Liters)

Cl_totalsolution = zeros(length(Cl_data), iterations);
Cl_totalsolution = (Cl_volume)*(1/1100); %1.1 gram/1 milliliter density

%Calculate the molarity of each time step for Bromide (grams/Liter), then
%grams/Liter molarity value to milligrams(mg/L)

Cl_final = zeros(length(Cl_data), iterations);
Cl_final = (1000/1100)*(Cl_data);
```

Bibliography

Alcala, Francisco J., and Emilio Custodio. 2008. "Using the Cl/Br ratio as a tracer to identify the origin of salinity in aquifers in Spain and Portugal." *Journal of Hydrology* no. 359 (1-2):189-207. doi: 10.1016/j.jhydrol.2008.06.028.

Alvarado, V., and E. Manrique. 2010. "Enhanced Oil Recovery: An Update Review." *Energies* no. 3 (9):1529-1575. doi: 10.3390/en3091529.

Ambrose, W. A., S. Lakshminarasimhan, M. H. Holtz, V. Nunez-Lopez, S. D. Hovorka, and I. Duncan. 2008. "Geologic factors controlling CO_2 storage capacity and permanence: case studies based on experience with heterogeneity in oil and gas reservoirs applied to CO_2 storage." *Environmental Geology* no. 54 (8):1619-1633. doi: 10.1007/s00254-007-0940-2.

Apps, J., L. Zheng, Y. Zhang, T. Xu, and J.T. Birkholzer. 2009. "Evaluation of Groundwater Chemistry Changes in Response to CO_2 Leakage from Deep Geological Storage." *Transport In Porous Media* no. 82 (1):215-246.

Avant, C., S. Daungcauw, B. Behera, S. Danpanich, W. Laprabang, I. De Santo, G. Heath, K. Osman, Z. Kahn, J. Russell, P. Sims, M. Slapal, and C. Trevis. 2012. "Testing the Limits in Extreme Well Conditions." *Oilfield Review* no. 24 (3):19.

Bachu, S. 2003. "Screening and ranking of sedimentary basins for sequestration of CO_2 in geological media in response to climate change." *Environmental Geology* no. 44 (3):277-289. doi: 10.1007/s00254-003-0762-9.

Baker Jr, E.T. 1979. Stratigraphic and Hydrogeologic Framework of Part of the Coastal Plain of Texas. Texas Department of Water Resources. Austin, TX.

Banga, T., and D. Van Nieuwenhuise. 2003. Evidence of Reservoir Compartmentalization from a Coupled Study on Brine Chemistry and Stratigraphy in and Around the South Liberty Salt Dome, Texas. In *American Association of Petroleum Geologists Annual Convention*. Salt Lake City, Utah: American Association of Petroleum Geologists.

Birkholzer, J. T., Q. L. Zhou, and C. F. Tsang. 2009. "Large-scale impact of CO_2 storage in deep saline aquifers: A sensitivity study on pressure response in stratified systems." *International Journal of Greenhouse Gas Control*no. 3 (2):181-194. doi: 10.1016/j.ijggc.2008.08.002.

Birkholzer, Jens T., and Quanlin Zhou. 2009. "Basin-scale hydrogeologic impacts of CO_2 storage: Capacity and regulatory implications." *International Journal of Greenhouse Gas Control* no. 3 (6):745-756. doi: 10.1016/j.ijggc.2009.07.002.

Burr, D. T., E. A. Sudicky, and R. L. Naff. 1994. "Nonreactive and Reactive Solution Transport in 3-Dimensional Heterogeneous Porous-Media – Mean Displacement, Plume Spreading, and Uncertainty." *Water Resources Research* no. 30 (3):791-815. doi: 10.1029/93wr02946.

Cihan, A., Q. L. Zhou, and J. T. Birkholzer. 2011. "Analytical solutions for pressure perturbation and fluid leakage through aquitards and wells in multilayered-aquifer systems." *Water Resources Research* no. 47. doi: W10504 10.1029/2011wr010721.

Cihan, Abdullah, Jens T. Birkholzer, and Quanlin Zhou. 2013. "Pressure Buildup and Brine Migration During CO_2 Storage in Multilayered Aquifers." *Ground Water* no. 51 (2):252-267. doi: 10.1111/j.1745-6584.2012.00972.x.

Class, Holger, Anozie Ebigbo, Rainer Helmig, Helge K. Dahle, Jan M. Nordbotten, Michael A. Celia, Pascal Audigane, Melanie Darcis, Jonathan Ennis-King, Yaqing Fan, Bernd Flemisch, Sarah E. Gasda, Min Jin, Stefanie Krug, Diane Labregere, Ali Naderi Beni, Rajesh J. Pawar, Adil Sbai, Sunil G. Thomas, Laurent Trenty, and Lingli Wei. 2009. "A benchmark study on problems related to CO_2 storage in geologic formations." *Computational Geosciences* no. 13 (4):409-434. doi: 10.1007/s10596-009-9146-x.

Crameik, T.D., and J.A. Plassey. 1972. Carbon Dioxide Injection Project Sacroc Unit, Scurry County, Texas. In *Divison of Production*. Annual Meeting Papers American Petroleum Institute.

Daley, Thomas M., Jonathan B. Ajo-Franklin, and Christine Doughty. 2011. "Constraining the reservoir model of an injected CO_2 plume with crosswell CASSM at the Frio-II brine pilot." *International Journal of Greenhouse Gas Control* no. 5 (4):1022-1030. doi: 10.1016/j.ijggc.2011.03.002.

Davis, G. B., C. Barber, T. R. Power, J. Thierrin, B. M. Patterson, J. L. Rayner, and Q. L. Wu. 1999. "The variability and intrinsic remediation of a BTEX plume in anaerobic sulphate-rich groundwater." *Journal of Contaminant Hydrology* no. 36 (3-4):265-290. doi: 10.1016/s0169-7722(98)00148-x.

Davis, S. N., D. O. Whittemore, and J. Fabryka-Martin. 1998. "Uses of chloride/bromide ratios in studies of potable water." *Ground Water* no. 36 (2):338-350. doi: 10.1111/j.1745-6584.1998.tb01099.x.

de Boor, C. 1978. *A Practical Guide to Splines*. Vol. 27. Germany: Springer-Verlag.

Doughty, C., and K. Pruess. 2004. "Modeling supercritical carbon dioxide injection in heterogeneous porous media." *Vadose Zone Journal* no. 3 (3):837-847.

Ebigbo, A., H. Class, and R. Helmig. 2007. " CO_2 leakage through an abandoned well: problem-oriented benchmarks." *Computational Geosciences* no. 11 (2):103-115. doi: 10.1007/s10596-006-9033-7.

Emberley, S., I. Hutcheon, M. Shevalier, K. Durocher, B. Mayer, W. D. Gunter, and E. H. Perkins. 2005. "Monitoring of fluid-rock interaction and CO_2 storage through produced fluid sampling at the Weyburn CO_2-injection enhanced oil recovery site, Saskatchewan, Canada." *Applied Geochemistry* no. 20 (6):1131-1157. doi: 10.1016/j.apgeochem.2005.02.007.

Energy, U.S. Department of. 2013. *FE Implementation of the Recovery Act* 2013 [cited 10/25/13 2013]. Available from http://energy.gov/fe/fe-implementation-recovery-act.

Freeze, R. A., B. James, J. Massmann, T. Sperling, and L. Smith. 1992. "Hydrogeological Decision-Analysis .4. The Concept of Data Worth and Its Use in the Development of Site Investigation Strategies." *Ground Water* no. 30 (4):574-588. doi: 10.1111/j.1745-6584.1992.tb01534.x.

Gaus, I. 2010. "Role and impact of CO_2-rock interactions during CO_2 storage in sedimentary rocks." *International Journal of Greenhouse Gas Control* no. 4 (1):73-89. doi: 10.1016/j.ijggc.2009.09.015.

Gaus, I., P. Audigane, L. Andre, J. Lions, N. Jacquemet, P. Dutst, I. Czernichowski-Lauriol, and M. Azaroual. 2008. "Geochemical and solute transport modelling for CO_2 storage, what to expect from it?" *International Journal of Greenhouse Gas Control* no. 2 (4):605-625. doi: 10.1016/j.ijggc.2008.02.011.

Gee, G.W., and D. Or. 2002. "Particle-Size Analysis." In *Methods of Soil Analysis Part 4 Physical Methods*, edited by J. Dane and C. Topp, 255-295. Madison, Wisconsin: Soil Science Society of America.

Halbouty, M. 1968. "Economic and Geologic Aspects of Search for Gas in Texas Gulf Coasts." In, 271-283. American Association of Petroleum Geologists Special Volume.

Hermanrud, C., O. Eiken, O.R. Hansen, H. Nordgaard Bolaas, T. Simmenes, G. Teige, H. Hansen, and S. Johansen. 2013. Importance of Pressure Management in CO_2

Storage. In *Offshore Technology Conference*. Houston, TX, USA: Offshore Technology Conference.

Hillier, S. 1999. "Use of an air brush to spray dry samples for X-ray powder diffraction." *Clay Minerals* no. 34 (1):127-135. doi: 10.1180/000985599545984.

Horvitz, L. 1985. "Geochemical-Exploration for Petroleum." *Science* no. 229 (4716):821-827. doi: 10.1126/science.229.4716.821.

Hou, Z. S., M. L. Rockhold, and C. J. Murray. 2012. "Evaluating the impact of caprock and reservoir properties on potential risk of CO_2 leakage after injection." *Environmental Earth Sciences* no. 66 (8):2403-2415. doi: 10.1007/s12665-011-1465-2.

Hovorka, Susan D., Timothy A. Meckel, Ramon H. Trevino, Jiemin Lu, Jean-Philippe Nicot, Jong-Won Choi, David Freeman, Paul Cook, Thomas M. Daley, Jonathan B. Ajo-Franklin, Barry M. Freifeild, Christine Doughty, Charles R. Carrigan, Doug La Brecque, Yousif K. Kharaka, James J. Thordsen, Tommy J. Phelps, Changbing Yang, Katherine D. Romanak, Tongwei Zhang, Robert M. Holt, Jeffery S. Lindler, and Robert J. Butsch. 2011. "Monitoring a large volume CO_2 injection: Year two results from SECARB project at Denbury's Cranfield, Mississippi, USA." *10th International Conference on Greenhouse Gas Control Technologies* no. 4:3478-3485. doi: 10.1016/j.egypro.2011.02.274.

Humez, Pauline, Pascal Audigane, Julie Lions, Christophe Chiaberge, and Gael Bellenfant. 2011. "Modeling of CO_2 Leakage up Through an Abandoned Well from Deep Saline Aquifer to Shallow Fresh Groundwaters." *Transport in Porous Media* no. 90 (1):153-181. doi: 10.1007/s11242-011-9801-2.

Hyeong, K., and R. M. Capuano. 2001. "Ca/Mg of brines in Miocene/Oligocene clastic sediments of the Texas Gulf Coast: Buffering by calcite/disordered dolomite equilibria." *Geochimica Et Cosmochimica Acta* no. 65 (18):3065-3080. doi: 10.1016/s0016-7037(01)00659-7.

IPCC. 2005. "Carbon dioxide capture and storage: Intergovernmental Panel on Climate Change Special Report." In, edited by L.A. Meyer. New York: Cambridge Univ. Press.

Kao, C. M., and Y. S. Wang. 2001. "Field investigation of the natural attenuation and intrinsic biodegradation rates at an underground storage tank site." *Environmental Geology* no. 40 (4-5):622-631.

Kell, S. 2011. State Oil and Gas Agency Groundwater Investigations and their Role in Advancing Regulatory Reforms, A Two-State Review: Ohio and Texas. Oklahoma City: Ground Water Protection Council.

Kesler, S. E., M. S. Appold, A. M. Martini, L. M. Walter, T. J. Huston, and J. R. Kyle. 1995. "Na-Cl-Br Systematics of Mineralizing Brines in Mississippi Valley-Type Deposits." *Geology* no. 23 (7):641-644. doi: 10.1130/0091-7613(1995)023<0641:ncbsom>2.3.co;2.

Kharaka, Y. K., D. R. Cole, S. D. Hovorka, W. D. Gunter, K. G. Knauss, and B. M. Freifeld. 2006. "Gas-water-rock interactions in Frio Formation following CO_2 injection: Implications for the storage of greenhouse gases in sedimentary basins." *Geology* no. 34 (7):577-580. doi: 10.1130/g22357.1.

Kipp, K.L. 1997. Guide to the revised heat and solute transport simulator HST3D - Version 2. In *Water-Resources Investigations Report*. Denver, CO: United States Geological Survey.

Konert, M., and J. Vandenberghe. 1997. "Comparison of laser grain size analysis with pipette and sieve analysis: A solution for the underestimation of the clay fraction." *Sedimentology* no. 44 (3):523-535. doi: 10.1046/j.1365-3091.1997.d01-38.x.

Kongsjorden, H., O. Karstad, and T. A. Torp. 1997. "Saline aquifer storage of carbon dioxide in the Sleipner project." *Waste Management* no. 17 (5-6):303-308.

Laboratory, National Energy Technology. 2010. Carbon Dioxide Enhanced Oil Recovery: Untapped Domestic Energy Supply and Long Term Carbon Solution. U.S. Department of Energy.

Laboratory, National Energy Technology. 2012a. Leucadia Energy, LLC: Lake Charles Carbon Capture & Sequestration Project

Laboratory, National Energy Technology. 2012b. *The 2012 United States Carbon Utilization and Storage Atlas*. 4 ed. United States: The U.S. Department of Energy.

Laboratory, National Energy Technology. 2013. Cost and Performance Baseline for Fossil Energy Plants Volume 1: Bituminous Coal and Natural Gas to Electricity. National Energy Technology Laboratory.

Land, L. S. 1995. "Na-Ca-Cl Saline Formation Waters, Frio Formation (Oligocene), South Texas, USA – Products of Diagenesis." *Geochimica Et Cosmochimica Acta* no. 59 (11):2163-2174. doi: 10.1016/0016-7037(95)00098-k.

Law, D.H.-S., and S. Bachu. 1996. "Hydrogeological and numerical analysis of CO_2 disposal in deep aquifers in the Alberta sedimentary basin." *Energy Conversion Management* no. 37:1167-1174.

Leblanc, D. R., S. P. Garabedian, K. M. Hess, L. W. Gelhar, R. D. Quadri, K. G. Stollenwerk, and W. W. Wood. 1991. "Large-Scale Natural Gradient Tracer Test in Sand and Gravel, Cape-Cod, Massachusetts .1. Experimental-Design and Observed Tracer Movement." *Water Resources Research* no. 27 (5):895-910. doi: 10.1029/91wr00241.

LeNeveu, D.M. 2008. "CQUESTRA: A risk and performance assessment code for geological sequestration of carbon dioxide." *Energy Conversion Management* no. 49:32-46.

Lewicki, J.L., J.T. Birkholzer, and C-F Tsang. 2007. "Natural and industrial analogues for leakage of CO_2 from storage reservoirs: identification of features, events, and processes and lessons learned." *Environmental Geology* no. 52 (3):457-467.

Masch, F. D., and K. J. Denny. 1966. "Grain Size Distribution and its Effect on Permeability of Unconsolidated Sands." *Water Resources Research* no. 2 (4):665-&. doi: 10.1029/WR002i004p00665.

Massmann, J., R. A. Freeze, L. Smith, T. Sperling, and B. James. 1991. "Hydrogeological Decision-Analysis .2. Applicatoins to Groundwater Contamination." *Ground Water* no. 29 (4):536-548. doi: 10.1111/j.1745-6584.1991.tb00545.x.

Massmann, Joel, and R. Allan Freeze. 1987. "Groundwater contamination from waste management sites: The interaction between risk-based engineering design and regulatory policy: 1. Methodology." *Water Resources Research* no. 23 (2):351-367. doi: 10.1029/WR023i002p00351.

Maynard, J. R. 2006. "Fluvial response to active extension: evidence from 3D seismic data from the Frio Formation (Oligo-Miocene) of the Texas Gulf of Mexico Coast, USA." *Sedimentology* no. 53 (3):515-536. doi: 10.1111/j.1365-3091.2006.00782.x.

McKay, M. D., R. J. Beckman, and W. J. Conover. 1979. "A Comparison of Three Methods for Selecting Values of Input Variables in the Analysis of Output From a Computer code." *Technometrics* no. 21 (2):239-245. doi: 10.2307/1268522.

McWilliams, J. 1972. Large Salt Water Disposal Systems at East Texas and Hastings Oil Fields, Texas. Underground Waste Management and Environmental Implications: American Association of Petroleum Geologists.

Meckel, T.A., and S.D. Hovorka. 2010. Above-Zone Pressure Monitoring as a Surveillance Tool for Carbon Sequestration Projects. In *SPE International Conference on CO_2 Capture, Storage, and Utilization, 10-12 November*. New Orleans, LA, USA: Society of Petroleum Engineers.

Morton, R.A., and S.L. Lynton. 1987. "Regional Variation in Formation Water Chemistry, Frio Formation (Oligocene), Texas Gulf Coast." *American Association of Petroleum Geologists Bulletin* no. 71:191-206.

Mulligan, C. N., R. N. Yong, and B. F. Gibbs. 2001. "Remediation technologies for metal-contaminated soils and groundwater: an evaluation." *Engineering Geology* no. 60 (1-4):193-207. doi: 10.1016/s0013-7952(00)00101-0.

Naff, R. L., D. F. Haley, and E. A. Sudicky. 1998. "High-resolution Monte Carlo simulation of flow and conservative transport in heterogeneous porous media 1. Methodology and flow results." *Water Resources Research* no. 34 (4):663-677. doi: 10.1029/97wr02712.

Nicot, Jean-Philippe. 2009. "A survey of oil and gas wells in the Texas Gulf Coast, USA, and implications for geological sequestration of CO_2." *Environmental Geology* no. 57 (7):1625-1638. doi: 10.1007/s00254-008-1444-4.

Nicot, Jean-Philippe, Susan D. Hovorka, and Jong-Won Choi. 2009. "Investigation of water displacement following large CO_2 sequestration operations." *Greenhouse Gas Control Technologies 9* no. 1 (1):4411-4418. doi: 10.1016/j.egypro.2009.02.256.

Nicot, Jean-Philippe, Curtis M. Oldenburg, Steven L. Bryant, and Susan D. Hovorka. 2009. "Pressure perturbations from geologic carbon sequestration: Area-of-review boundaries and borehole leakage driving forces." *Greenhouse Gas Control Technologies 9* no. 1 (1):47-54. doi: 10.1016/j.egypro.2009.01.009.

Nimz, G.J., and G.B. Hudson. 2005. "The use of noble gas isotopes for monitoring leakage of geologically stored CO_2." In *Carbon dioxide capture for storage in*

deep geologic formations, edited by D. Thomas and S. Benson, 1113-1130. Amsterdam: Elsevier.

Nordbotten, J. M., M. A. Celia, and S. Bachu. 2004. "Analytical solutions for leakage rates through abandoned wells." *Water Resources Research* no. 40 (4). doi: 10.1029/2003wr002997.

Nordbotten, J. M., M. A. Celia, and S. Bachu. 2005. "Injection and storage of CO_2 in deep saline aquifers: Analytical solution for CO_2 plume evolution during injection." *Transport in Porous Media* no. 58 (3):339-360. doi: 10.1007/s11242-004-0670-9.

Oldenburg, Curtis M., and Antonio Pio Rinaldi. 2011. "Buoyancy Effects on Upward Brine Displacement Caused by CO_2 Injection." *Transport in Porous Media* no. 87 (2):525-540. doi: 10.1007/s11242-010-9699-0.

Omega. 1998. *Force-Related Measurements*. 3 vols. Vol. 3, *Transactions in Measurement and Control*: Putnam Publishing,Omega Press LLc.

Parkhurst, D. L., K. L. Kipp, P. Engesgaard, and S. R. Charlton. 2005. "PHAST - A program for simulating ground-water flow, solute transport, and multicomponent geochemical reactions." *Geochimica Et Cosmochimica Acta* no. 69 (10):A156-A156.

Perry, K. 2005. "Natural Gas Storage Industry Experience and Technology: Potential Application to CO_2 Geological Storage." In *Carbon Dioxide Capture for Storage in Deep Geologic Formations - Results from the CO_2 Capture Project: Geologic Storage of Carbon Dioxide with Monitoring and Verification*, edited by S.M. Benson, C. Oldenburg, Hoversten M. and S. Imbus, 815-825. The Netherlands: Elsevier B.V.

Phade, A., and Y. Gupta. 2008. Reservoir Pressure Management Using Waterflooding: A Case Study. In *SPE Western Regional and Pacific Section AAPG Joint Meeting*. Bakersfield, CA, USA: Society of Petroleum Engineers.

Rainwater, E.H. 1970. Geologic Occurrence of Oil and Gas in Miocene of Gulf Coast of United States. American Association of Petroleum Geologists Bulletin.

Rittenhouse, G. 1967. "Bromine in Oil-Field Waters and Its Use in Determining Possibilities of Origin of These Waters." *AAPG Bulletin* no. 51 (12):2430-2440.

Schlumberger. 2006a. Fundamentals of Formation Testing. Texas: Schlumberger Marketing Communications.

Schlumberger. 2006b. Signature Quartz Gauges: reliable, accurate pressure measurements in extreme environments.

Schnaar, G., and D. C. Digiulio. 2009. "Computational Modeling of the Geologic Sequestration of Carbon Dioxide." *Vadose Zone Journal* no. 8 (2):389-403. doi: 10.2136/vzj2008.0112.

Siirila, E. R., A. K. Navarre-Sitchler, R. M. Maxwell, and J. E. McCray. 2012. "A quantitative methodology to assess the risks to human health from CO_2 leakage into groundwater." *Advances in Water Resources* no. 36:146-164. doi: 10.1016/j.advwatres.2010.11.005.

Smyth, R.C., S.D. Hovorka, J. Lu, Romanak K.D., J.W. Partin, and C. Wong. 2008. Assessing risk to fresh water resources from long term CO_2 injection-laboratory and field studies: presented at the 9th International Conference on Greenhouse Gas Control Technologies (GHGT-9), Washington, D.C.: GCCC.

Stalker, L., C. Boreham, and E. Perkins. 2009. "A Review of Tracers in Monitoring CO_2 Breakthrough: Properties, Uses, Case Studies, and Novel Tracers." In *AAPG Studies in Geology: Carbon dioxide sequestration in geological media—State of the science*, edited by M. Grobe, J.C. Pashin and R.L. Dodge, 595-608.

Sun, Alexander Y., and Jean-Philippe Nicot. 2012. "Inversion of pressure anomaly data for detecting leakage at geologic carbon sequestration sites." *Advances in Water Resources* no. 44:20-29. doi: 10.1016/j.advwatres.2012.04.006.

Sun, Alexander Y., Mehdi Zeidouni, Jean-Philippe Nicot, Zhiming Lu, and Dongxiao Zhang. 2013. "Assessing leakage detectability at geologic CO_2 sequestration sites using the probabilistic collocation method." *Advances in Water Resources* no. 56:49-60. doi: 10.1016/j.advwatres.2012.11.017.

Survey, United States Geological. 2006. "Collection of Water Samples." In *National Field Manual for the Collection of Water-Quality Data*, 1-159.

Taguchi, G. 1986. *Introduction to Quality Engineering: Designing Quality Into Products and Processes*. White Plains, NY: Kraus International Publications.

Technology, Massachusetts Institute of. 2013. *Carbon Dioxide Capture and Storage Projects*. MIT Energy Initiative, 8/15/13 2013 [cited 11/3 2013]. Available from http://sequestration.mit.edu/tools/projects/map_projects.html.

Thomas, W.A. 1953. Hastings Field, Brazoria and Galveston Counties, Texas. Houston Geological Society: American Association of Petroleum Geologists.

USEPA. 2009. Statistical Analysis of Groundwater Monitoring Data at RCRA Facilities: Unified Guidance. edited by Office of Resource Conservation and Recovery: USEPA.

USEPA. 2010. Federal Requirements Under the Underground Injection Control (UIC) Program for Carbon Dioxide (CO_2) Geologic Sequestration (GS) Wells. Washington DC: Federal Register.

Vengosh, A., and E. Rosenthal. 1994. "Saline Groundwater in Israel – Its Bearing on the Water Crisis in the Country." *Journal of Hydrology* no. 156 (1-4):389-430. doi: 10.1016/0022-1694(94)90087-6.

Walter, Lena, Philip John Binning, Sergey Oladyshkin, Bernd Flemisch, and Holger Class. 2012. "Brine migration resulting from CO_2 injection into saline aquifers - An approach to risk estimation including various levels of uncertainty." *International Journal of Greenhouse Gas Control* no. 9:495-506. doi: 10.1016/j.ijggc.2012.05.004.

Watson, T. L., and S. Bachu. 2009. "Evaluation of the Potential for Gas and CO_2 Leakage Along Wellbores." *SPE Drilling & Completion* no. 24 (1):115-126.

Weaver, T. R., S. K. Frape, and J. A. Cherry. 1995. "Recent Cross-Formational Fluid-Flow and Mixing in the Shallow Michigan Basin." *Geological Society of America Bulletin* no. 107 (6):697-707. doi: 10.1130/0016-7606(1995)107<0697:rcfffa>2.3.co;2.

Whittemore, D.O. 1995. "Geochemical differentiation of oil and gas brine from other saltwater sources contaminating water resources; case studies from Kansas and Oklahoma." *Environmental Geosciences* no. 2:15-31.

Wilkin, R. T., and D. C. Digiulio. 2010. "Geochemical Impacts to Groundwater from Geologic Carbon Sequestration: Controls on pH and Inorganic Carbon Concentrations from Reaction Path and Kinetic Modeling." *Environmental Science & Technology* no. 44 (12):4821-4827. doi: 10.1021/es100559j.

Wolaver, B.D., S.D. Hovorka, and R.C. Smyth. 2013. "Greensites and brownsites: Implications for CO_2 sequestration characterization, risk assessment, and monitoring." *International Journal of Greenhouse Gas Control* no. 19 (November):49-62.

Xu, T. F., E. Sonnenthal, N. Spycher, and K. Pruess. 2006. "TOUGHREACT - A simulation program for non-isothermal multiphase reactive geochemical transport in variably saturated geologic media: Applications to geothermal

injectivity and CO_2 geological sequestration." *Computers & Geosciences* no. 32 (2):145-165. doi: 10.1016/j.cageo.2005.06.014.

Yang, C., P. Mickler, R. Reedy, B. Scanlon, K. Romanak, J.P. Nicot, S.D. Hovorka, R.H. Trevino, and T. Larson. 2013. "Single-well push–pull test for assessing potential impacts of CO_2 leakage on groundwater quality in a shallow Gulf Coast aquifer in Cranfield, Mississippi." *International Journal of Greenhouse Gas Control*:13.

Yang, C., K. Romanak, S. Hovorka, R.M. Holt, J. Lindner, and R. Trevino. 2013. "Near-Surface Monitoring of Large-Volume CO_2 Injection at Cranfield: Early Field Test of SECARB Phase III." *SPE Journal* no. 18 (3):486-494.

Young, M. H., P. J. Wierenga, A. W. Warrick, L. L. Hofmann, and S. A. Musil. 1999. "Variability of wetting front velocities during a field-scale infiltration experiment." *Water Resources Research* no. 35 (10):3079-3087. doi: 10.1029/1999wr900191.

Zeidouni, M. 2012. "Analytical model of leakage through fault to overlying formations." *Water Resources Research* no. 48. doi: 10.1029/2012wr012582.

Zheng, L., J. Apps, Y. Zhang, T. Xu, and J.T. Birkholzer. 2009. "Reactive transport simulations to study groundwater quality changes in response to CO_2 leakage from deep geological storage." *Energy Procedia* no. 1 (1):1887-1894.

Zhou, Q., and J.T. Birkholzer. 2011. "On the Scale and Magnitude of Pressure Buildup Induced by Large-Scale Geologic Storage of CO_2." *Greenhouse Gases: Science and Technology* no. 1 (1):11-20.